# $CO_2$ APPLICATIONS IN UNCONVENTIONAL RESERVOIRS: COALBED METHANE, NATURAL DEPLETION AND $CO_2$ SEQUESTRATION

A Dissertation

By

AHMED MOHAMED FARID IBRAHIM

Submitted to the Office of Graduate and Professional Studies of
Texas A&M University
in partial fulfillment of the requirements for the degree of

DOCTOR OF PHILOSOPHY

| | |
|---|---|
| Chair of Committee, | Hisham A. Nasr-El-Din |
| Committee Members, | Berna Hascakir |
| | Hadi Nasrabadi |
| | Mahmoud El-Halwagi |
| Head of Department, | A. Daniel Hill |

December 2017

Major Subject: Petroleum Engineering

# ABSTRACT

Unconventional reservoirs are getting an increase in attention in the oil and gas industry. This is because of the high energy demands from all over the world, which cannot be satisfied by conventional resources alone. Coalbed methane (CBM) currently accounts for approximately 5% of U.S. annual gas production. The performance prediction of CBM is very complex. It is highly affected by the complexity of porosity-permeability variation, reduction due to formation compaction, enhancement due to matrix shrinkage, and the two-phase flow effects. An additional complexity is added if the initial gas content, permeability, and porosity are not available. Also, $CO_2$ sequestration in coal seams is an attractive carbon sequestration technology where the injection of $CO_2$ enhances methane production from coalbeds (ECBM) in addition to storing $CO_2$.

The main objectives of this work are to: (1) develop an integrated model to simulate the b behavior of CBM; A developed generalized material balance equation will be used to account for the solubility of the methane in water, and the changes of porosity and permeability with pressure depletion; (2) Extend the model to simulate the performance of ECBM; (3) evaluate the role of brine salinity, formation pressure and gas composition on the $CO_2$-water-coal wettability; and (4) examine the effect of the water salinity, gas composition, formation pressure, and injection flow rate on the performance of $CO_2$ sequestration in coal cores.

In order to achieve the proposed objectives, a generalized material balance equation is developed to account for the solubility of the methane in water and the changes of porosity and permeability with pressure depletion. An optimization algorithm was also used with the integrated model. The model could be used as a history-matching tool to estimate the original gas-in-place (the adsorbed gas-in-place and the free gas-in-place), the initial formation permeability, the gas and water relative permeability exponents, and the matrix shrinkage coefficient that reflected the permeability changes.

The model was then extended to simulate the performance of ECBM. A compositional material balance (CMB) was used to track the propagation of $CO_2$ concentration in the reservoir. CMB was combined with the stream tube concept to convert

a 2D to a 1D problem. An optimization algorithm was also used with the integrated model. The integrated model could be used as a history-matching tool to estimate the initial formation permeability, the initial formation porosity, the matrix shrinkage, and swelling coefficients that reflected the permeability changes.

In addition, coal blocks were collected from the Bull Hill mine in Oklahoma to be used in the experimental work. The coal sample was characterized using SEM/EDS and proximate thermogravimetric analysis. It was found that the coal sample contains a high carbon content of 82 wt%. Based on these measurements, this coal sample was classified as high volatile bitumen coal. The effects of the injected gas composition and the formation water salinity on the wettability behavior of high volatile bitumen coal will be investigated. The captive bubble method will be used to measure the contact angle in coal–water–$CO_2$ systems at pressures up to 2,000 psi. The contact angle (CA) will be measured at different NaCl concentrations (0-20 g/l). Flue gasses with different nitrogen concentrations will be used to examine the effect of gas composition on wettability behavior. $CO_2$ adsorption isotherm on the coal surface will be examined at different water salinities. Zeta potential measurements will be conducted to understand the effect of salt concentration on coal hydrophobicity. Coreflood tests will be conducted on different coal cores. The change in the effective water-coal permeability after a $CO_2$ injection will be examined. Also, the displacement efficiency of water by $CO_2$ will be estimated. The experimental data will be cross-matched with a numerical simulation to estimate the relative permeability curves.

# DEDICATION

To my family, my wife Walaa, and my daughters Darein and Mariam, for their persistent love and spiritual support in my life.

# ACKNOWLEDGEMENTS

I would like to take this opportunity to express my deepest gratitude and appreciation to my advisor and committee chair, Dr. Hisham A. Nasr-El-Din, for his continuous encouragement and especially for his academic guidance.

Appreciation is extended to the members of my committee, Dr. Hadi Nasrabadi, Dr. Berna Hascakir, and Dr. Mahmoud El-Halwagi, for their help.

Thanks also go to my friends and colleagues and the department faculty and staff for making my time at Texas A&M University a great experience. Ms. K. Gia is acknowledged for proofreading this dissertation.

Finally, I would like to acknowledge the financial support of the Texas A&M U., the Texas Engineering Experiment Station of Texas A&M University and Crisman Institute for Petroleum Research. The facilities and resources provided by the Harold Vance Department of Petroleum Engineering of Texas A&M University are gratefully acknowledged.

# CONTRIBUTORS AND FUNDING SOURCES


## Contributors

This work was supervised by a dissertation committee consisting of Professor Hisham A. Nasr-El-Din, Assistant Professor. Hadi Nasrabadi, and Assistant Professor. Berna Hascakir of the Department of Petroleum Engineering and Professor Mahmoud M. El-Halwagi of the Department of Chemical Engineering.

All other work conducted for the dissertation was completed by the student, under the advisement of Professor Hisham A. Nasr-El-Din of the Department of Petroleum Engineering.

## Funding Sources

This work was financial supported by the Crisman Research Institute, Petroleum Research, Texas A&M University.

# NOMENCLATURE

| | |
|---|---|
| $B_g$ | gas formation volume factor, bbl/scf |
| $B_t$ | total formation volume factor, bbl/STB |
| $B_w$ | water formation volume factor, bbl/STB |
| $c_f$ | formation compressibility, $psi^{-1}$ |
| $c_{sh}$ | formation shrinkage coefficient, dimensionless |
| $c_{sw}$ | formation swelling coefficient, dimensionless |
| $c_w$ | water compressibility, $psi^{-1}$ |
| $E_a$ | adsorbed gas expansion term for straight line material balance |
| $E_c$ | compaction and shrinkage term for straight line material balance |
| $E_g$ | free gas expansion term for straight line material balance |
| $E_w$ | water expansion term for straight line material balance |
| F | underground withdrawal term for straight line material balance |
| G | original gas in-place, scf |
| $G_c$ | initial gas content, scf/ton |
| $G_f$ | volume of free gas in the reservoir, bbl |
| $G_p$ | cumulative gas production, scf |
| k | absolute coal permeability, md |
| $k_{rg}$ | relative permeability to gas |
| $k^*_{rg}$ | relative permeability to gas at critical water saturation |
| $k_{rw}$ | relative permeability to water |
| m | Corey exponent for relative permeability to water |
| n | Corey exponent for relative permeability to gas |
| N | original oil in-place, STB |
| $n_{in}$ | number of $CO_2$ moles flow to the cell |
| $n_{LCO2}$ | $CO_2$ Langmuir adsorption volume |
| $n_{out}$ | number of $CO_2$ moles flow out of the cell |
| p | reservoir pressure, psi |

| | |
|---|---|
| $P_{LCO2}$ | $CO_2$ Langmuir adsorption pressure, psi |
| $P_{LCH4}$ | CH4 Langmuir adsorption pressure, psi |
| $P_{inj}$ | bottom-hole injection pressure, psi |
| $P_L$ | Langmuir adsorption pressure, psi |
| $p_{wf}$ | bottom-hole flowing pressure, psi |
| $q_g$ | gas flowrate, MScf/day |
| R | instantaneous gas water ratio, scf/STB |
| $R_p$ | cumulative produced gas divided by the cumulative produced water ratio, scf/STB |
| $R_s$ | dissolved gas water ratio, scf/STB |
| $R_{soi}$ | initial dissolved gas oil ratio, scf/STB |
| $S_w$ | water saturation, volume fraction |
| $S_{wc}$ | connate water saturation, volume fraction |
| $S_{wi}$ | initial water saturation, volume fraction |
| T | formation temperature, $^oR$ |
| $V_b$ | bulk volume, acre-ft |
| $V_L$ | Langmuir adsorption volume, scf/ton |
| $V_p$ | pore volume, bbl |
| $W_i$ | initial water-in-place, STB |
| $W_f$ | volume of water in the reservoir, bbl |
| $W_p$ | cumulative water production, STB |
| $y_{CO2}$ | $CO_2$ mole fraction |
| $y_{CH4}$ | $CH_4$ mole fraction |
| Z | gas compressibility factor, dimensionless |
| $Z^*$ | King's equation modified gas factor |

**Greek Symbols**

| | |
|---|---|
| ∅ | porosity, volume fraction |
| $\rho_b$ | bulk density, $g/cm^3$ |

| | |
|---|---|
| $\mu_g$ | gas viscosity, cp |
| $\mu_w$ | water viscosity, cp |
| $\in$ | error tolerance |
| $\gamma_{SG}$ | gas interfacial tension to the solid, mN/m |
| $\gamma_{SL}$ | liquid interfacial tension to the solid, mN/m |
| $\gamma_{GL}$ | gas-liquid surface tension, mN/m |

**Subscripts**

| | |
|---|---|
| f | free gas |
| g | gas |
| i | initial conditions |
| j | time step counter |
| r | reference cell |
| s | stabilized conditions |
| L | Langmuir |

**Abbreviations**

| | |
|---|---|
| CA | contact angle |
| CBM | coalbed methane |
| ECBM | enhanced coalbed methane |
| EDS | energy dispersive X-ray spectroscopy |
| EOR | enhanced oil recovery |
| EOS | equation of state |
| TGA | thermogravimetric analysis |

# TABLE OF CONTENTS

Page

# LIST OF FIGURES

Page

# LIST OF TABLES

Page

# CHAPTER I
# INTRODUCTION AND LITERATURE REVIEW

## 1.1 CBM Natural Depletion

According to the U.S. Energy Information Administration (EIA 2013), coalbed methane production in the U.S. in 2013 was 1.5 Tscf, nearly 5% of U.S. gas production that year (EIA 2013). The CBM is considered an unconventional resource where the coal is the source rock and the reservoir rock for the methane (Gray 1987). The performance prediction of CBM reservoirs is challenging due to the complex interactions of storage and transportation mechanisms. The coalbed formations are characterized by their dual porosity: primary (micropores and macropores) and secondary (cleats network) (Laubach et al. 1998). The main difference between conventional reservoirs and the CBM is that in CBM the primary porosity system contains the majority of the gas-in-place as adsorbed gas in the coal matrix, while the cleat network system is usually full of water, and provides the path for mass transfer to the wellbore (Laubach et al. 1998; Shi and Durucan 2004). As a result, the production behavior of the CBM formations greatly differs from conventional gas reservoirs (Gray 1987). The production of CBM formations contains three stages (Gray 1987; Seidle 2011; Ahmed and Meehan 2012). In the dewatering stage, the water flows from the formation and the pressure in the cleat network decreases, which allows gas to desorb from the coal matrix. Once the gas saturation in the cleat network becomes higher than the critical gas saturation, it begins to flow through the cleat network to the producing wells. As the gas desorption from the matrix continues, the gas flow increases dominantly and it reaches its maximum value (peak gas stage). Finally, in the decline stage, the gas flow decreases and the CMB behavior becomes similar to the conventional gas reservoirs. Also, as the gas desorbs from the coal surface, the matrix shrinks. Matrix shrinkage increases cleat width, and the permeability increases (Harpalani and Schraufnagel, 1990).

This complicated behavior of CBM limits the use of common methods, such as decline curves, to predict the gas recovery and the well performance. Some of these

decline curve analyses assume constant operating conditions and static reservoir behavior, these assumptions are usually violated, that leads to incorrect results (Arps 1945). Clarkson explained that CBM wells violate many of the conditions for Arps decline curve analysis (Clarkson 2013). In CBM wells, the Arps b-exponent is not constant during the decline stage. The early performance decline often appears to have exponential decline but in the end becomes more hyperbolic. As a result, the uses of the Arps exponential model early in the production history tended to underestimate gas reserves (Clarkson 2013). Also, some of these decline curves face some difficulties in fitting models with a higher number of unknowns. The numerical reservoir simulators are therefore the best tools for predicting the performance of the CBM reservoirs. The prediction of gas production can be time consuming, expensive, and unreliable if the formation parameters are unavailable. Analytical models and history matching can be used efficiently to estimate the reservoir parameters and predict production performance.

The Material Balance Equation (MBE) describes the production behavior of the oil and gas reservoirs. Material balance equations are used to define the performance of oil and gas reservoirs. For conventional oil reservoirs, it has the following form:

$$\mathbf{N}(\mathbf{B_t}-\mathbf{B_{ti}})+\mathbf{G}\left(\mathbf{B_g}-\mathbf{B_{gi}}\right)+\mathbf{NB_{ti}}\left[\frac{\mathbf{c_w}\,\mathbf{s_{wi}}+\mathbf{c_f}}{\mathbf{1}-\mathbf{s_{wi}}}\right]\Delta\overline{\mathbf{P}}=\mathbf{N_p}\left[\mathbf{B_t}+\mathbf{B_g}\left(\mathbf{R_{po}}-\mathbf{R_{soi}}\right)\right] \quad (1\text{-}1)$$

And for gas reservoirs:

$$\mathbf{G}\left(\mathbf{B_g}-\mathbf{B_{gi}}\right)+\mathbf{GB_{gi}}\left[\frac{\mathbf{c_w}\,\mathbf{s_{wi}}+\mathbf{c_f}}{\mathbf{1}-\mathbf{s_{wi}}}\right]\Delta\overline{\mathbf{P}}=\mathbf{G_pB_g}+\mathbf{W_pB_w} \quad (1\text{-}2)$$

To derive these equations, it is assumed that the reservoir temperature is constant; there is equilibrium reservoir pressure (the porosity, the permeability, and the fluid saturations are the same throughout the entire reservoir); there is a constant reservoir bulk volume; the fluid and reservoir rock are nonreactive; and the production, pressure and PVT data are available (Craft et al. 1959).

Various forms of MBEs for CBM and shale gas formations have been developed (King 1990, 1993; Seidle 1999; Clarkson and McGovern 2001; Ahmed et al. 2006;

Williams-Kovacs et al. 2012). These equations account for the assumptions of the material balance equation for conventional reservoirs with considering the adsorbed gas. In addition, it assumes equilibrium between the free gas in the pores and the adsorbed gas on the matrix. These equations account for the formation compressibility and the fluid compressibility effects; however, they do not account for matrix shrinkage and methane-in-water solubility.

Different authors discussed the effect of matrix shrinkage on formation permeability, especially when the formation pressure is depleted (Harpalani and Schraufnagel 1990; Powwas 1998; Shi and Durucan 2005; Palmer 2009; Clarkson et al. 2010; Liu et al. 2011; Liu and Harpalani 2013b; Zhu et al. 2013). The gas desorption shrinks the coal matrix and increases cleat width, which in turn increases the absolute permeability. Also, matrix shrinkage improves relative permeability to gasses. As the volume of the cleat network increases, while the water volume is constant, the water saturation decreases and relative permeability to gasses increases.

## 1.2 ECBM and $CO_2$ Sequestration

Carbon dioxide ($CO_2$) is the major greenhouse gas emitted from all activities. In 2012, $CO_2$ accounted for 85% of all U.S. greenhouse gas emissions (State 2010).The combustion of fossil fuels (coal, natural gas, and oil) for energy and transportation is the main human activity that emits $CO_2$ (Houghton et al. 2001; State 2010). $CO_2$ sequestration is one of the effective ways to reduce $CO_2$ emissions. Different authors have discussed the applicability of $CO_2$ sequestration in underground formations (depleted oil reservoirs, saline water aquifers, or salt caverns), in order to reduce the effect of global warming and also to enhance oil recovery (EOR) (Espie 2005; Benson and Cole 2008; Pilisi et al. 2010; Mohamed and Nasr-El-Din 2013).

$CO_2$ has been sequestrated in coal seams to enhance the coalbed methane production (ECBM) in addition to $CO_2$ storage (Seidle 2000; Mavor et al. 2002; Schroeder et al. 2002; Busch et al. 2003; Garduno et al. 2003). A coalbed is characterized by its dual porosity: primary (micropores and macropores) and secondary (cleats network). The

primary porosity system contains the majority of the gas-in-place as adsorbed gas in the coal matrix, while the secondary porosity system provides the conduit for mass transfer to the wellbore and is usually full of water. The gas flow mechanism can be summarized in three stages: (1) desorption: once water is produced from the cleat network system, the formation pressure will be declined, and the gas will be desorbed from the matrix surface, which can be described by Langmuir isotherm equation; (2) diffusion: gas will diffuse from coal matrix to cleat network due to the gas concentration difference; (3) Darcy's flow: gas in the cleats and natural fractures will flow to the wellbore by Darcy's flow (Gray 1987; Laubach et al. 1998).

$CO_2$ can be stored within the coal seams by three mechanisms: (1) stratigraphic and structural trapping (as a free phase in the pores), (2) hydrodynamic trapping (as a dissolved gas in water), and (3) adsorption trapping (as adsorbed gas on the organic surface). The adsorbed gas phase is more dominant in the case of coal formations (He et al. 2013). As $CO_2$ is injected into the coal formation, it will replace the methane on the coal surface due to its higher affinity to the coal matrix than methane. Busch et al. (2003) reported the ratios of the final sorption capacities for pure $CO_2$ and methane (in molar units) on the five coal samples varied between 1.15 and 3.16. Battistutta et al. (2010) determined the adsorption isotherms of $CO_2$, $CH_4$, and $N_2$ and found that the adsorption ratio between the maximum in the excess sorption $N_2$:$CH_4$:$CO_2$ was 1:1.5:2.6.

Both $CO_2$ adsorption and $CH_4$ desorption affect coal permeability. $CH_4$ desorption shrinks the coal matrix and increases cleat width, which in turn increases the absolute permeability. Opposite effects can be expected when $CO_2$ is adsorbed by coal. Previous research work has shown that the coal swells when exposed to carbon dioxide (McKee 1987; Harpalani and Schraufnagel 1990; Palmer 2009; Battistutta et al. 2010; Liu and Harpalani 2013a, 2013b).

$CO_2$ has been sequestrated in unmineable coal seams to enhance coalbed methane production (ECBM), in addition to $CO_2$ storage (Seidle 2000; Mavor et al. 2002; Garduno et al. 2003). In general, the coal structure consists of a cleat network system (> 50 nm) and a coal matrix system (< 50 nm). The cleat system is initially filled with water, and it

provides the flow path for fluid production by Darcy flow. The matrix system provides the storage for the gasses, and the gas diffusion dominates the gas flow. During the primary recovery of coalbed methane (CBM), water must be drained prior to gas production so that the reservoir pressure can be lowered and the gas can desorb from the internal matrix. Once desorbed gas enters the cleats and reaches the irreducible gas saturation, gas and water flow simultaneously in the cleats. In the ECBM process, nitrogen, $CO_2$ or their binary mixture inject into coalbeds to enhance CBM production and ultimate methane recovery.

As $CO_2$ is injected into the coal formation, it will replace the methane on the coal surface due to the higher affinity of $CO_2$ to the coal matrix than to methane. (Busch et al. 2003) reported the ratios of the final sorption capacities for pure $CO_2$ and methane (in molar units) on the five coal samples varying between 1.15 and 3.16. (Battistutta et al. 2010) determined the adsorption isotherms of $CO_2$, $CH_4$, and $N_2$ and found that the adsorption ratio between the maximum in the excess sorption, $N_2$:$CH_4$:$CO_2$, is 1:1.5:2.6. The Langmuir equation can be used to describe the adsorption behavior.

$$\mathbf{V_{adsorbed}} = \frac{\mathbf{V_L p}}{\mathbf{p + p_L}}, \qquad 1\text{-}3$$

$V_L$ is Langmuir adsorption volume (scf/ton), P is formation pressure (psi), $P_L$ is Langmuir adsorption pressure (psi), and $V_{adsorbed}$ is adsorbed gas volume (scf/ton).

Multiphase flow occurs at reservoir conditions for both primary and enhanced coalbed methane recovery processes. The effective permeabilities of water and gas dominate the ratio of fluid flows rather than the absolute permeability. Relative permeability, the ratio of the effective permeability to the absolute permeability of the porous media, characterizes the flow capacity for one fluid during a simultaneous filtration of multiphase systems in the petroleum industry (Clarkson et al. 2011).

$CO_2$ adsorption and $CH_4$ desorption affect the coal permeability. $CH_4$ desorption shrinks the coal matrix and increases cleat width, which increases the absolute permeability. Opposite effects can be expected when $CO_2$ is adsorbed on the coal surface.

$CO_2$ adsorption swells the coal matrix and decreases the absolute permeability. Previous work has shown that the coal swells when exposed to carbon dioxide (Harpalani and Schraufnagel 1990; Palmer 2009; Battistutta et al. 2010; Liu and Harpalani 2013a).

Different studies presented core flooding experiments for $CO_2$ injection in coal cores for ECBM and $CO_2$ sequestration purpose (Shimada et al. 2005; Mazumder et al. 2008; Yu et al. 2008; Zhao et al. 2011; Zhou et al. 2013). These studies neglected the presence of water in coal cores and the multiphase flow effects on the performance. Other studies highlighted that the $CH_4$ desorption decreased in higher water-saturated conditions (Crosdale et al. 2008; Le Gal et al. 2012). These studies did not investigate the effect of water salinity and the injection of flue gas on the performance of $CO_2$ sequestration. Coal seam water usually has low salt concentrations that vary between 800 to 28,000 ppm (Hamawand et al. 2013).

### 1.3 Coal Wettability

Carbon dioxide sequestration is one of the most effective ways to reduce $CO_2$ in the environment. Different authors have discussed the applicability of $CO_2$ sequestration in underground formations (depleted oil reservoirs,(Espie 2005) saline water aquifers,(Mohamed and Nasr-El-Din 2013) or salt caverns(Dusseault et al. 2004)) to reduce the effect of global warming and also to enhance oil recovery (EOR). Geological sequestration of $CO_2$ in coal seams has become an attractive technology for two reasons. First, the injection of $CO_2$ or mixtures of $CO_2$ and $N_2$ enhances methane production from coalbeds (ECBM). Second, it reduces the effect of global warming by storing $CO_2$.(Busch et al. 2003; Garduno et al. 2003)

The efficiency of the ECBM and $CO_2$ sequestration process is dependent on the wettability behavior of the coal–water–$CO_2$ system. It depends specifically on the $CO_2$ diffusion rate from the cleat network, through the micro-cleats, to the surface of the coal matrix. If the coal is gas-wet (hydrophobic), then the gas will fill the smaller pores (Mazumder et al. 2003; Plug et al. 2008; Saghafi et al. 2014) which leads to a faster diffusion of the injected gas to the coal surface (diffusion coefficient of $CO_2 = 1.7\times10^{-7}$

$m^2/s$) (Plug et al. 2008). If the coal is water-wet (hydrophilic), then the water will fill the smaller pores, which decreases the $CO_2$ diffusion (from the main cleats) to the coal surface through the water (diffusion coefficient of $CO_2 = 2\times10^{-9}$ $m^2/s$) (Plug et al. 2008).

Wettability studies usually use the contact angle measurements as a simple and reliable method to characterize the degree of wetting when a solid and liquid interact (Kwok and Neumann 1999). The wettability behavior of coal was investigated in the literature based on contact angle measurements for coal–water–air systems (Siemons et al. 2006; Sakurovs and Lavrencic 2011; Shojai Kaveh et al. 2012). It was found that the coal rank and its maceral type highly affect the coal wettability behavior. The main groups of coal macerals are vitrinite, exinite, and inertinite. These macerals have different oxygen-containing polar groups such as carboxyl (COOH), hydroxyl (OH), and methoxyl ($OCH_3$) groups. It was found that the coal becomes more water-wet (decreasing the hydrophobicity) with decreasing rank, carbon content, and with increasing oxygen-containing groups. In other words, the lower the coal rank (lower carbon content and higher oxygen-containing groups), the lower the contact angle (lower hydrophobicity).

The wettability behavior of coal depends on the pressure, and its effect is a function of the coal rank (Siemons et al. 2006; Sakurovs and Lavrencic 2011; Shojai Kaveh et al. 2012). Sakurovs and Lavrencic (2011) and Shojai et al.(2012) investigated the wettability behavior for different coal ranks at different pressures up to 1500 psi. For high-ranking coal, the wettability was modulated from water-wet to gas-wet with $CO_2$ injection at higher pressures. Siemons et al.(2006) indicated that coal was water-wet at atmospheric pressure and then turned into gas-wet at pressures greater than 375 psi.

Sakurovs and Lavrencic ( 2011) and Shojai et al.(2012) showed that the wettability behavior of $CO_2$ in wet coal was dependent on the $CO_2$ adsorption behavior instead of other $CO_2$ properties, such as solubility and density. They found that the $CO_2$-coal wetting behavior was affected by the adsorption of $CO_2$ on the coal surface, and that the surface tension between water and coal decreased due to adsorption.

The injected gas composition also affected the wettability behavior. Shojai et al.(2011) investigated the wetting behavior of flue gasses (73 mol% $N_2$, 11 mol% $CO_2$,

and impurities). They found that the contact angle values of flue gasses on the coal surface were generally smaller than those of $CO_2$. Shojai et al.(2012) showed experimental results for flue gas (80 mol% $N_2$, 20 mol% $CO_2$) coal wettability measurements where the wettability of coal was intermediate-wet at all pressures, and the contact angle only slightly increased with increasing pressure.

Rock wettability depends on the stability of water layer surrounding the rock surface, which is a function of the zeta potential. Zeta potential is the electrical potential that develops at the interface between a solid and a liquid in response to the relative movement of solid particles and water. When small particles are dispersed in solutions, a charged interface between the surfaces of the particles and the bulk liquid will develop. The dispersion stability, or the tendency of particles not to aggregate, is dependent on the magnitude of the zeta potential of the particles. As the zeta potential value nears zero, the dispersions will become unstable and will aggregate or flocculate to form larger particles.

Coal-seam water usually has low salt concentrations that vary between 800 to 28,000 ppm (Hamawand et al. 2013). No study was found on the effect of salt concentration on coal wettability. However, other studies show the effect of salt concentration on $CO_2$ wettability in conjunction with other minerals (calcite, quartz, feldspar, and mica) (Chiquet et al. 2007; Farokhpoor et al. 2013). Chiquet et al. (2007) and Farokhpoor et al.(2013) showed that an increase in the salt concentration made feldspar and muscovite mica less water-wet. These researchers also showed that this effect was limited in the cases of quartz and calcite.

## 1.4 Objectives

The main objectives of this work are to: (1) develop an integrated model to simulate the b behavior of CBM. A developed generalized material balance equation will be used to account for the solubility of the methane in water, and the changes of porosity and permeability with pressure depletion., (2) Extend the model to simulate the performance of ECBM, (3) evaluate the role of brine salinity, formation pressure and gas composition on the $CO_2$-water-coal wettability, and (4) examine the effect of the water

salinity, gas composition, formation pressure, and injection flow rate on the performance of $CO_2$ sequestration in coal cores.

# CHAPTER II

# A COMPREHENSIVE MODEL TO HISTORY MATCH AND PREDICT GAS/WATER PRODUCTION FROM COAL SEAM[1]

This chapter presents a model that can be used as a prediction or a history matching tool for coalbed methane (CBM) performance. It can be used to match the production data to estimate the formation properties, which can then be used to predict future reservoir performance.

## 2.1. Model Description

The objectives of the model were to history match and predict the performance of the CBM formations. First, a forward model was developed for the rate-time performance prediction of the well. In the case of the formation parameters were not available, the model was inverted in order to use the rate time production history to obtain the reservoir properties that will be used to predict the future performance (**Fig. 2-1**).

The developed model assumes that each well is treated individually and the estimated parameters, gas content and pore volume, will give the values for the drainage area of the well. Well interferences were neglected in this work.

[1] Reprinted with permission from "A comprehensive model to history match and predict gas/water production from coal seams" by Ibrahim, A. F., Nasr-El-Din, H. A. 2015. International Journal of Coal Geology **146** (01): 79-90, Copyright 2015 by Elsevier B.V.

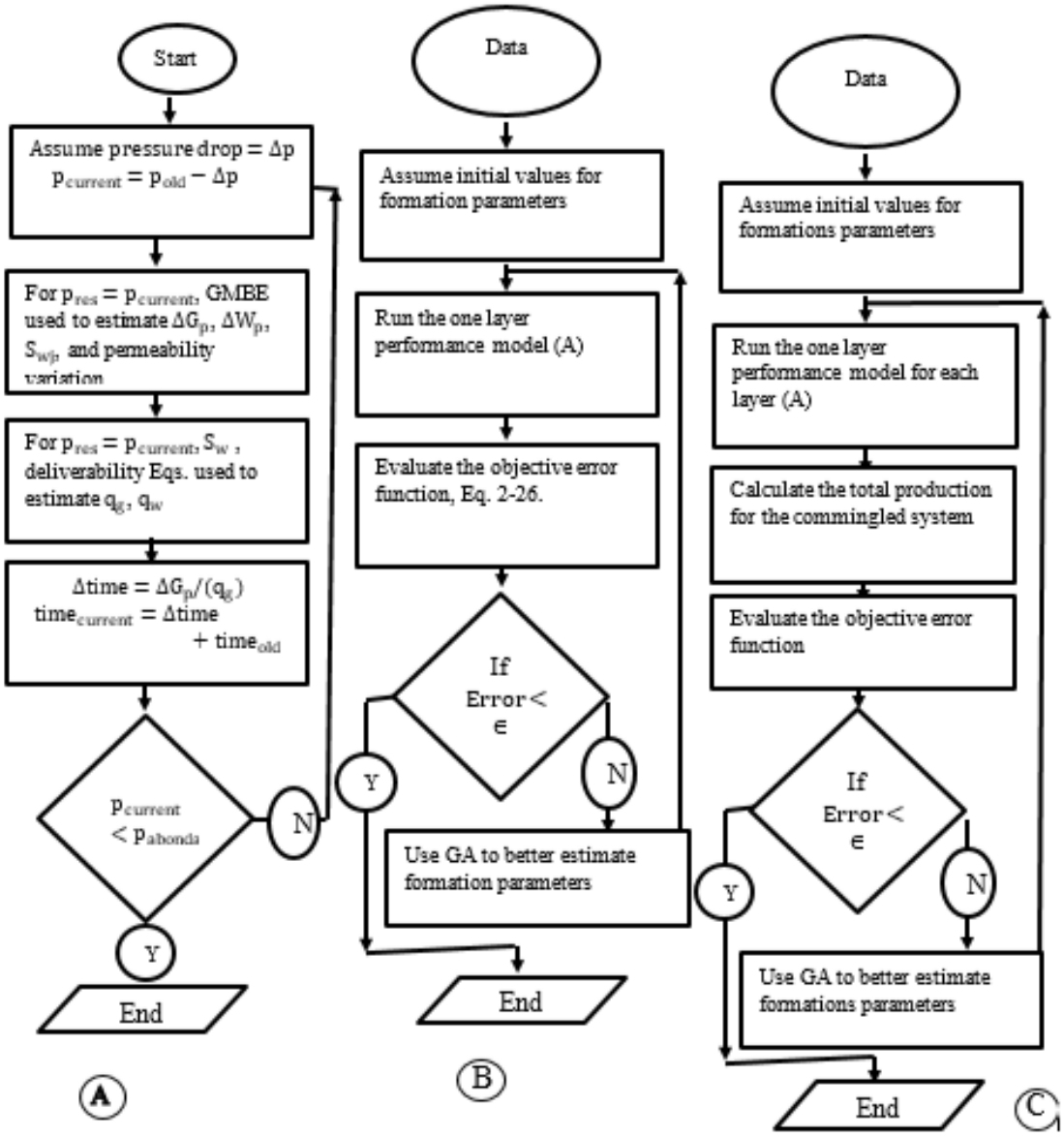


**Fig. 2-1 Flow chart for the model; A) the forward one layer model, B) the inverted one layer model, and C) the inverted commingled layered model.**

## The Generalized Material Balance Equation (GMBE)

The aim of the GMBE is to predict the CBM performance with pressure depletion by predicting the water saturation in the reservoir, the incremental water and gas production with a drop in pressure.

A GMBE is developed in order to account for the porosity variation due to matrix shrinkage and formation compressibility, and the solubility of methane in water. The tank model concept was used to develop the GMBE (**Fig. 2-2)**. It is based on a volumetric balance where the pore volume at any pressure or time is equal to the summation of free water and gas volumes. This means that the change in the pore volume is equal to the summation of changes in the free water volume and the free gas volume with pressure depletion.

$$\Delta \mathbf{V_p} = \Delta \mathbf{W_f} + \Delta \mathbf{G_f} \qquad 2\text{-}1$$

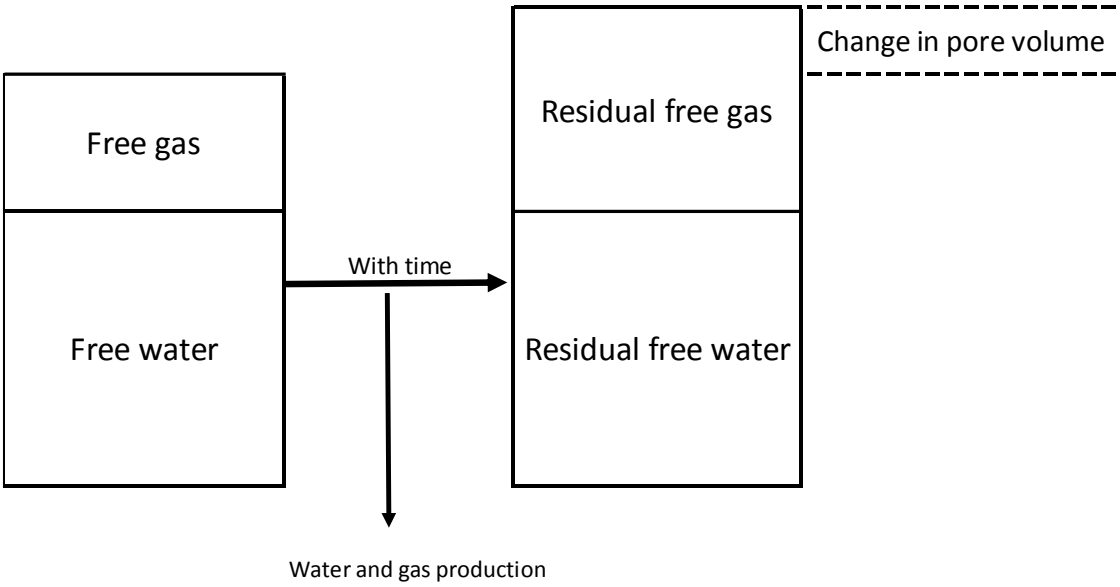


**Fig. 2-2 The tank model concept that was used to develop the general material balance equation.**

The reservoir pore volume changes due to formation compaction and matrix shrinkage. According to (Harpalani and Schraufnagel 1990; Palmer 1998; Shi and Durucan 2005; Palmer 2009; Clarkson et al. 2010; Liu and Harpalani 2013b), the change in porosity, $\Delta\emptyset$, can be calculated as follows:

$$\Delta\emptyset = \emptyset_{\mathbf{i}}\left(\mathbf{c_f}\Delta\overline{\mathbf{P}} - \mathbf{c_s}\Delta\mathbf{P}^*\right) \quad 2\text{-}2$$

Where,

$$\Delta\mathbf{P}^* = \left[\frac{\mathbf{P_i}}{\mathbf{P_i}+\mathbf{P_L}} - \frac{\mathbf{P}}{\mathbf{P}+\mathbf{P_L}}\right], \text{ and } \quad \Delta\overline{\mathbf{P}} = \mathbf{P_i} - \mathbf{P} \quad 2\text{-}3$$

$\mathbf{c_f}$ is the formation compressibility. $c_s$ is the matrix shrinkage coefficient, which is a function of the formation mechanical properties and the gas properties. The history matching technique can be used to determine $c_s$.

The absolute permeability can be predicted as a function of porosity (McKee 1987; Palmer 1998; Zhou et al. 2013) as follows:

$$\frac{\mathbf{k}}{\mathbf{k_i}} = \left(\frac{\emptyset}{\emptyset_{\mathbf{i}}}\right)^{\mathbf{3}} \quad 2\text{-}4$$

By assuming a constant bulk volume, the change in the pore volume can be calculated as follows:

$$\Delta\mathbf{V_p} = \mathbf{V_{pi}}\left(\mathbf{c_f}\Delta\overline{\mathbf{P}} - \mathbf{c_s}\Delta\mathbf{P}^*\right) \quad 2\text{-}5$$

The water volume in the reservoir changed due to water expansion and production.

$$\Delta\mathbf{W_f} = \mathbf{W}_{\boldsymbol{i}}\mathbf{B_{wi}} - \left(\mathbf{W_i} - \mathbf{W_p}\right)\mathbf{B_w} \quad 2\text{-}6$$

The change in the free gas volume is described by **Eqs. 2-7 – 2-10**. It is equal to the difference between the initial free gas in the reservoir and the current residual free gas.

$$\Delta\mathbf{G_f} = \mathbf{G_{fi}} - \mathbf{G_{fr}} \quad 2\text{-}7$$

$$\mathbf{G_{fi}} = \mathbf{G_f}\mathbf{B_{gi}} \quad 2\text{-}8$$

The current residual free gas volume is equal to the initial free gas volume minus the produced gas with the addition of free gas from the adsorbed gas phase and the dissolved methane in the water phase.

The free gas added from the adsorbed phase can be handled by the Langmuir equation (Langmuir 1916).

$$\text{The free gas added from the adsorbed phase} = \rho_b V_b\left(G_c - \frac{V_L P}{P+P_L}\right)$$

Where, $G_c$ is the initial gas content.

The free gas added from the dissolved gas phase with pressure depletion = $W_i R_{si} - \left(W_i - W_p\right)R_s$

$$G_{fr} = B_g\left[G_{fi} - G_p + W_i R_{si} - (W_i - W_p)R_s + \rho_b V_b\left(G_c - \frac{V_L P}{P+P_L}\right)\right] \quad 2\text{-}9$$

$$\Delta G_f = G_f B_{gi} - B_g\left[G_{fi} - G_p + W_i R_{si} - (W_i - W_p)R_s + \rho_b V_b\left(G_c - \frac{V_L P}{P+P_L}\right)\right] \quad 2\text{-}10$$

By using the following definitions:

$$V_{pi} = \frac{W_I B_{wi}}{S_{wi}} = \frac{G_{fi} B_{gi}}{1-S_{wi}} \quad 2\text{-}11$$

$$B_t = B_w + B_g(R_{si} - R_s) \quad 2\text{-}12$$

$$R_p = \frac{G_p}{W_p} = \frac{\sum_0^t \Delta W_p R}{\sum_0^t \Delta W_p} \quad 2\text{-}13$$

Instantaneous gas water ratio, R, can be calculated from **Eq. 2-14**:

$$R = \frac{k_{rg}}{k_{rw}} \times \frac{B_w}{B_g} \times \frac{\mu_w}{\mu_g} + R_s \quad 2\text{-}14$$

The gas to water relative permeability ratio is a function of water saturation (Aminian and Ameri, 2009).

$$\frac{k_{rg}}{k_{rw}} = f(S_W) \quad 2\text{-}15$$

The water saturation is the residual water volume divided by the current pore volume. It is a function of the fractional water production and the change in porosity.

$$S_W = \frac{[1+C_w \times (P_i - P)] - \frac{W_p \times B_w}{W_i}}{(1 - c_f \Delta\overline{P} + c_s \Delta P^*)} \quad 2\text{-}16$$

By substituting in the volumetric balance (Eq. 2-1), the GMBE will be:

$$\mathbf{W_I(B_{wt} - B_{wti}) + W_I B_{wti}\left[\frac{1-s_{wi}}{s_{wi}}\right]\left[\frac{B_g - B_{gi}}{B_{gi}}\right] + W_I B_{wti}\left[\frac{c_f \Delta\overline{P} - c_s \Delta P^*}{s_{wi}}\right] +}$$

$$\mathbf{1359.7\ \rho_b V_b B_g\left[G_c - \frac{V_L P}{P+P_L}\right] = W_p\left[B_w + B_g(R_p - R_s)\right]} \qquad 2\text{-}17$$

**Eq. 2-17** is similarly formatted to the conventional material balance of oil reservoirs. The left-hand side of Eq. 2-17 represents the production driving forces. These driving forces are water and dissolved gas expansion force, free gas expansion force, net formation compaction force (formation compressibility - matrix shrinkage), and gas desorption force. The right-hand side of Eq. 2-17 refers to the water and gas production.

Eqs. 13 to 17 can be solved by using Tarner's solution procedures, a false position iteration method, to predict the performance with pressure depletion (Tarner 1944) (Appendix A).

By assuming that water is a slightly compressible fluid, then:

$$\mathbf{c_w B_{wti} \Delta\overline{P} = (B_{wt} - B_{wti})} \qquad 2\text{-}18$$

Eq. 2-19 becomes:

$$\mathbf{W_I B_{wti}\left[\frac{1-s_{wi}}{s_{wi}}\right]\left[\frac{B_g - B_{gi}}{B_{gi}}\right] + W_I B_{wti}\left[\frac{(c_f + c_w s_{wi})\Delta\overline{P} - c_s \Delta P^*}{s_{wi}}\right] + 1359.7\ \rho_b V_b B_g\left[G_c - \frac{V_L P}{P+P_L}\right] =}$$

$$\mathbf{W_p\left[B_w + B_g(R_p - R_s)\right]} \qquad 2\text{-}19$$

In terms of free gas in-place and cumulative gas production Eq. 2-19 can be formatted as follows;

$$\mathbf{G_{fi}\left[B_g - B_{gi}\right] + G_{fi} B_{gi}\left[\frac{(c_f + c_w s_{wi})\Delta\overline{P} - c_s \Delta P^*}{1-s_{wi}}\right] + 1359.7\ \rho_b V_b B_g\left[G_c - \frac{V_L P}{P+P_L}\right] = \frac{G_p}{R_p}\left[B_w +\right.}$$

$$\mathbf{\left. B_g(R_p - R_s)\right]} \qquad 2\text{-}20$$

In cases of no free gas at initial conditions where the initial water saturation is equal to 1, Eq. 2-17 can be reduced to;

$$\mathbf{W_I B_{wti}}\left[(\mathbf{c_f + c_w})\Delta\overline{\mathbf{P}} - \mathbf{c_s}\Delta\mathbf{P}^*\right] + \mathbf{1359.7\,\rho_b V_b B_g}\left[\mathbf{G_c} - \frac{\mathbf{V_L P}}{\mathbf{P+P_L}}\right] = \mathbf{W_p}\left[\mathbf{B_w} + \mathbf{B_g}\left(\mathbf{R_p} - \mathbf{R_s}\right)\right] \quad 2\text{-}21$$

In cases of dry coal at initial conditions, Eq. 2-17 can be written as:

$$W_p \text{ and } W_i \approx 0$$

$$\mathbf{G_{fi}}\left[\mathbf{B_{gi}} - \mathbf{B_g}\right] + \mathbf{G_{fi} B_{gi}}\left[\mathbf{c_f}\Delta\overline{\mathbf{P}} - \mathbf{c_s}\Delta\mathbf{P}^*\right] + \mathbf{1359.7\rho_b V_b B_g}\left[\mathbf{G_c} - \frac{\mathbf{V_L P}}{\mathbf{P+P_L}}\right] = \mathbf{G_p B_g} \quad 2\text{-}22$$

**Deliverability Equation**

The two-phase flow analysis in coalbed methane reservoirs differs from conventional gas reservoirs. In conventional reservoirs, the gas-in-place is stored in the pore space and it is a function of the porosity, pressure, and water saturation. There is usually little or no mobile water in the conventional gas reservoirs (assuming volumetric reservoir conditions). Therefore, the relative permeability is not a significant factor in the performance of the conventional gas reservoirs. On the other hand, coalbed methane reservoirs consist of coal matrix blocks, which are separated by cleats. At initial conditions, the cleat system is usually 100% saturated with water. As production begins, only water flows into the wellbore through the cleat system. When the reservoir pressure drops below the desorption pressure, gas desorbs from the coal and flows in the cleat system with the water to the wellbore (Chen et al. 2013). The two-phase flow was considered through the gas and water relative permeabilities. Corey equations were used to determine the relative permeability curves (Enoh 2007; Aminian and Ameri 2009) as follows:

$$\mathbf{K_{rg}} = \mathbf{K^*_{rg}}(\mathbf{1} - \boldsymbol{s_w}^*)^{\mathbf{n}} \quad 2\text{-}23$$

$$\mathbf{K_{rw}} = (\boldsymbol{s_w}^*)^{\mathbf{m}} \quad 2\text{-}24$$

$$\mathbf{s_w}^* = \frac{\mathbf{s_w - s_{wc}}}{\mathbf{1 - s_{wc}}}$$

The history matching technique can be used to determine Corey exponents (n, m).

Al-Hussainy et al. (1966) defined the pseudo-integral pressure to consider the

variation of gas compressibility and viscosity with pressure. The two-phase pseudo-integral pressure, $\Delta\mathbf{m}(\mathbf{p})$, is used to account for the two-phase flow effect.

$$\Delta\mathbf{m}(\mathbf{p}) = \int_{\mathbf{p_{wf}}}^{\mathbf{p}} \left[\frac{\mathbf{K_{rw}}}{\mu_{\mathbf{w}}\mathbf{B_w}}\mathbf{R_s} + \frac{\mathbf{K_{rg}}}{\mu_{\mathbf{g}}\mathbf{B_g}}\right]\mathbf{dp} \qquad 2\text{-}25$$

Where $\frac{K_{rw}}{\mu_w B_w} R_s$ represents the flow of the dissolved gas in water, and $\frac{K_{rg}}{\mu_g B_g}$ represents the flow of the free gas.

**Automatic History Matching**

The model is combined with a genetic algorithm (GA) routine to estimate the initial gas content, formation permeability, porosity, the Corey exponents for relative permeability curves, and the matrix shrinkage coefficient that gives the best match with the actual production history. The analysis is carried out by assuming values for these parameters and calculating the total performance (gas rate and water rate versus time) for the system. The error in the performance can then be calculated by Eq. 2-26:

$$\mathbf{Error} = \frac{\mathbf{1}}{\mathbf{2N}_d}\left[\sum_{\mathbf{1}}^{\mathbf{N}_d}\left|\frac{\mathbf{q_{g_{observed}} - q_{g_{model}}}}{\mathbf{q_{g_{observed}}}}\right| + \sum_{\mathbf{1}}^{\mathbf{N}_d}\left|\frac{\mathbf{q_{w_{observed}} - q_{w_{model}}}}{\mathbf{q_{w_{observed}}}}\right|\right] \qquad 2\text{-}26$$

Where, $N_d$ is the number of the total data points used in the matching period. This error can be treated as an objective function for the GA routine (Holland 1975). The procedure of the GA is as follows:

1. Set maximum and minimum values for the unknowns (formation parameters).
2. Generate random population of solutions (x) for the problem (within the maximum and the minimum values for each parameter).
3. Calculate the error of each solution (x) in the population.
4. Create a new population by repeating the following steps:

   4.1. Select two-parent solutions from the previous population according to their error (the lower the error, the bigger the chance to be selected).

   4.2. With a crossover probability, cross over the parents to form new offspring. If no crossover was performed, offspring is the exact copy of

parents.

4.3. With a mutation probability, mutate new offspring at each locus (position in the chromosome).

4.4. Place new offspring in the new population.

5. Use the newly generated population for a further run of the algorithm.
6. Repeat the steps (3 through 5) to satisfy the end conditions, stop, and return the best solution in the current population.

Two end conditions were set for the GA. The first condition was that the objective function error reached the tolerance (0.01). The second condition was that the number of runs (iterations) reached the maximum number (100).

As the number of unknowns increases, it is better to reduce the difference between the maximum and the minimum values to obtain a better estimation. In order to do that, wide ranges for the parameters were set to obtain initial estimation. This estimation was then used to set a narrow range for the parameters for a better estimation.

In the case of a commingled system, the model (as a single layer model) can be used to match the total production from all layers. Weighted average values for the formation parameters can be estimated. Also, the developed model (as a multilayer model) can be used to estimate the individual parameters for each layer (Fig. 2-1). The following procedure was used:

1. Assume initial values for formation parameters for each layer.
2. Run the single layer model for each layer using the $p_{wf}$ estimated for the commingled well and obtain individual layer gas and water rates (versus time).
3. Obtain the total production rate of the commingled system by summing the rates of individual layers.
4. Evaluate the error (objective function), which is defined by Eq. 2-26.
5. Optimize the formations parameters to minimize the error.

**Tarner procedure to solve the material balance equation**

1. Assume incremental reservoir pressure drop $= \Delta p$,
   So $p_j = p_{(j-1)} - \Delta p$ .
2. For $p = p_j$ obtain the corresponding PVT data
3. Assume incremental water production ($\Delta w_{pj}$) corresponding to $\Delta p$.
   $W_{pj} = W_{pj-1} + \Delta W_{pj}$
4. Calculate water saturation at $p_j$ using Eq. 2-16.
5. Calculate instantaneous gas water ratio ($R_j$) from Eq. 2-14.
6. Calculate average gas water ratio. $R_{avg} = \frac{R_j + R_{j-1}}{2}$
7. Calculate the incremental gas production ($\Delta G_{pj}$) corresponding to $\Delta W_{pj}$.
   $\Delta G_{pj} = \Delta W_{pj} R_{avg}$ So $G_{pj} = G_{pj-1} + \Delta G_{pj}$
8. Calculate the cumulative gas-water ratio: $R_p = \frac{G_{pj-1} + \Delta G_{pj}}{W_{pj}}$
9. Calculate the cumulative water production,$W_{pj}$, using Eq. 2-17.
10. Calculate the incremental water production. $\Delta W_{pj} = W_{pj} - W_{p(j-1)}$
11. Calculate the error between $\Delta W_{pj}$ in steps 10 and 3.
12. Repeat the calculation steps (3 through 11) to achieve error < $\in$.

**Linearization of the developed MBE**

Eq. 2-17 can be formatted as a straight line as follows:

$$\mathbf{W_i \frac{(Ew + Eg + Ec)}{Ea} + 1359.7\, \rho_b V_b V_L = \frac{F}{Ea}} \qquad \text{2-27}$$

Where,

$$\mathbf{F = W_p\left[B_w + B_g\left(R_p - R_s\right)\right]} \qquad \text{2-28}$$

$$\mathbf{Ew = \left(B_{wt} - B_{wti}\right)} \qquad \text{2-29}$$

$$\mathbf{Eg} = \mathbf{B_{wti}}\left[\frac{\mathbf{1-s_{wi}}}{\mathbf{s_{wi}}}\right]\left[\frac{\mathbf{B_g-B_{gi}}}{\mathbf{B_{gi}}}\right] \quad 2\text{-}30$$

$$\mathbf{Ec} = \mathbf{B_{wti}}\left[\frac{\mathbf{c_f\Delta\overline{P}-c_s\Delta P^*}}{\mathbf{s_{wi}}}\right] \quad 2\text{-}31$$

$$\mathbf{Ea} = \mathbf{B_g}\left[\frac{\mathbf{P_i}}{\mathbf{P_i+P_L}} - \frac{\mathbf{P}}{\mathbf{P+P_L}}\right] \quad 2\text{-}32$$

Eq. 2-27 can be plotted as a straight line as the X-axis is $\frac{(\mathbf{Ew}+\mathrm{Eg}+\mathrm{Ec})}{\mathrm{Ea}}$, and the Y-axis is $\frac{\mathrm{F}}{\mathrm{Ea}}$. From this plot, the slope is $W_i$ and the Y-intercept is $1359.7\ \rho_b V_b V_L$. The original gas in-place can be calculated as follows:

$$\mathbf{G} = \mathbf{1359.7}\ \boldsymbol{\rho_b V_b V_L}\frac{\mathbf{P}_i}{\mathbf{P_i+P_L}} \quad 2\text{-}33$$

## 2.2. Hypothetical Application Cases

The model was verified against different hypothetical cases. A commercial reservoir simulator (CMG-GEM) was used to generate production data for the hypothetical cases. The reservoir properties and the relative permeability data that were used to build the hypothetical cases are given in **Tables 2-1** and **2-2**, respectively (Mora 2007). Several cases were used to verify the model at various water saturation and different production conditions. The verification was conducted using water and gas production rates versus time from simulator results as input data for the integrated model. The integrated model was run in the history matching mode for a production period to obtain the reservoir parameters. These parameters were then used to predict future performance.

| Parameter | Value |
|---|---|
| Initial reservoir pressure, psia | 701 |
| Gas composition ($CH_4$) | 100% |
| Reservoir temperature, °F | 104 |
| Reservoir depth, ft | 2500 |
| Reservoir permeability, md | 20 |
| Reservoir porosity, volume fraction | 0.01 |
| Reservoir thickness, ft | 40 |
| Reservoir area, acres | 83 |
| Coal bulk density, $g/cm^3$ | 1.43 |
| Langmuir adsorption volume, $V_L$, scf/ton | 449.7 |
| Langmuir adsorption pressure, $p_L$, psi | 500.4 |
| Initial gas content, scf/ton | 269.7 |

Table 2-1 The reservoir properties for the hypothetical cases (Mora 2007).

| $S_w$ | $k_{rg}$ | $k_{rw}$ |
|---|---|---|
| 1 | 0.0 | 1.00 |
| 0.9 | 0.01 | 0.60 |
| 0.8 | 0.05 | 0.39 |
| 0.7 | 0.08 | 0.24 |
| 0.6 | 0.15 | 0.15 |
| 0.5 | 0.21 | 0.08 |
| 0.4 | 0.29 | 0.05 |
| 0.3 | 0.40 | 0.02 |
| 0.2 | 0.53 | 0.01 |
| $S_{wc} = 0.1$ | 0.72 | 0 |
| 0 | 1 | 0 |

Table 2-2 The relative permeability data for the hypothetical cases (m = 3.9 and n = 2.07).

**Hypothetical Case #1**

In this case, the well was assumed to produce at a constant bottom-hole pressure, $p_{wf}$ (100 psi). The integrated model was run in the history matching mode for 1000 days to obtain the reservoir parameters. Then, these parameters were used to predict future performance for 9000 days. **Table 2-3** presents the history matching results and the absolute error compared to the correct values used in the simulation. The simulator and the program results are plotted in **Figs. 2-3 and 2-4** to show that a good match had been achieved. **Fig. 2-5** shows the relative permeability curve compared to that used in the simulator. The production behavior of CBM in this case started by the dewatering stage (high water flow rate 650 bbl/day), then the gas flow rate increased to its maximum value (peak gas flow rate 480 Mscf/day), and finally the gas flow rate declined to 10 Mscf/day after 27 years. The water saturation curve showed a rapid decline for water saturation during the dewatering stage and almost stabilized at $S_w = 0.35$. At this water saturation, the relative permeability to water was less than 0.01, with almost no water production.

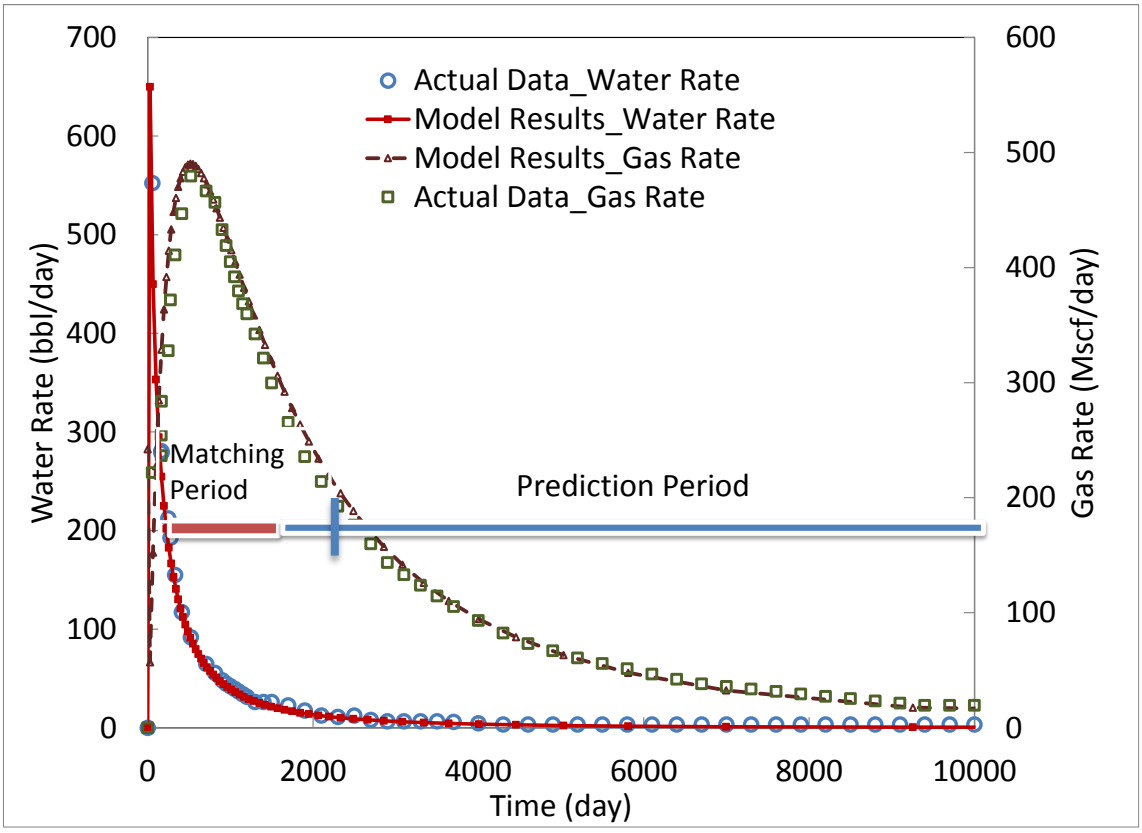


**Fig. 2-3 Gas and water production rates vs. time (history matching and prediction) hypothetical case #1.**

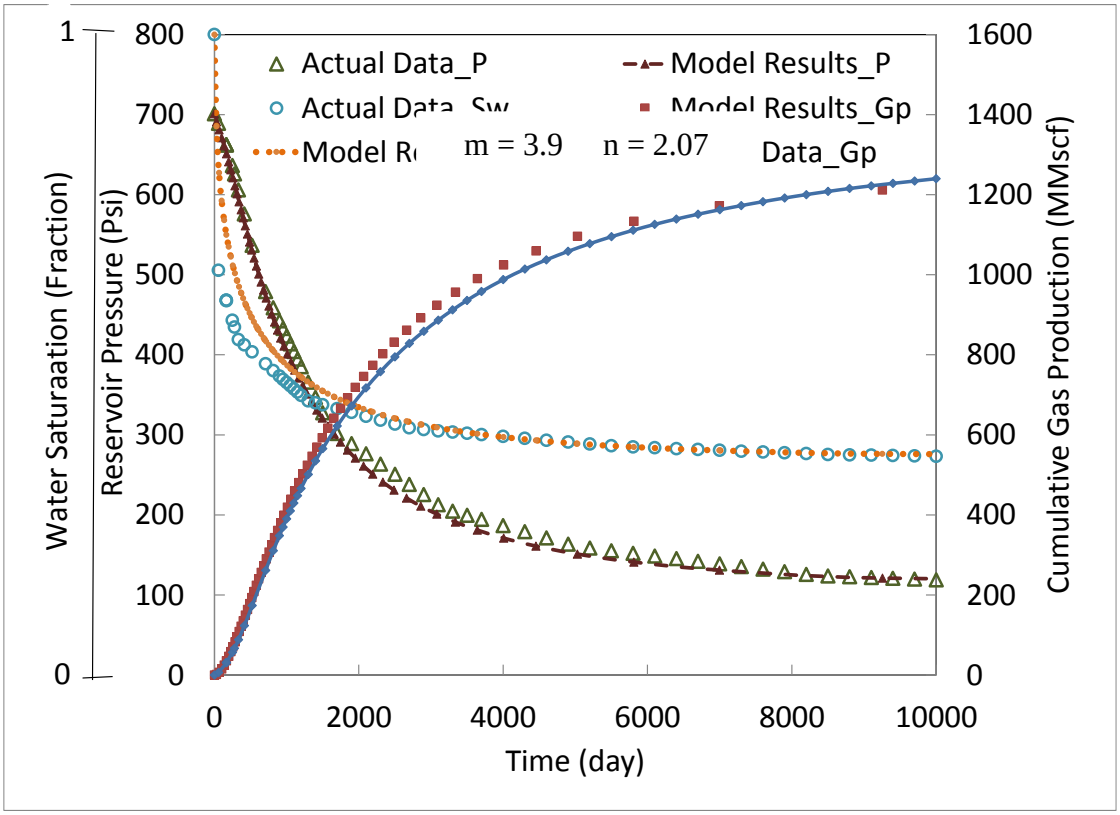


**Fig. 2-4 Reservoir pressure, water saturation and cumulative gas production vs. time for hypothetical case #1.**

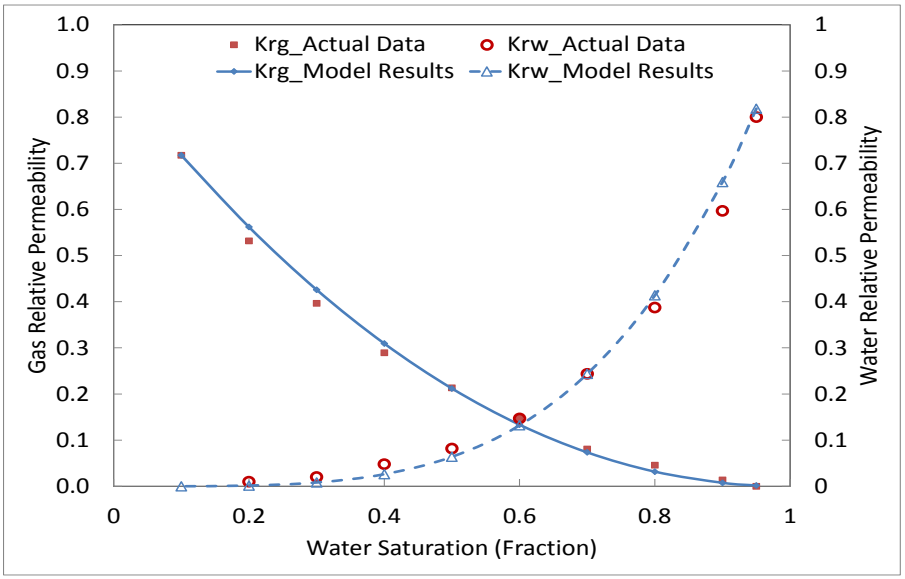


**Fig. 2-5 Gas and oil relative permeability for hypothetical case #1.**

**Hypothetical Case #2**

In this case, the well was assumed to produce at a constant water rate and allowed the bottom-hole pressure to decline to a certain limit at which the well started to produce at a constant $p_{wf}$ as shown in **Fig. 2-6**. Two different runs were conducted: one with a water rate equal to 200 bbl/day and another run for 80 bbl/day. It was used to verify the model under variable production conditions and to explain the effect of the dewatering rate on the peak gas rate. The simulator and the program results are plotted in Fig. 2-6 to show that a good match was achieved. Table 2-3 presents the history matching results and the absolute error compared to the correct values used in the simulation. This case verified the model to match and predict the behavior of a CBM well with variable production control modes (constant flow rate or constant bottom-hole flowing pressure). This case showed the effect of dewatering time on the performance behavior. As the water production rate increases, it accelerates the dewatering stage and the peak gas was reached earlier (2.5 years difference between the two runs). As a result, this model can be used to optimize the dewatering rate (initial water production rate) in order to optimize the time needed to reach the peak gas rate.

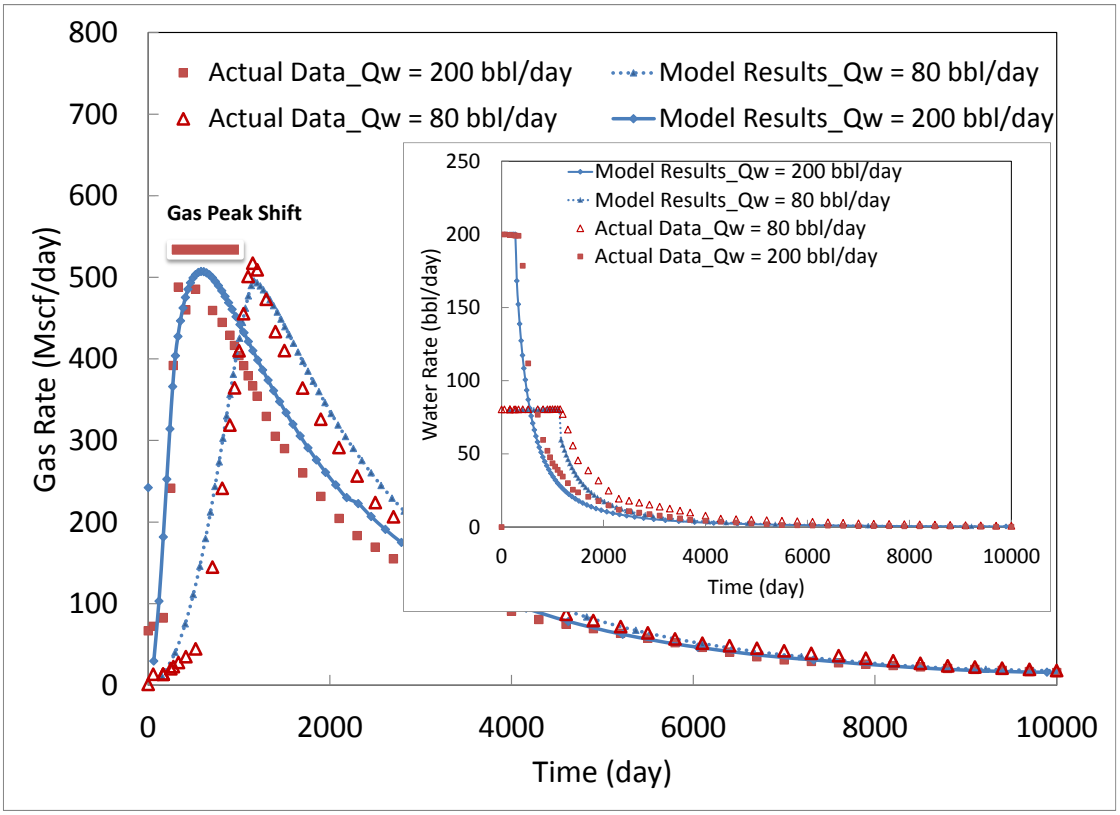


**Fig. 2-6 Gas and water production rates vs. time hypothetical case #2 for different production conditions.**

### Hypothetical Case #3

In this case, the initial gas saturation was higher than the critical saturation, and the gas production started at a high rate. Two different runs were conducted: one with water saturation that was assumed to be equal to the connate water saturation and another run with water saturation equal to 0.6. The simulator and the program results are plotted in **Fig. 2-7** to show that a good match had been achieved. Table 2-3 presents the history matching results and the absolute error compared to the correct values used in the simulation. This case verified the model at different initial water conditions. In this case, the dewatering stage was missing, and the behavior of CBM production was similar to the behavior of conventional reservoirs. In the case of water saturation equal to the connate water saturation, the gas flow rate started at a high flow rate and rapidly declined and the reservoir almost drained after approximately 6 years. In the case of water saturation equal

to 0.6, it takes a longer time (15 years) to drain the reservoir, which is a result of competitive flow between the water and the gas.

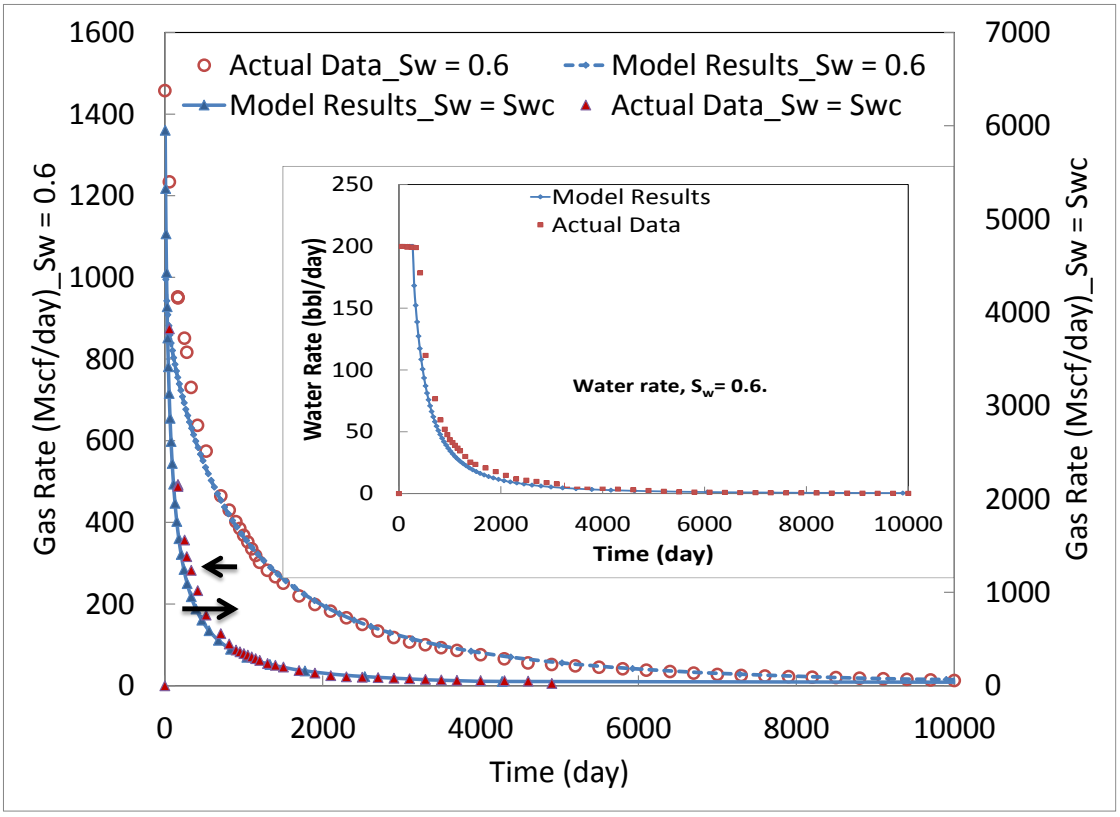


**Fig. 2-7 Gas and water production rates vs. time for hypothetical case #3 at various water saturations.**

| Parameter | Case #1 | | Case #2 | | | | Case #3 | | | |
|---|---|---|---|---|---|---|---|---|---|---|
| | Model Results | Error % | Run #1 | | Run #2 | | Run #1 | | Run #2 | |
| | | | Model Results | Error % | Model Results | Error % | Model Results | Error % | Model Results | Error % |
| Initial gas content, scf/ton | 271 | 0.7 | 279 | 3.6 | 271 | 0.7 | 271 | 0.7 | 272 | 1.1 |
| Permeability, md | 21.76 | 8.8 | 18.15 | 9.2 | 21.76 | 8.8 | 21.76 | 8.8 | 21.76 | 8.8 |
| Pore volume, acre-ft | 34.93 | 6.1 | 35.28 | 7.1 | 34.71 | 5.4 | 34.93 | 6.0 | 35.58 | 8.0 |
| $V_L$, scf/ton | 480.3 | 6.8 | 480.3 | 6.8 | 480.3 | 6.8 | 480.3 | 6.8 | 480.3 | 6.8 |
| $P_L$, psi | 538.4 | 7.6 | 538.4 | 7.6 | 538.4 | 7.6 | 538.4 | 7.6 | 538.4 | 7.6 |
| $c_s$ | 0.007 | | 0.007 | | 0.007 | | 0.002 | | 0.005 | |

Table 2-3 History matching results for hypothetical cases.

## 2.3. Field Examples

The model was used to analyze data sets for different formations: the Fruitland formation in the San Juan basin and the Upper Pottsville formation in Black Warrior basin.

**Fruitland Formation**

The original gas-in-place in the Fruitland formation was approximately 50 Tscf, and the coalbed gas reserve in Colorado and New Mexico (mainly produce from Fruitland formation) was 7.2 Tscf at the beginning of 2013 (EIA, 2013). The thickness of coal deposits varied between 50 and 70 ft in the Northern part of the basin and varied between 0 and 60 ft in the southwest part of the basin. Coalbed permeability is very sensitive to overburden and directed tectonic stress. Fruitland coalbed permeability in the producing regions of the San Juan basin is generally 5 – 60 md, and it is greatest in the fairway area (Ayers Jr 2003). The gas content of Fruitland coals is generally 150 scf/ton less in the southern two-thirds of the San Juan basin. In the northern, thermally mature (vitrinite reflectance > 0.78%), over-pressured area, ash-free gas content is generally greater than

300 scf/t, and in the fairway area, it commonly exceeds 500 scf/t. The Fruitland formation is abnormally pressured relative to a freshwater hydrostatic gradient (0.433 psi/ft). Most wells in the Fruitland formation are completed with cased holes and fracture stimulation (Ayers Jr 2003).

Two wells were analyzed using the developed model. The production data was used as an input for the model for the history-matching mode to estimate permeability, relative permeability exponents, porosity, and the initial gas content. These parameters are then used to predict the future performance of the well.

The first well is located in Archuleta County. It began production in 1999 with a total depth of 2,340 ft. As there is no completion data about this well, it was assumed that it was completed as one layer, and a weighted average value for the formation parameters was estimated. First, the model was used to match the production data and estimated the formation properties. **Fig. 2-8** presents the production history matching data and prediction data. **Table 2-4** presents the history matching results. The estimated parameters are within the range for Fruitland formations (Ayers, 2003). These parameters were then used to predict the future performance of the well for an additional 40-year. The lack of matching in case of water flow was due to the missing water production data. Fig. 2-8 presents the permeability variation with pressure depletion. The initial permeability was 12.5 md, it decreased with pressure depletion due to formation compaction, and finally it increased to 14.5 md due to matrix shrinkage effect.

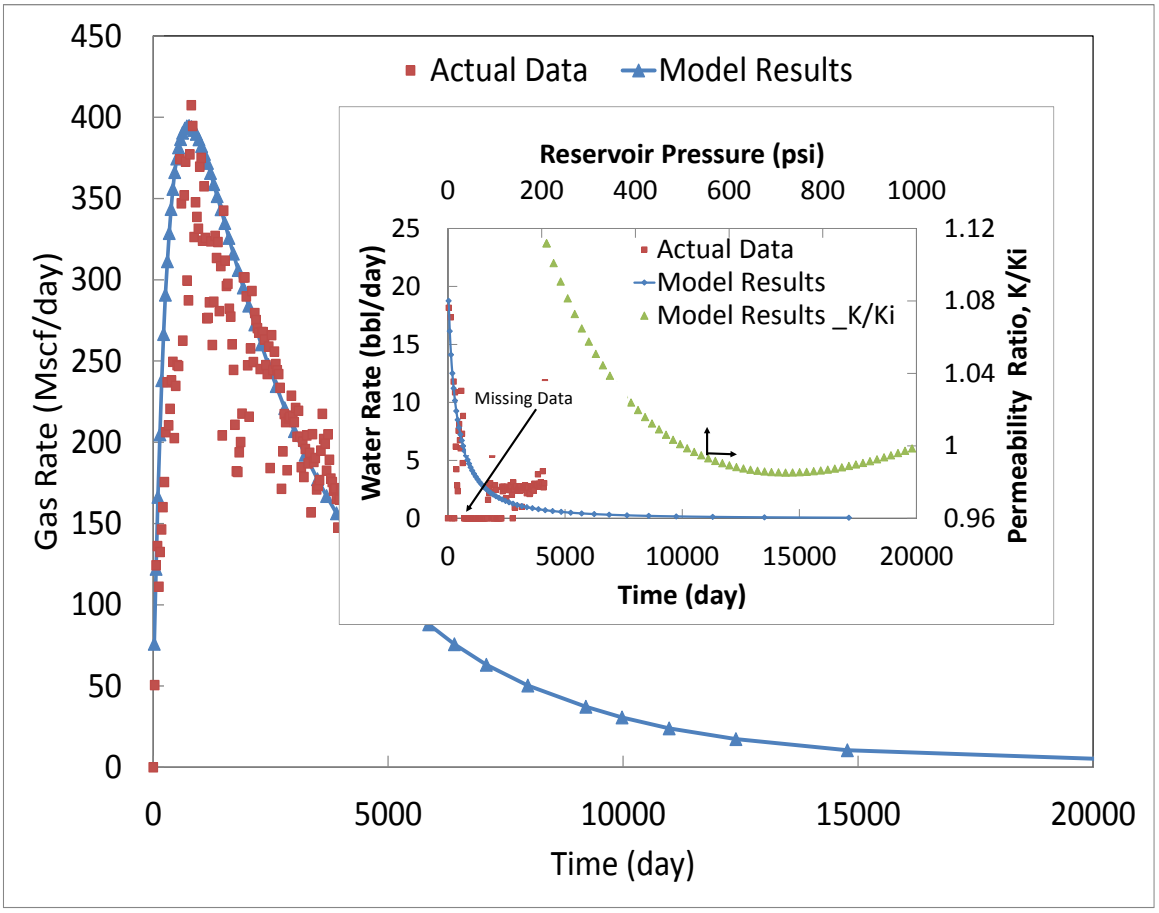


**Fig. 2-8 Gas and water production rates vs. time (history matching and prediction), and permeability vs. pressure for the Fruitland formation (well #1).**

The second well is located in La Plata County, and it is currently at production conditions. Its production started in 1992. It is completed in more than nine coal formations, but it can be combined mainly in two groups. Core data shows that the first group (Inter) contains carbonaceous shale with coal thickness of 49 ft and a middle depth of 1,760 ft; however, it shows that the second group (Basal) contains carbonaceous shale and siltstone with a coal thickness of 27 ft and a middle depth of 1,928 ft**.** The tubing head pressure varied between 72 to 65 psi.

The model was used to match the total production data from this commingled system by estimating the individual behavior for each group. The formation parameters for each

group were also estimated. The tubing head pressure was used at 70 psi and the bottom-hole pressure was calculated using the produced gas and water rates, neglecting the pressure drop on the well bore between the two groups**.** Also, skin factor was used to consider the hydraulic fracturing for the well. Table 2-4 presents the history matching results and the formation properties ranges according to Ayers (2003). The estimated parameters are within the range for Fruitland formations (Ayers, 2003). **Figs. 2-9 and 2-10** present the production history matching data and prediction data. **Fig. 2-9** shows that the gas production rate from the first coal group is higher than the production from the second group**.** This behavior is because the gas content and permeability for group 1 is higher than that for group 2. Also, as the group 1 has higher pore volume with higher permeability, it produced a higher water flow rate than group 2. **Fig. 2-10** presents the permeability variation with pressure depletion, and it shows high permeability changes due to matrix shrinkage. The permeability increased by 60%. Fig. 9 shows the matrix shrinkage effect on the gas production behavior.

A high matrix shrinkage coefficient was estimated in the second well. This could be due to the high initial gas content and the high cumulative gas production.

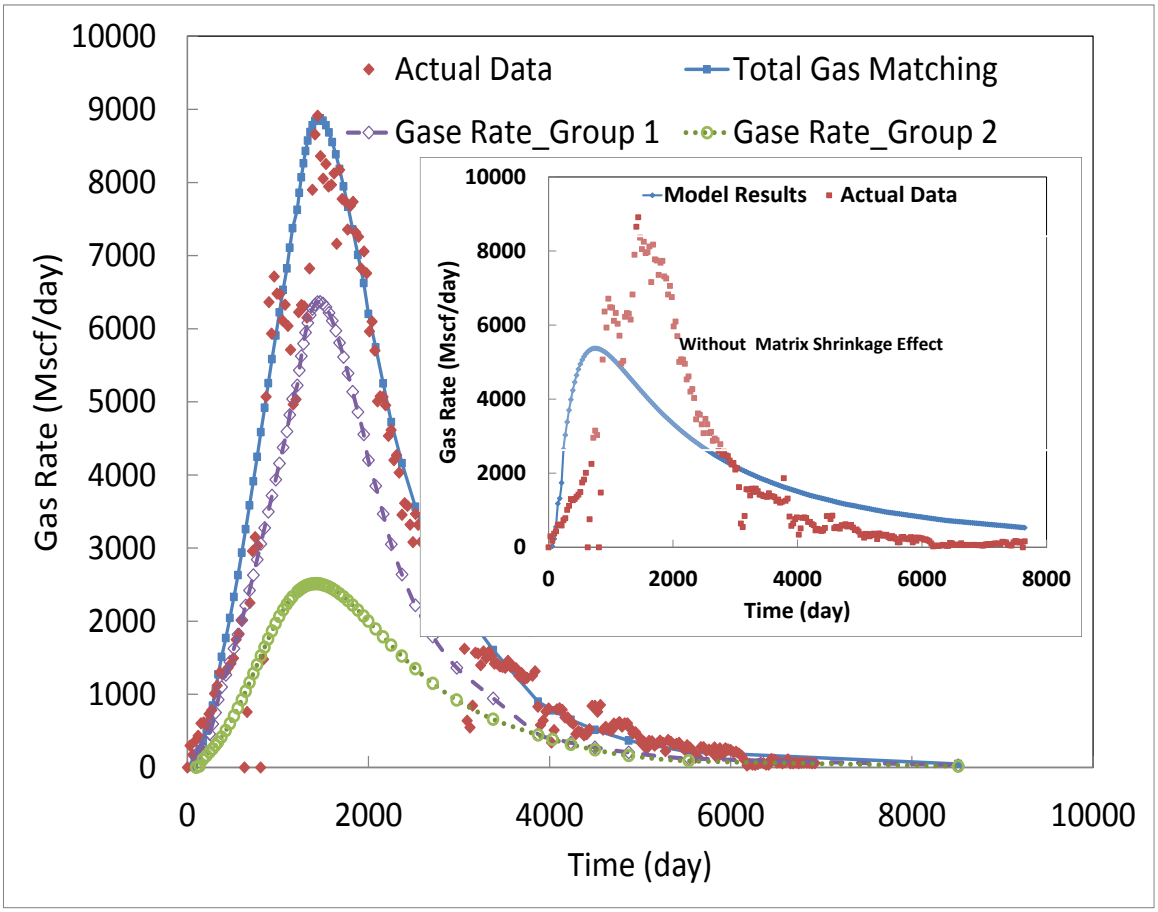


**Fig. 2-9 Gas production rate vs. time (history matching and prediction) Fruitland formation, well #2.**

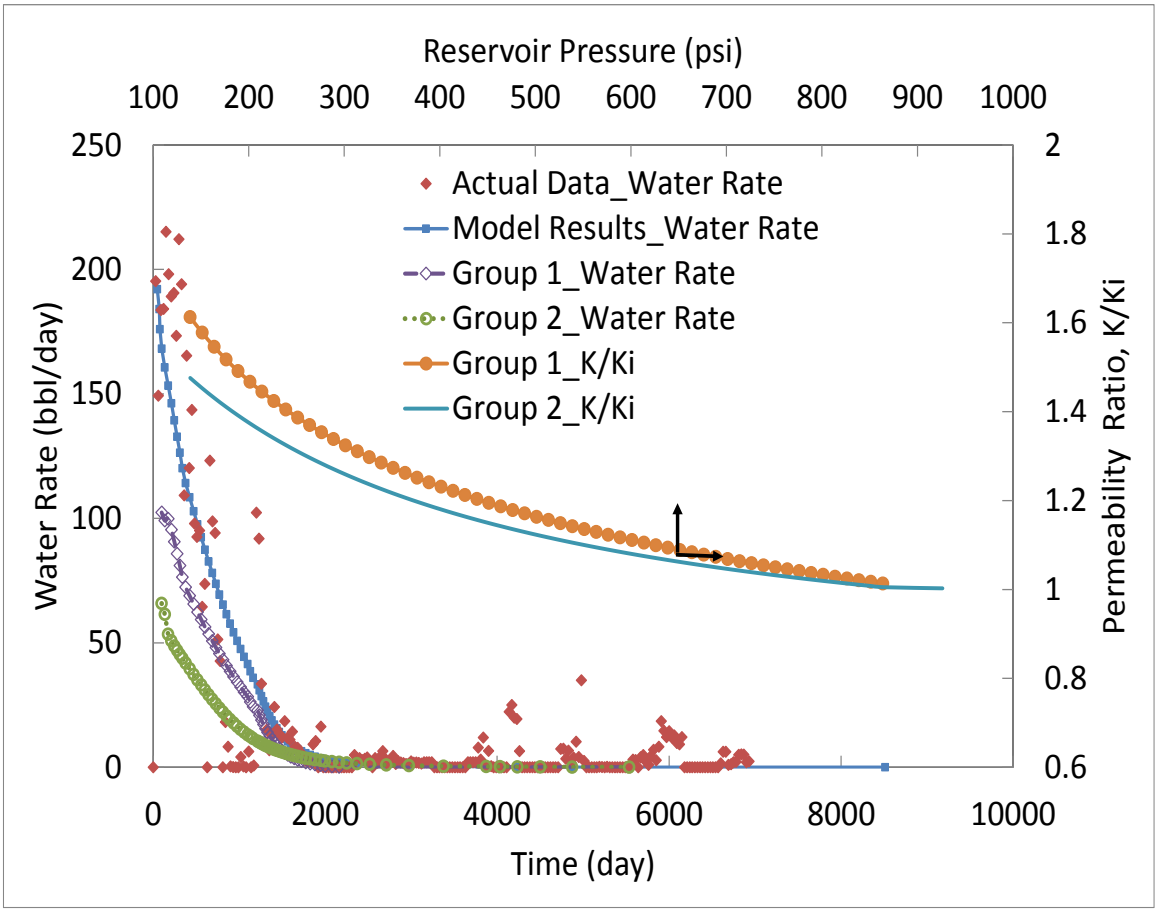


**Fig. 2-10 Water production rate vs. time (history matching and prediction) and permeability ratio vs. reservoir pressure Fruitland formation, Well #2.**

| Parameter | Model data | | | | Formation properties ranges according to Ayers (2003) | |
|---|---|---|---|---|---|---|
| | Well #1 | Well #2 | | | | |
| | | One layer model | Multilayer model | | | |
| | | | Group #1 | Group #2 | Overall area | Fairway area |
| Initial gas content, scf/ton | 320.92[a] | 500 [a] | 538 [a] | 476 [a] | 150 - | > 500 |
| Permeability, md | 12.5 | 32 | 35 | 25 | 5- 60 | > 60 |
| Drainage area, acres | 125 | 240 | 255 | 200 | 120 - | - |
| Thickness, ft | 32[b] | 76[b] | 49[b] | 27[b] | 0 - 60 | 50 -70 |
| Skin | -2 | -3.2 | -3.5 | -3 | - | - |
| $V_L$, scf/ton | 553.31 | 809 | 905 | 759 | 615- | - |
| $P_L$, psi | 316.28 | 560 | 613 | 532 | 231-641[c] | - |
| $c_s$ | 0.0118 | 0.024 | 0.026 | 0.022 | - | - |
| Porosity, volume fraction | 0.014 | 0.057 | 0.051 | 0.067 | - | - |

a. Calculated as a function of initial pressure and Langmuir constants ($V_L$, and $P_L$)

b. Input for the model

c. According to Mavor et al. (1990)

Table 2-4 History matching results for Fruitland formation cases.

**The Upper Pottsville Formation**

The Upper Pottsville Coal Total Petroleum System (TPS) in the Black Warrior basin of Alabama and Mississippi produces natural gas from coals in the Lower to Middle Pennsylvanian Upper Pottsville formation. Natural gasses produced from coals in the Black Warrior basin are very dry. Production began in both the Oak Grove and Brookwood coal degasification fields in 1981 (Hatch 2007). The ability of coal to adsorb gas is highly variable in the Black Warrior coalbed methane fields, and much of this variability may be related to differences of coal quality (Carroll and Pashin 2003).

Karacan (2013) analyzed gas and water production data from 92 vertical wells in the Brookwood and Oak Grove fields of the Black Worrior basin by history-matching techniques. Completion data for these wells shows completion at Mary Lee group, or at a combination of Pratt, Mary Lee, and Black Creek groups. The tubing head pressure for

most of the well was 8-12 psi, and the average hydrostatic gradient varies between 0 and 0.3 psi/ft (Pashin 2007). Most of the wells are hydraulically fractured.

The analyzed well is located in Tuscaloosa County, and it is currently at production conditions with a total depth of 2,947 ft. It started production in 1993. The well is completed at Pratt, Mary Lee, and Black Creek groups. The tubing head pressure was taken 10 psi (Karacan, 2013). The actual gas and water production rates were used to estimate the bottom-hole pressures for each group, neglecting the friction losses in the wellbore between the layers. Since wells in the Upper Pottsville formation are hydraulically fractured, skin factor was used to consider the well stimulation.

The model was used to match the total production data from this commingled system by estimating the individual behavior for each group. **Table 2-5** presents the history matching results and the formation properties ranges according to Karacan (2013). The estimated parameters are within the range for Upper Pottsville formation. The estimated initial gas content for these layers is slightly higher than those from Karacan (2013). These are a result of higher gas production (gas peak flowrate = 580 Mscf/day, cumulative production 1.5 Bscf) compared to the maximum flow rate according to Karacan (2013) (300 Mscf/day, cumulative production 1.1 Bscf). **Fig. 2-11** presents the production history matching data and prediction data. The production data from Mary Lee is higher than the gas production from the other groups, as it has the highest gas content when compared to Pratt, and Black Creek groups. The Pratt group has the highest formation permeability, which led to higher water production initially but then rapidly declined due to its low pore volume. The gas and water production from Black Creek group is lower than the two other groups as it has the lowest gas content, permeability, and pore volume. **Fig. 2-12** presents the permeability variation with pressure depletion. The Mary Lee group has the highest matrix shrinkage, and its permeability increased by 35 % of its original value. However, Black Creek group has the lowest matrix shrinkage due to a lower gas content.

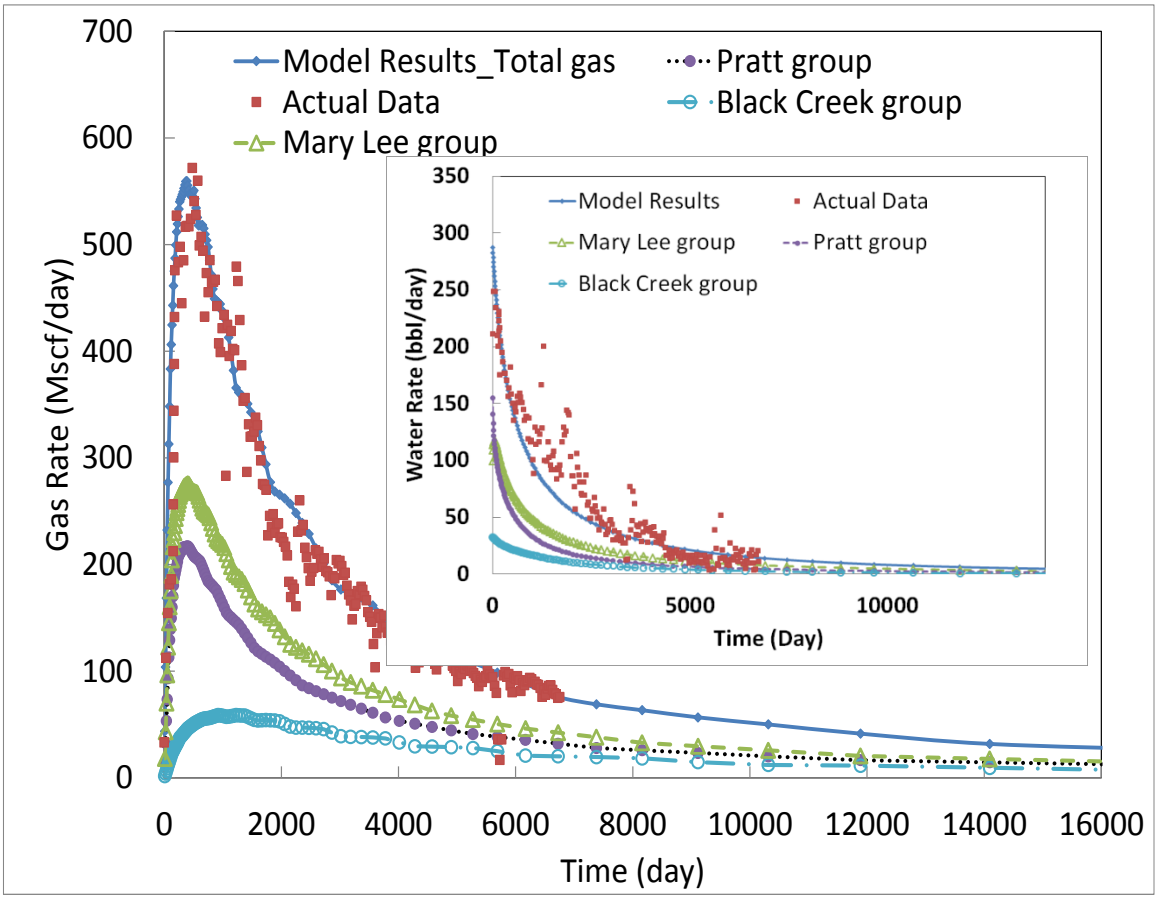


**Fig. 2-11 Gas and water production rates vs. time (history matching and prediction) Upper Pottsville formation.**

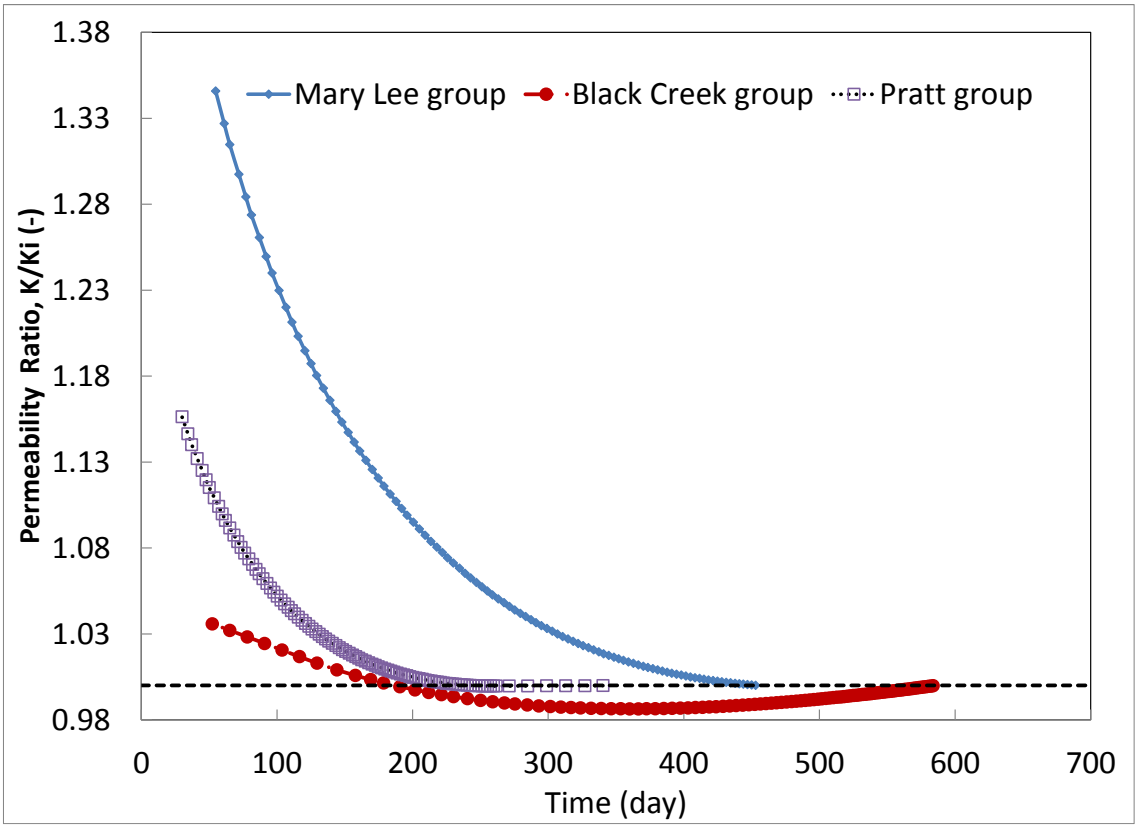


**Fig. 2-12 Permeability ratio vs. reservoir pressure of the upper Pottsville formation.**

| Parameter | Model data | | | | Formation properties Karacan (2013) | | |
|---|---|---|---|---|---|---|---|
| | One layer model | Multilayer model | | | | | |
| | | Pratt group | Mary Lee group | Black Creek group | Pratt group | Mary Lee group | Black Creek group |
| Initial gas content, | 411[a] | 302[a] | 450[a] | 299[a] | 72-251 | 65- | 39- |
| Permeability, md | 4.9 | 9 | 4.05 | 3 | 3.83- | 0.53- | 0.32- |
| Drainage area, acres | 66 | 65 | 60 | 92 | 24-117 | 6-173 | 12- |
| Thickness, ft | 54[b] | 16[b] | 28[b] | 10[b] | - | 22 | - |
| Skin | -3.1 | -3.2 | -4 | -2 | (-0.7)- | (-0.1)- | (-1.1)- |
| $V_L$, scf/ton | 611 | 700 | 750 | 587 | 676 | 666 | 567 |
| $P_L$, psi | 388 | 354 | 305 | 635 | 415 | 248 | 644 |
| $c_s$ | 0.003 | 0.002 | 0.005 | 0.002 | - | - | - |
| Porosity, volume | 0.014 | 0.013 | 0.011 | 0.018 | 0.0052 | 0.0027 | 0.005- |

a. Calculated as a function of the initial pressure and Langmuir constants ($V_L$, and $P_L$)

b. Input for the model

Table 2-5 History matching results for actual field cases.

## 2.4. Effect of Matrix Shrinkage and the Methane Solubility in the Performance

In this section, the developed material balance equation was compared to the conventional material balance equation: King's material balance equation, and Clarkson and McGovern's material balance equations. Also, this section shows the effect of considering matrix shrinkage and the methane solubility effect. For this analysis, a straight line concept was used to analyze production data (**Fig. 2-13 from A to E)**. Appendix B summarizes the developed MBE in a straight line format.

Fig. 2-13A shows the analysis using the conventional material balance equation. The original gas in-place (OGIP) is equal to the straight line slope of the underground withdrawal term (F) versus the cumulative gas production. Clarkson and McGovern's MBE was used to analyze the production data (Fig. 2-13B). The cumulative gas

production ($G_p$) was plotted on the X axis, and $\frac{\mathbf{P}}{\mathbf{P}+\mathbf{P_L}}+\frac{\emptyset(1-\overline{s_w})}{\mathbf{V_L}\boldsymbol{\rho_b}B_g}$ on the Y axis. The OGIP is equal to the X axis intercept. Fig. 12-13C shows a similar analysis using King's MBE, where $G_p$ was plotted on the X axis and $\frac{P}{z^*}$ on the Y axis. The OGIP is equal to the X axis intercept. Figs. 2-13D and E show the analysis using the MBE presented in the present paper.

**Table 2-6** summarizes the analysis results. The conventional MBE shows a low estimate of OGIP because it does not account for the adsorbed gas and it underestimates OGIP nearly 26%. Also, the King and Clarkson and McGovern MBEs underestimate OGIP around 10%, as they don't account for the matrix shrinkage and methane in water solubility effect. The developed MBE without the shrinkage effect estimated an OGIP is similar to King's and Clarkson's equations, while the neglection of the methane solubility in water almost not affecting the OGIP. This error was considered by adding the shrinkage effect in the developed material balance equation, and the developed GMBE provides a good estimate of OGIP.

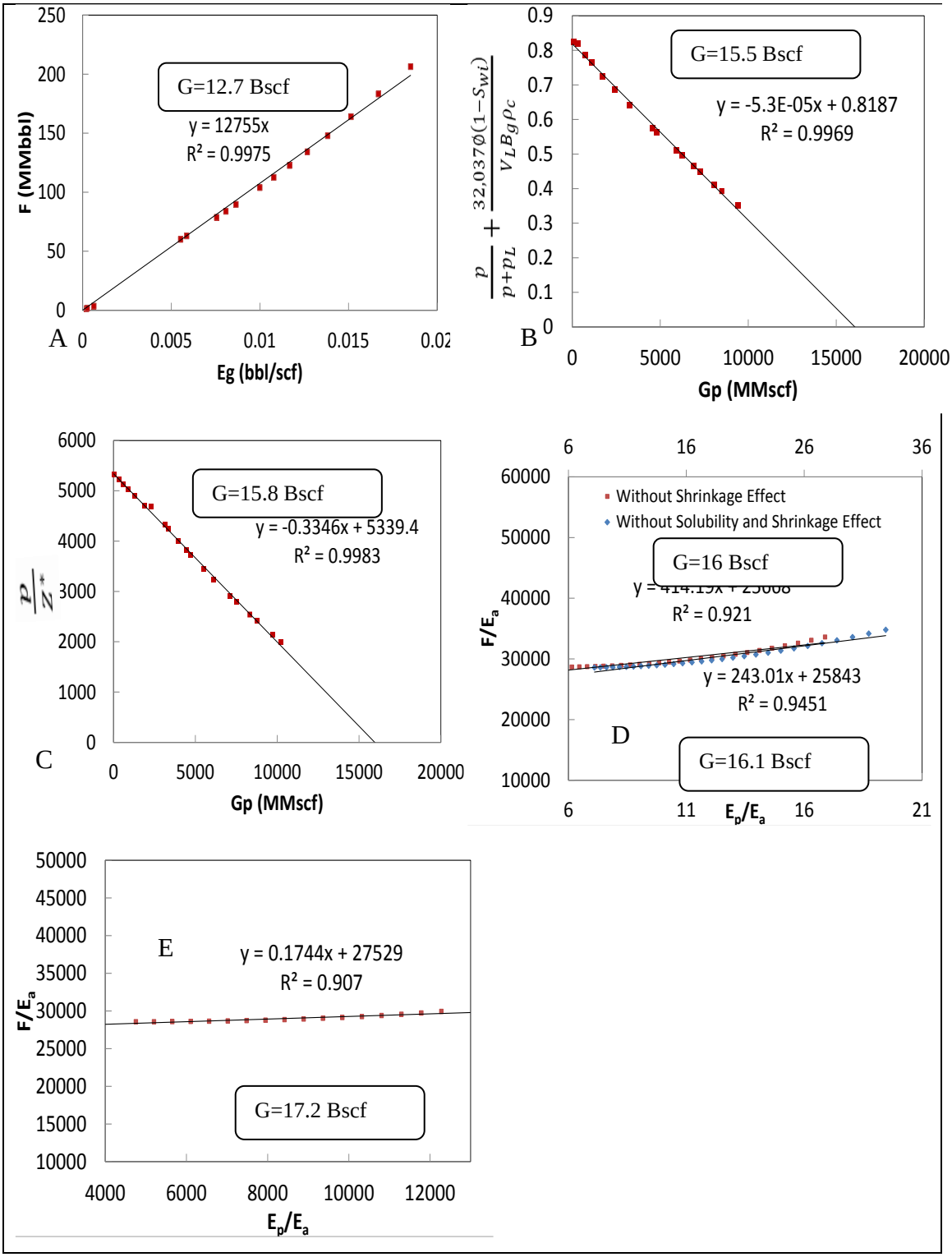


**Fig. 2-13 Comparison between MBE models; A) Conventional MBE, B) Clarkson and McGovern MBE, C) King's MBE, D) MBE without shrinkage and solubility effect, and E) Fully developed MBE. Graphs D and E were obtained from the present work.**

| | **OGIP (Bscf)** |
|---|---|
| Actual | 17.4 |
| Conventional MBE | 12.7 |
| King's MBE (King, 1993) | 15.5 |
| Clarkson et al. MBE (Clarkson and McGovern, 2001) | 15.8 |
| MBE without shrinkage effect[a] | 16.1 |
| MBE without solubility and shrinkage effect[a] | 16 |
| MBE[a] | 17.2 |

a. Present work

Table 2-6 Comparison between the different material balance equations.

# CHAPTER III
# HISTORY MATCHING AND PREDICTING GAS PRODUCTION DURING ECBM[2]

Several Authors (Wu et al. 2011; He et al. 2013; Zhou et al.2013) discussed a preliminary numerical simulation for ECBM for pilot field tests. These studies were based on predicting the capacity of coal for $CO_2$ storage but it didn't consider the estimation of formation parameters by history matching. This paper presents a model that can be used as a prediction and a history matching tool for ECBM performance in a five-spot pattern. It can be used to match the production and the injection data to estimate the initial gas content, formation permeability, porosity, and the matrix shrinkage and swelling coefficients. These parameters can then be used to predict future performance.

## 3.1. Model Description

The objective of the model is to history match and predict the performance in the ECBM process in a five-spot pattern. This is achieved by first developing a forward model for rate-time performance prediction on a one dimension problem. Then, a stream tube concept was used to convert the five-spot pattern into 1D problems. Second, the model is inverted in order to use the rate time history to obtain the reservoir properties (Ibrahim and Nasr-El-Din, 2015).

### Compositional Material Balance

A compositional material balance was developed in order to predict the gas composition distribution in the reservoir and the produced gas composition with time (Seidle 2011). It was assumed that at the initial condition the formation is saturated with methane, and the formation is homogenous and isotropic. Also, it was assumed steady

[2] Reprinted with permission from "Carbon Dioxide Sequestration in Coal Formations" by Ibrahim, A. F., Nasr-El-Din, H. A. 2015. IPTC-18278-MS. Preprint, Copyright 2015 by Society of Petroleum Engineers

state flow conditions during the injection. Water flow was neglected (dry coal with water saturation = 0) in order to simplify the calculations.

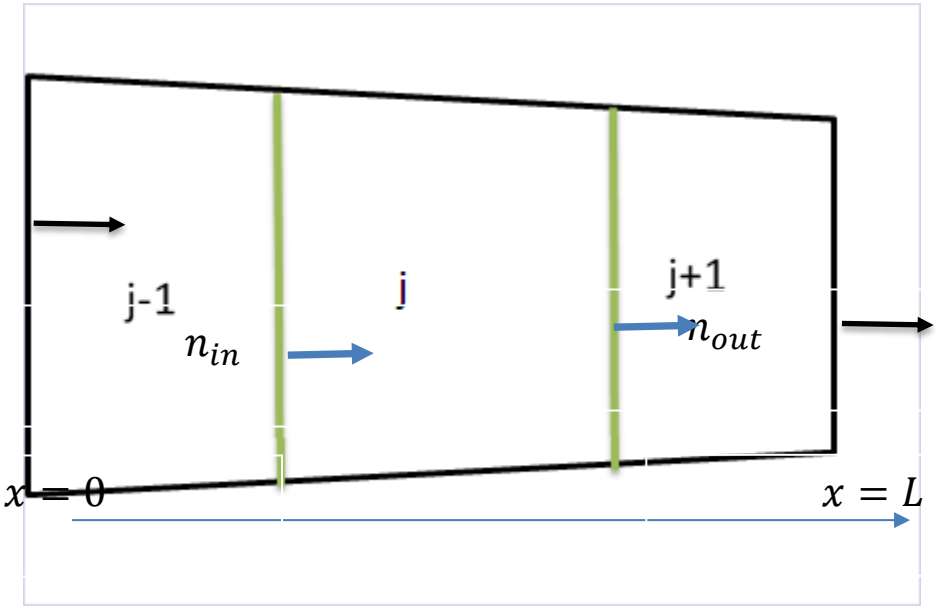


**Fig. 3-1 Schematic for the mass balance concept for the compositional material balance.**

The compositional material balance equation was based on the mass balance for each cell (**Fig. 3-1**), where j is the cell counter in the injection direction. The change in the number of $CO_2$ moles in a cell (j) is equal to the difference between the numbers of mole flow in and out of the cell.

$$\mathbf{n_{in} - n_{out} = \Delta n} \qquad 3\text{-}1$$

The number of $CO_2$ moles flows in a cell (j) is a function of the gas flowrate, the $CO_2$ mole fraction, and the pressure on the previous cell (j-1). However, the number of $CO_2$ moles flow out of a cell (j) is function of gas flowrate, the $CO_2$ mole fraction, and the pressure in the cell (j)

$$\mathbf{n_{in}} = \left[\mathbf{y_{CO2}}\ \frac{\mathbf{pq_g\Delta t}}{\mathbf{ZRT}}\right]_{\mathbf{j-1}} \quad 3\text{-}2$$

$$\mathbf{n_{out}} = \left[\mathbf{y_{CO2}}\ \frac{\mathbf{pq_g\Delta t}}{\mathbf{ZRT}}\right]_{\mathbf{j}} \quad 3\text{-}3$$

Where $\mathbf{y}_{CO2}$ is the $CO_2$ mole fraction, p is cell pressure, $q_g$ is gas flowrate, $\Delta t$ is time step, T is cell temperature, and Z is the gas compressibility factor at cell conditions and it was calculated using Peng-Robinson EOS (Peng, D.-Y. and Robinson, D.B. 1976).

The change in the number of $CO_2$ moles in a cell (j) is equal to the difference between the number of moles in the adsorbed and free phases during the time (t) and the previous (t-1) time step.

Extended Langmuir equation $\left[n_{CO2} = y_{CO2}\ \frac{\frac{n_{LCO2}p}{p_{LCO2}}}{1+p\left(\frac{y_{CO2}}{p_{LCO2}}+\frac{1-y_{CO2}}{p_{LCH4}}\right)}\right]$ was used to calculate the number of moles of adsorbed gas (Kapoor et al. 1990; Choy et al. 2000).

$$\Delta \boldsymbol{n_j} = \boldsymbol{n_{j,t}} - \boldsymbol{n_{j,t-1}} \quad 3\text{-}4$$

$$\mathbf{n_{j,t-1}} = \left[\mathbf{y_{CO2}}\ \frac{\mathbf{pV_j}}{\mathbf{ZRT}} + \mathbf{y_{CO2}}\ \frac{\frac{\mathbf{n_{LCO2}p}}{\mathbf{p_{LCO2}}}}{\mathbf{1+p\left(\frac{y_{CO2}}{p_{LCO2}}+\frac{1-y_{CO2}}{p_{LCH4}}\right)}}\right]_{\mathbf{j,t-1}} \quad 3\text{-}5$$

$$\boldsymbol{n_{j,t}} = \left[\boldsymbol{y_{CO2}}\ \frac{\boldsymbol{pV_j}}{\boldsymbol{ZRT}} + \boldsymbol{y_{CO2}}\ \frac{\boldsymbol{n_{L1}p/p_{L1}}}{\boldsymbol{1+p\left(\frac{y_{CO2}}{p_{LCO2}}+\frac{1-y_{CO2}}{p_{LCH4}}\right)}}\right]_{\boldsymbol{j,t}} \quad 3\text{-}6$$

The first and the second terms in Eqs. 5 and 6 are the volume of free and the adsorbed $CO_2$, respectively. The free $CO_2$ volume is a function of the cell pore volume ($\mathbf{V_j}$), the formation pressure and temperature (p,T), and the gas composition. However, the adsorbed $CO_2$ volume is function of Langmuir adsorption constants ($n_L$, $p_L$) for $CH_4$ and $CO_2$, formation pressure, and gas composition.

By substituting Eqs. 3-2 – 3-6 in Eq. 3-1, we obtain:

$$\left[\mathbf{y_{CO2}}\,\frac{\mathbf{pq_g\Delta t}}{\mathbf{ZRT}}\right]_{\mathbf{j-1,t}}+\left[\mathbf{y_{CO2}}\,\frac{\mathbf{pV_j}}{\mathbf{ZRT}}+\mathbf{y_{CO2}}\,\frac{\mathbf{n_{LCO2}p/p_{LCO2}}}{\mathbf{1+p\left(\frac{y_{CO2}}{p_{LCO2}}+\frac{1-y_{CO2}}{p_{L2}}\right)}}\right]_{\mathbf{j,t-1}}=\left[\mathbf{y_{CO2}}\,\frac{\mathbf{p}}{\mathbf{ZRT}}\left(\mathbf{q_g\Delta t+V_j}\right)+\mathbf{y_{CO2}}\,\frac{\mathbf{n_{LCO2}p/p_{LCO2}}}{\mathbf{1+p\left(\frac{y_{CO2}}{p_{LCO2}}+\frac{1-y_{CO2}}{p_{L2}}\right)}}\right]_{\mathbf{j,t}}$$

3-7

For a cell (j) and time step (t), the right-hand side of Eq. 3-7 is:

$$\mathbf{n_x}=\left[\mathbf{y_{CO2}}\,\frac{\mathbf{pq_g\Delta t}}{\mathbf{ZRT}}\right]_{\mathbf{j-1,t}}+\left[\mathbf{y_{CO2}}\,\frac{\mathbf{pV_j}}{\mathbf{ZRT}}+\mathbf{y_{CO2}}\,\frac{\frac{\mathbf{n_{LCO2}p}}{\mathbf{p_{LCO2}}}}{\mathbf{1+p\left(\frac{y_{CO2}}{p_{LCO2}}+\frac{1-y_{CO2}}{p_{LCH4}}\right)}}\right]_{\mathbf{j,t-1}}$$

By substituting in Eq. 3-7.

$$\mathbf{n_x}=\left[\mathbf{y_{CO2}}\,\frac{\mathbf{p}}{\mathbf{ZRT}}\left(\mathbf{q_g\Delta t+V_j}\right)+\mathbf{y_{CO2}}\,\frac{\frac{\mathbf{n_{LCO2}p}}{\mathbf{p_{LCO2}}}}{\mathbf{1+p\left(\frac{y_{CO2}}{p_{LCO2}}+\frac{1-y_{CO2}}{p_{LCH4}}\right)}}\right]_{\mathbf{j,t}}$$

3-8

By rearranging Eq. 3-8 in a quadratic formula, the final equation is:

$$\mathbf{A\,y_{CO2}^2+B\,y_{CO2}+C=0}$$

3-9

Where:

$$\mathbf{A}=\frac{\mathbf{p_j}}{\mathbf{Z_jRT}}\left(\mathbf{q_g\Delta t+V_j}\right)\times\mathbf{p_j}\left(\frac{\mathbf{1}}{\mathbf{p_{LCO2}}}-\frac{\mathbf{1}}{\mathbf{p_{LCH4}}}\right)$$

$$\mathbf{B}=\frac{\mathbf{p_j}}{\mathbf{Z_jRT}}\left(\mathbf{q_g\Delta t+V_j}\right)\times\left(\mathbf{1}+\frac{\mathbf{p_j}}{\mathbf{p_{LCH4}}}\right)+\frac{\mathbf{n_{L1}p_j}}{\mathbf{p_{LCO2}}}-\mathbf{n_x}\times\mathbf{p_j}\left(\frac{\mathbf{1}}{\mathbf{p_{LCO2}}}-\frac{\mathbf{1}}{\mathbf{p_{LCH4}}}\right)$$

$$\mathbf{C}=-\,\mathbf{n_x}\times\left(\mathbf{1}+\frac{\mathbf{p}}{\mathbf{p_{LCH4}}}\right)$$

Solve **Eq. 3-9** for $y_{CO2}$ where;

The initial conditions are;

At t = 0 $\quad (y_{CO2})_j = 0 \qquad p = reservoir\ pressure$

Boundary condition;

At $\quad (y_{CO2})_0 = 1 \qquad p =$ injection pressure $(p_i)$

Darcy equation for gas was used to calculate the gas flow rate and it was assumed steady state flow conditions (Ahmed 2010).

$$qg = \frac{0.111924\ A\ K\ (p_{inj}^2 - p_{wf}^2)}{T\ L\ Z\ \mu_g} \quad \textbf{3-10}$$

Where:

$qg$ is the total gas flow rate, A is the cross section area, $p_{inj}$ and $p_{wf}$ are the injection and production pressures, T is the formation temperature, L is the core length, $\mu_g$ and Z are the gas viscosity and compressibility factor.

**Stream Tube Flow**

The stream tube method was used to monitor the displacement of methane by $CO_2$ and it was used to convert the 2D problem (reservoir pattern) into a 1D problem. (Leighton and Higgins 1975) proposed the streamline-channel flow method. A pattern flood can be considered to perform as a number of parallel flow tubes whose boundaries are the stream lines.

Streamlines were developed between the injection and production wells (**Fig. 3-2)**. However, various streamlines have different lengths with the shortest streamline being the direct line between the injector and producer. The pressure gradient along this line is the highest that causes the injection fluid to flow faster along the shortest streamline than the other lines at which the breakthrough started.

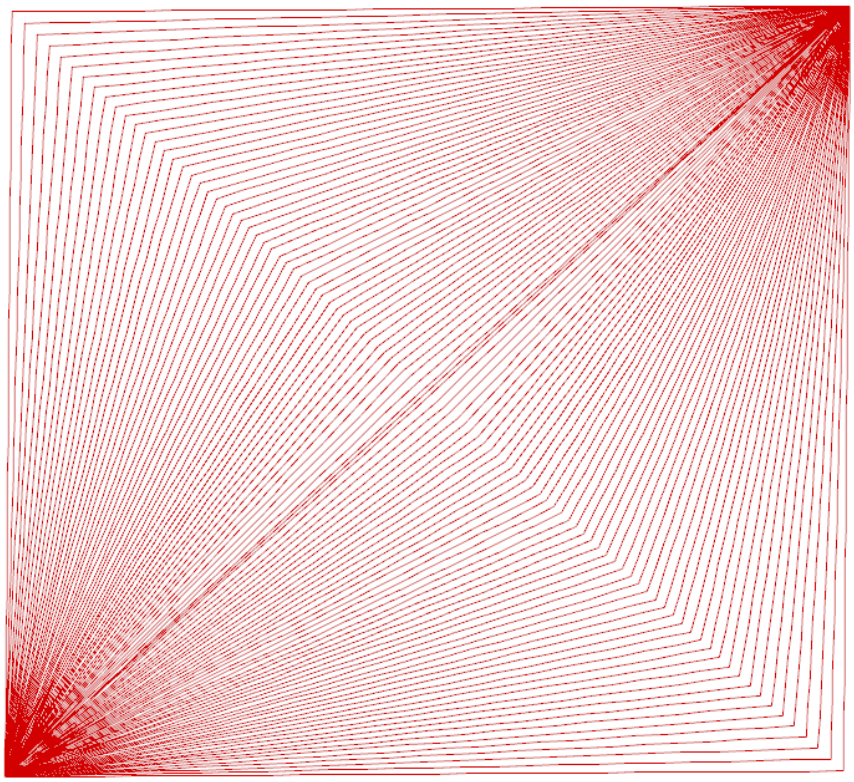

**Fig. 3-2 Streamline lines in a quadrant of a five-spot**

## Coal Swelling and Shrinkage

$CO_2$ adsorption and $CH_4$ desorption affect the coal permeability. $CH_4$ desorption shrinks the coal matrix and increases cleat width that increases the absolute permeability. Opposite effects can be expected when $CO_2$ is sorbed by coal. (Palmer 2009) considered the coal swelling and shrinkage effects as follows.

$$\frac{\emptyset}{\emptyset_i} = 1 + c_f \Delta\overline{P} + c_{sw}\Delta p_1 - c_{sh}\Delta p_2 \qquad 3\text{-}11$$

$c_f$ is the formation compressibility. $c_{sw}$ and $c_{sh}$ are the matrix swelling and shrinkage coefficients, respectively, which is a function of the formation mechanical properties and the gas properties. The history matching technique can be used to determine $c_{sw}$ and $c_{sh}$.

$$\Delta \mathbf{p_1} = \left[\frac{\mathbf{p/p_{LCO2}}}{\mathbf{1+p\left(\frac{y_{CO2}}{p_{LCO2}}+\frac{1-y_{CO2}}{p_{L2}}\right)}}\right]_{initial} - \left[\frac{\mathbf{p/p_{LCO2}}}{\mathbf{1+p\left(\frac{y_{CO2}}{p_{LCO2}}+\frac{1-y_{CO2}}{p_{LCH4}}\right)}}\right]_{current} \quad 3\text{-}12$$

$$\Delta \mathbf{p_2} = \left[\frac{\mathbf{p/p_{LCH4}}}{\mathbf{1+p\left(\frac{y_{CO2}}{p_{LCO2}}+\frac{1-y_{CO2}}{p_{LCH4}}\right)}}\right]_{initial} - \left[\frac{\mathbf{p/p_{LCH4}}}{\mathbf{1+p\left(\frac{y_{CO2}}{p_{LCO2}}+\frac{1-y_{CO2}}{p_{LCH4}}\right)}}\right]_{current} \quad 3\text{-}13$$

$$\Delta\overline{P} = P_i - P$$

The permeability variation can be predicted as a function of the porosity (McKee 1987; Palmer 1998; ZhouHou et al. 2013) as follows:

$$\frac{\mathbf{k}}{\mathbf{k_i}} = \left(\frac{\emptyset}{\emptyset_i}\right)^{\mathbf{3}} \quad 3\text{-}14$$

During the ECBM, the behavior is dominated by a steady state flow, where the average reservoir pressure remains constant. The porosity changes will mainly depend on the matrix shrinkage and swelling effect, not compressibility.

**Optimization Algorithm**

The model is combined with a genetic algorithm routine (Holland 1975) to estimate the formation properties that gives the best match with the observed production and injection history. The analysis is started by assuming an initial guess for these parameters and calculating the performance for the system. The error in the model results can then be calculated by Eq. 3-15:

$$\mathbf{Error} = \frac{\mathbf{1}}{\mathbf{2n}}\left[\sum_{\mathbf{1}}^{\mathbf{n}}\left|\frac{\mathbf{q_{g_{observed}} - q_{g_{model}}}}{\mathbf{q_{g_{observed}}}}\right| + \sum_{\mathbf{1}}^{\mathbf{n}}\left|\frac{\mathbf{q_{w_{observed}} - q_{w_{model}}}}{\mathbf{q_{w_{observed}}}}\right|\right] \quad 3\text{-}15$$

Where n is the number of the total data points used in history matching analysis.
The genetic algorithm routine was used to minimize the error from Eq. 15 by guessing the formation properties.

### 3.2. Model Verification

Coreflood data was used to verify the model as a 1D model (ZhouHussain et al. 2013) assuming that the coreflood experiment is one stream tube as a 1D flow problem. **Table 3-1** presents the basic data for the coreflood experiment. The production data (gas flow rate, gas composition) was used as an input for the model. The model was run at constant production pressure and variable injection pressure. History matching was performed for this data and the coal core parameters (Langmuir adsorption pressure and volume for $CO_2$ and $CH_4$, shrinkage and swelling coefficients, porosity, and permeability) were estimated.

**Figs. 3-3** and **3-4** show a good matching for the experimental flowrates and the concentrations with the model results. **Table 3-2** shows the history matching parameters. The production data shows that the $CO_2$ breakthrough after 0.32 day and the $CO_2$ production sharply increased for the first two days where $CO_2$ concentration on the produced gas is 0.9. **Fig. 3-5** shows the injection pressure and the average reservoir permeability. The reservoir permeability decreased with continuous $CO_2$ injection due to coal matrix swelling, where permeability reduced by 10 times the original value.

**Figs. 3-6 – 3-8** show the porosity, permeability, and $CO_2$ fraction distribution along the core with respect to time. The core was initially saturated with methane (100% $CH_4$). Once the $CO_2$ was injected, a $CO_2$ front was formed and propagated along the core with displacing the methane from the core. $CO_2$ breakthrough after around 0.32 day injection with a very low $CO_2$ concentration on the produced gas (less than 0.1). The average $CO_2$ concentration on the core to increase sharply in the first two days to 0.95 then it gradually increased to 0.997 after 5.7 days. Porosity distribution behavior along the core was similar to the $CO_2$ distribution behavior, where the average porosity in the core decreased sharply in the first two days to 0.027 ($\frac{\emptyset}{\emptyset_i} = 0.5$), then it gradually decreased to 0.026 ($\frac{\emptyset}{\emptyset_i} = 0.46$) after 5.7 days. Permeability distribution changed faster along the core, where the average permeability in the core decreased sharply in the first two days to 0.0025 ($\frac{k}{k_i} = 0.13$), then it gradually decreased to 0.0019 ($\frac{k}{k_i} = 0.1$) after 5.7 days.

| Parameter | Value |
|---|---|
| Core bulk volume, $in^3$ | 5.266 |
| Core length, in | 3.03 |
| Core diameter, in | 1.496 |
| Core cross-section area, $in^2$ | 1.736 |
| Core bulk density, $lb/ft^3$ | 91.6 |

Table 3-1 Physical properties of the coal sample used in the experiments (ZhouHussain et al. 2013).

| Parameter | Initial value | Matching value |
|---|---|---|
| Permeability, md | 0.05 | 0.019 |
| Porosity, fraction | 0.07 | 0.057 |
| Langmuir adsorption volume $CH_4$, scf/ton | 500 | 450 |
| Langmuir adsorption pressure $CH_4$, psi | 200 | 75.98 |
| Langmuir adsorption volume $CO_2$, scf/ton | 800 | 1200 |
| Langmuir adsorption pressure $CO_2$, psi | 300 | 126.53 |
| Matrix shrinkage coefficient | 0.0007 | 0.00332 |
| Matrix swelling coefficient | 0.014 | 0.03259 |

Table 3-2 History matching results (1D model case).

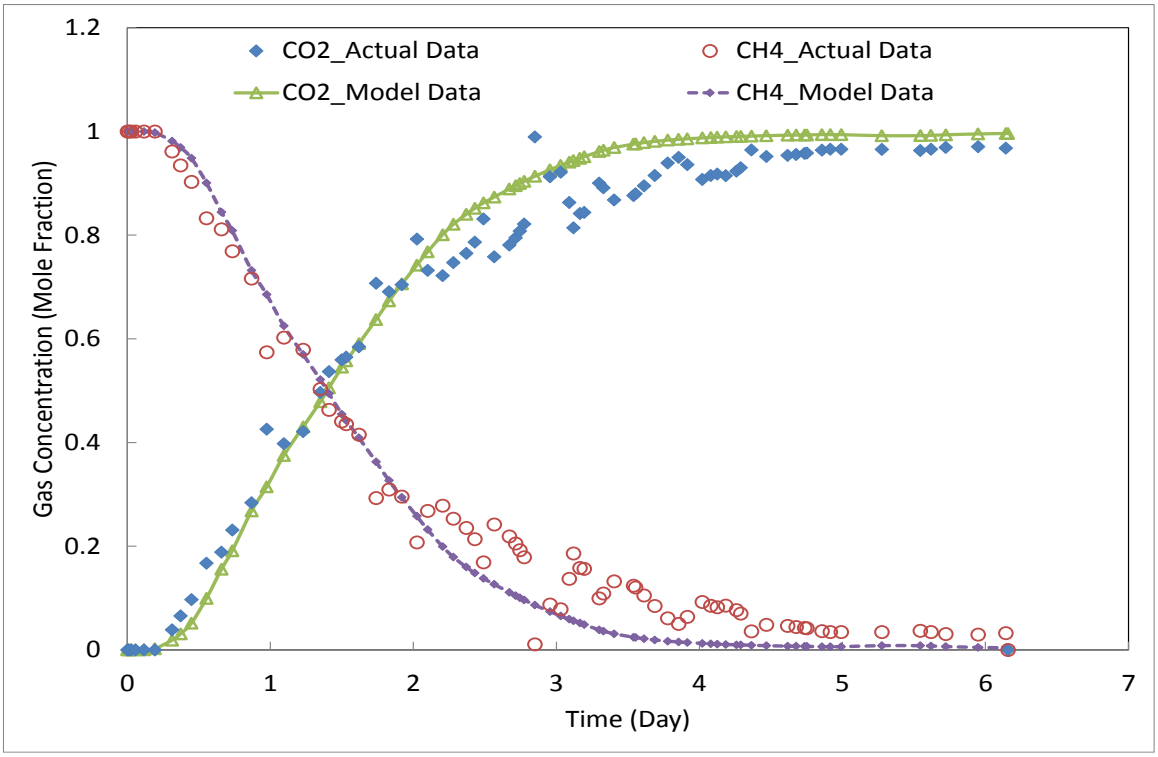


**Fig. 3-3 Gas composition history matching in case of 1D model (Zhou et al. 2013).**

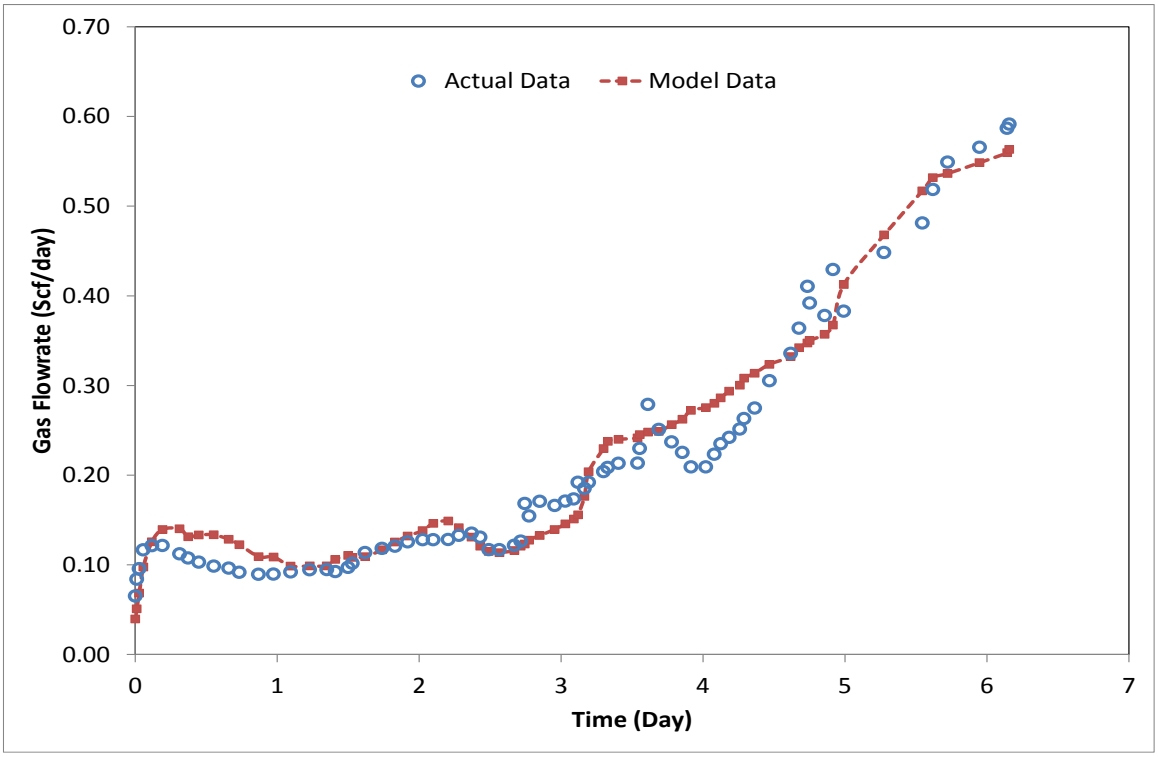


**Fig. 3-4 Total gas production flow rate history matching in case of 1D model (Zhou et al. 2013).**

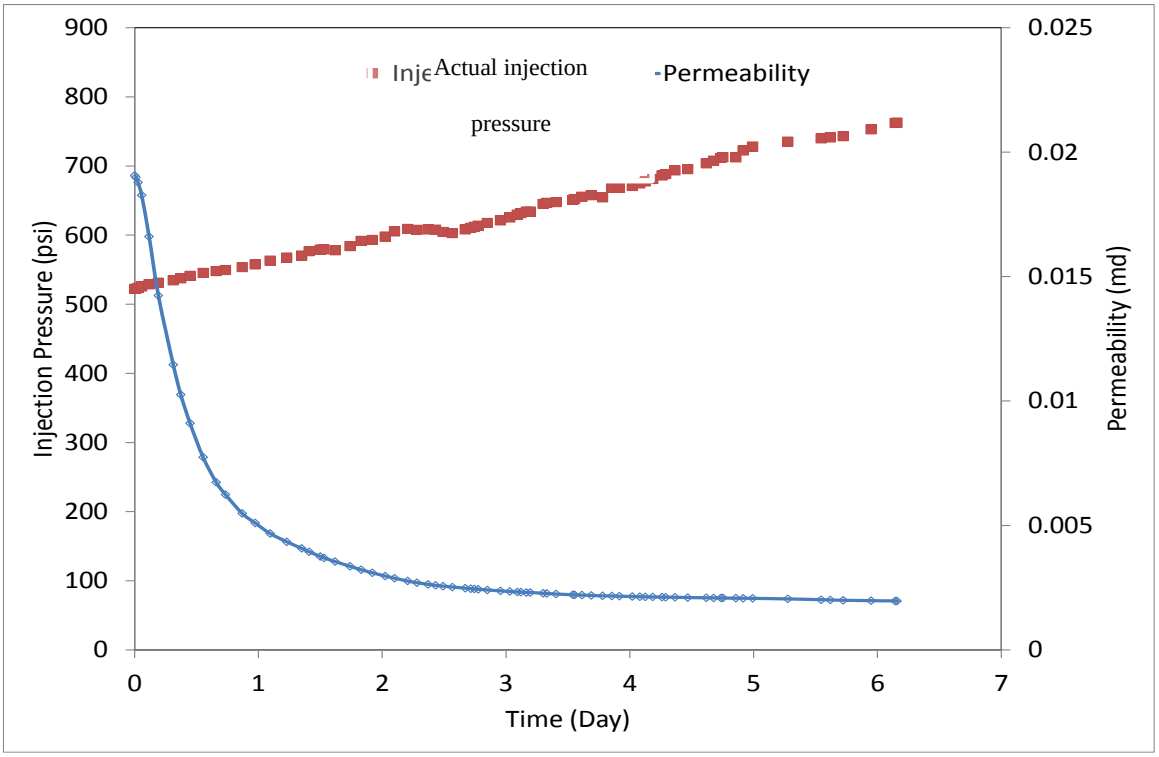


**Fig. 3-5 Actual injection pressure and observed permeability decline versus time (1D model).**

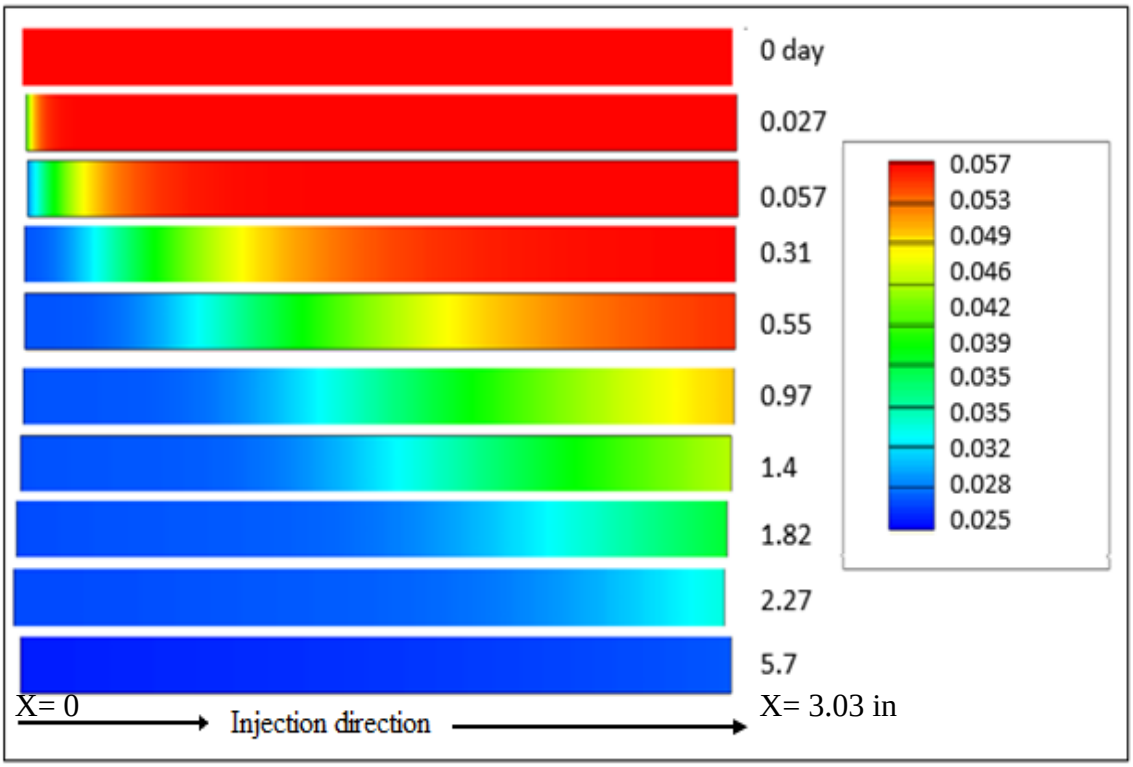


**Fig. 3-6 Porosity distribution along the core with time (1D model).**

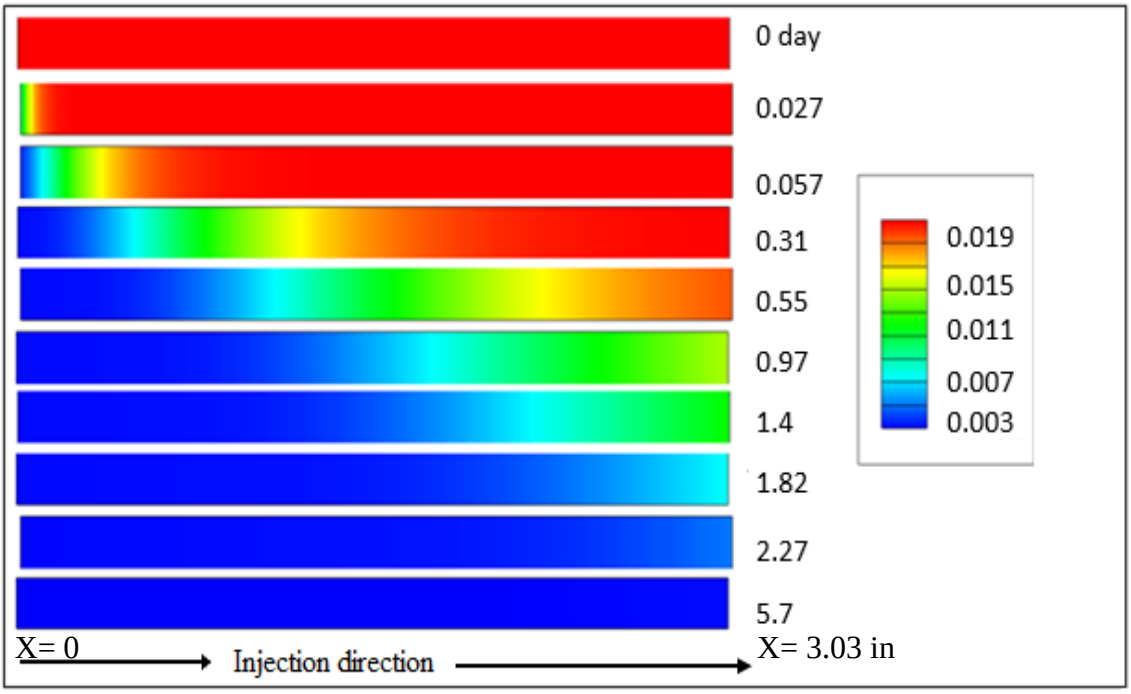


**Fig. 3-7 Permeability distribution along the core with time (1D model).**

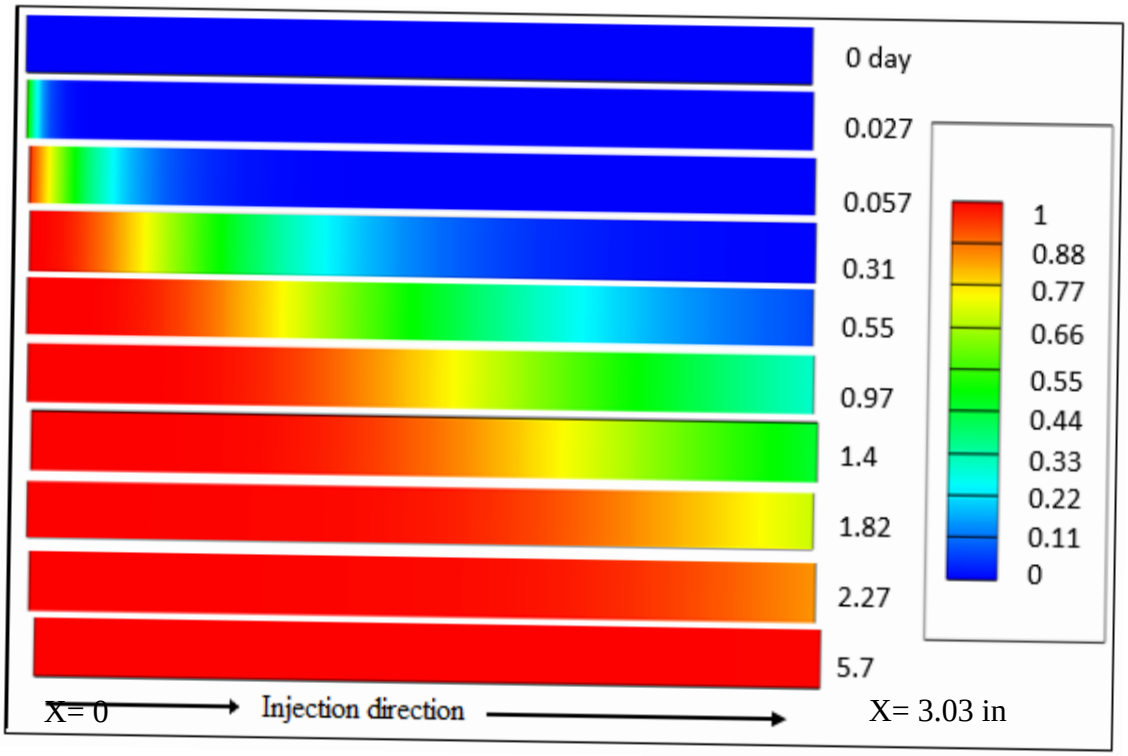


**Fig. 3-8 $CO_2$ concentration along the core with time (1D model).**

**Five-Spot Pattern Case**

Five-spot pattern case was used to examine the behavior of ECBM in 2D model. Stream tubes were used to cover a quadrant five-spot pattern. The behavior of each stream tube was treated as an individual 1D problem using 1D model. Then, the total production is the summation of all tubes production. **Table 3-3** presents the quadrant five-spot pattern properties. **Figs. 3-9** and **3-10** show the production behavior and **Fig.** 3-**11** shows the average reservoir permeability change with time. It shows that the total gas flow rate was a reflection for reservoir permeability. The total flow rate started at 1.35 MMscf then sharply decreased due to permeability reduction for the first year ($\frac{q_t}{q_{ti}} = 0.58, \frac{k}{k_i} = 0.59$) then it gradually decreased and stabilized after 3.2 years ($\frac{q_t}{q_{ti}} = 0.51, \frac{k}{k_i} = 0.55$). The methane production rate was equal to the total flow rate for the first four months then it deceased due to $CO_2$ breakthrough. After $CO_2$ breakthrough, $CO_2$ concentration on the produced gas increased sharply for 1.5 years ($y_{CO2} = 0.9$) then it gradually increased for 2 years ($y_{CO2} = 0.996$). **Fig. 3-12** shows the pressure distribution along the diagonal from the injection well toward the production well.

**Figs. 3-13 – 3-15** shows $CO_2$ fraction, porosity, and permeability distribution in the reservoir with time. $CO_2$ propagated cylindrically with the injector as a center point for the first 70 days. A cusping behavior for the $CO_2$ front was then created that led to a fingering breakthrough with a sweep efficiency of 60%. After $CO_2$ breakthrough, the average $CO_2$ concentration increased sharply to 0.97 after 1.5 years injection. Porosity distribution behavior was almost similar to the $CO_2$ distribution behavior. The average porosity on the reservoir decreased sharply in the first 1.5 years to 0.0346 ($\frac{\emptyset}{\emptyset_i} = 0.818$), then it gradually decreased to 0.0345 ($\frac{\emptyset}{\emptyset_i} = 0.816$) after 3.2 years. The permeability distribution behavior changed faster in the reservoir, where the average permeability on the reservoir decreased sharply in the first 1.5 years to 5.57 md ($\frac{k}{k_i} = 0.0.557$), then it gradually decreased to 5.52 md ($\frac{k}{k_i} = 0.552$) after 3.2 years. At the end of injection, it was

observed that the permeability around the injection well was lower than its values around the production well due to the different pressure distribution along the reservoir.

| Parameter | Value |
|---|---|
| Pattern bulk volume, acr.ft | 300 |
| Formation permeability, md | 10.13 |
| Formation porosity, fraction | 0.0423 |
| Langmuir adsorption volume $CH_4$, scf/ton | 820 |
| Langmuir adsorption pressure $CH_4$, psi | 500 |
| Langmuir adsorption volume $CO_2$, scf/ton | 1528 |
| Langmuir adsorption pressure $CO_2$, psi | 700 |
| Matrix shrinkage coefficient | 0.0003 |
| Matrix swelling coefficient | 0.009 |
| Injection pressure, psi | 1160 |
| Production pressure, psi | 200 |

Table 3-3 Quadrant five-spot pattern properties used in the 2D model (Wu et al. 2011).

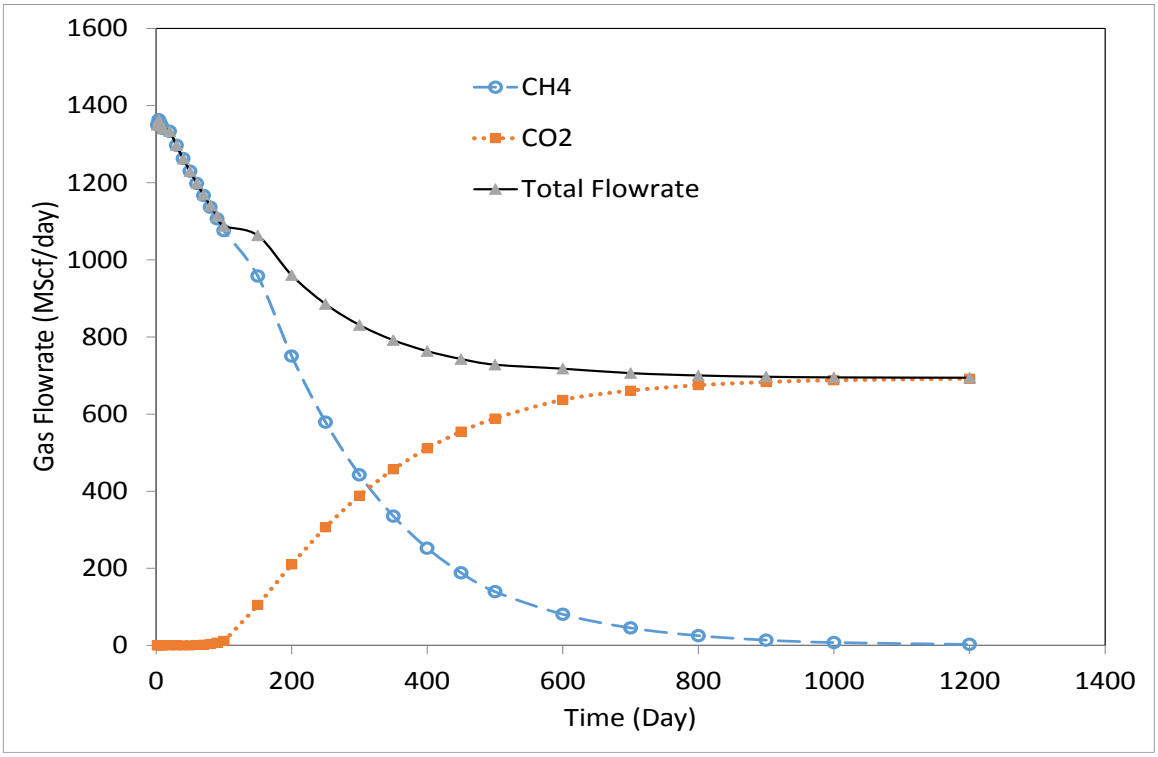


**Fig. 3-9 Gas production data versus time (2D model).**

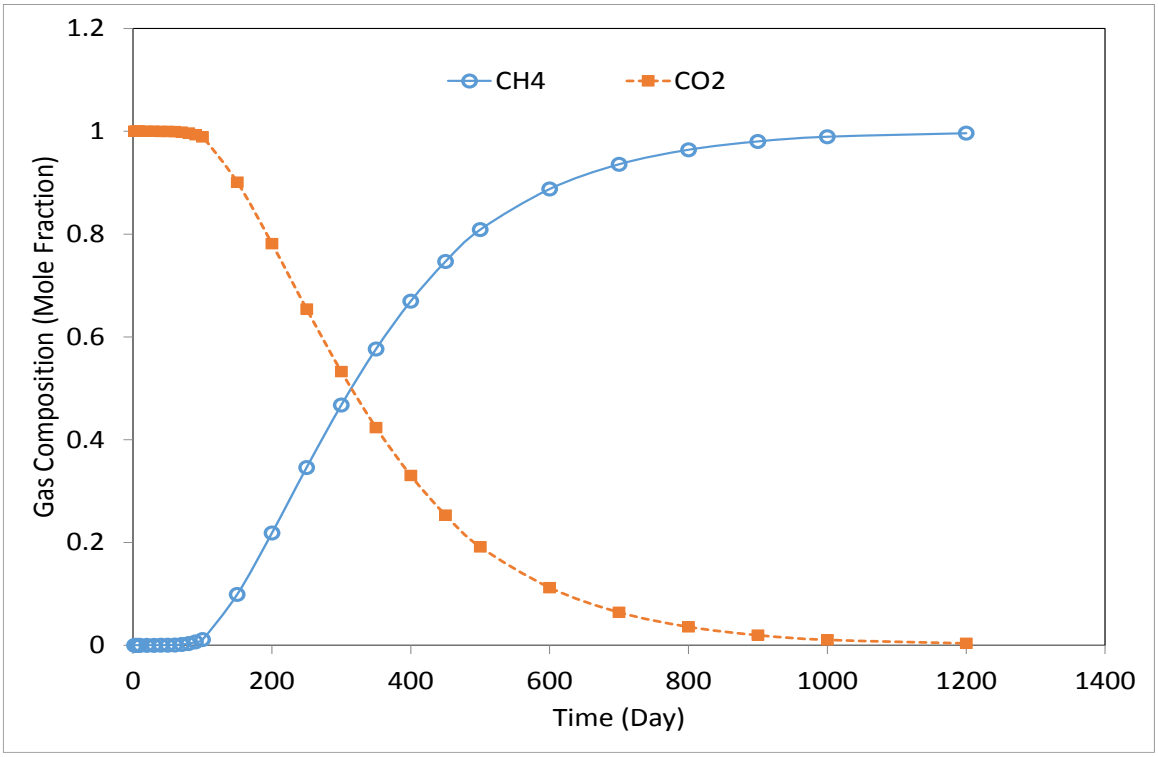


**Fig. 3-10 Produced gas composition versus time (2D model).**

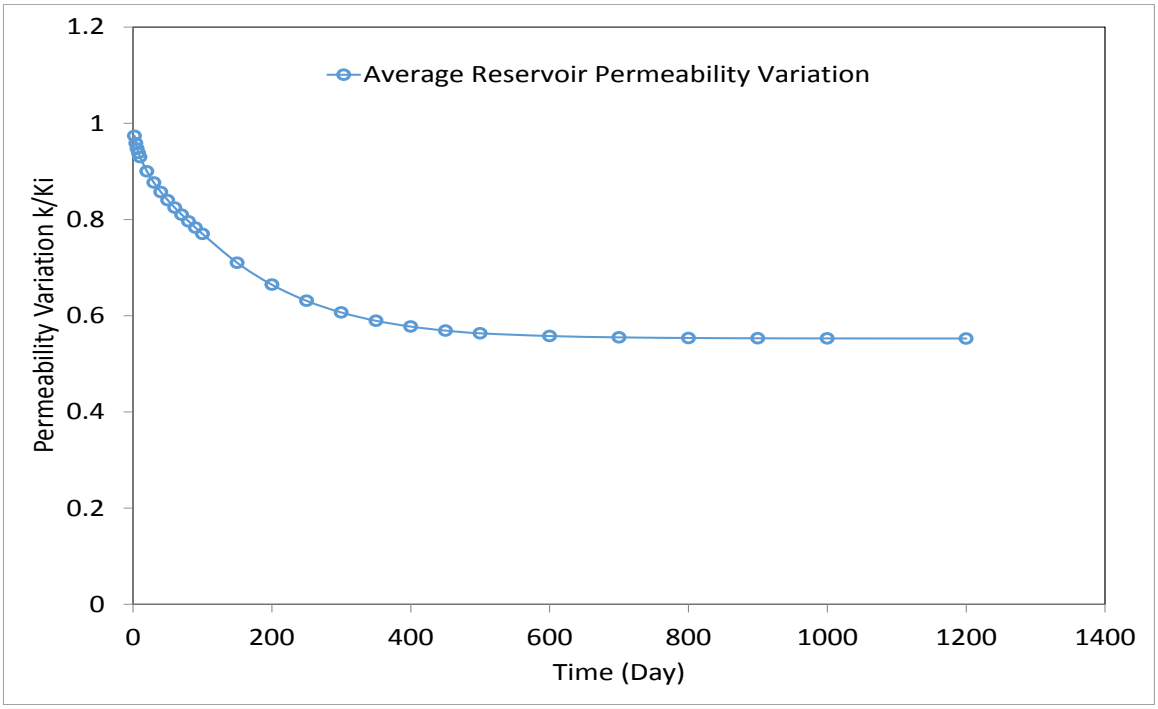


**Fig. 3-11 Reservoir permeability variation versus time (2D model).**

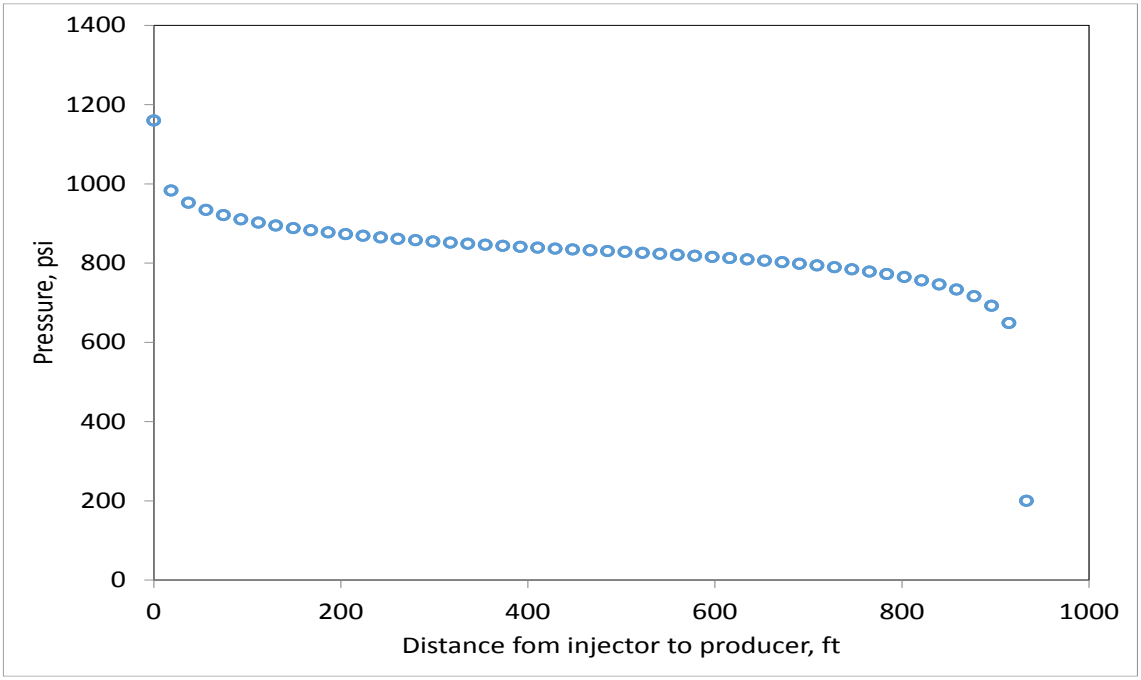


**Fig. 3-12 Reservoir pressure distribution from the injection well to the production well (2D model).**

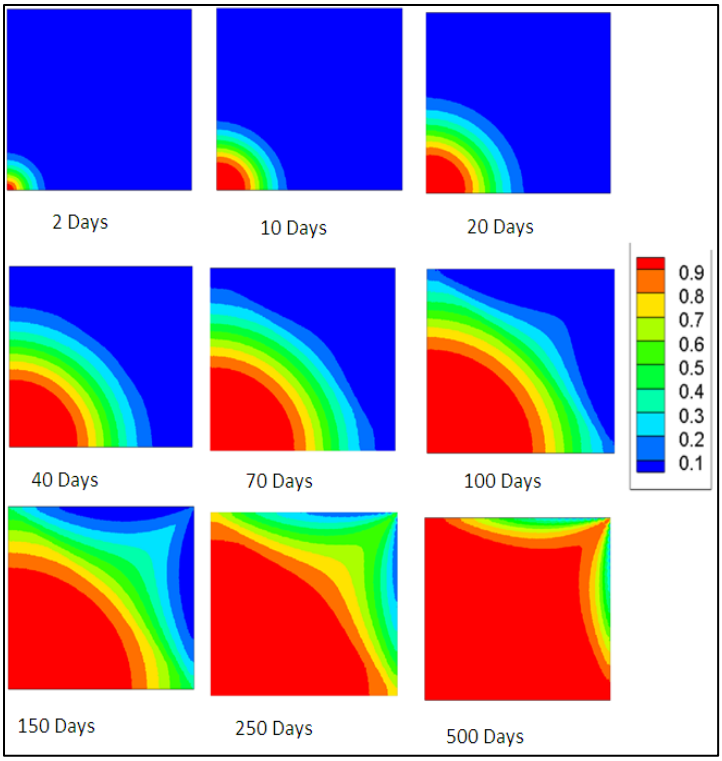


**Fig. 3-13 $CO_2$ concentration distribution in the reservoir with time (2D model).**

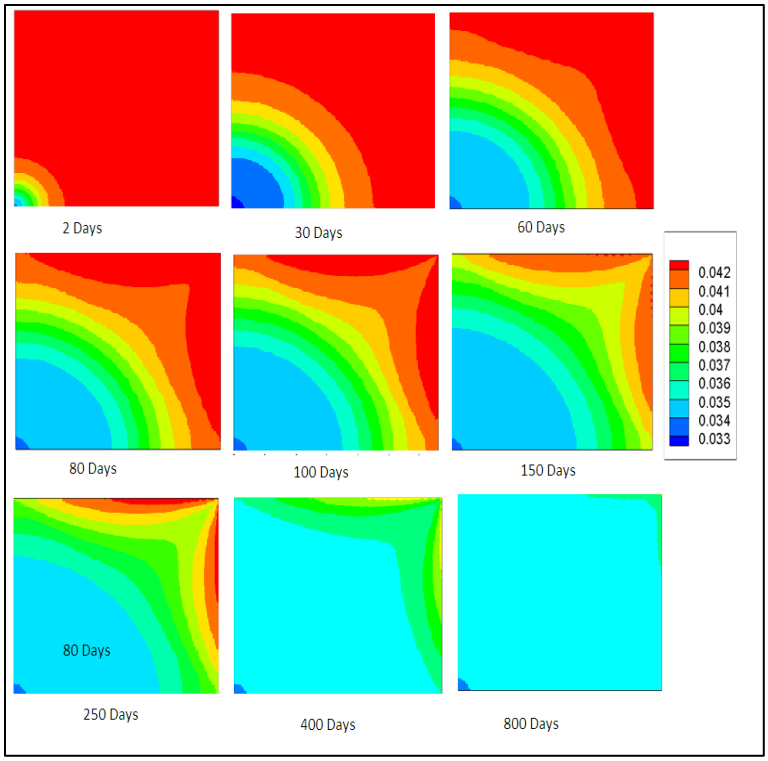


**Fig. 3-14 Porosity distribution in the reservoir with time (2D model).**

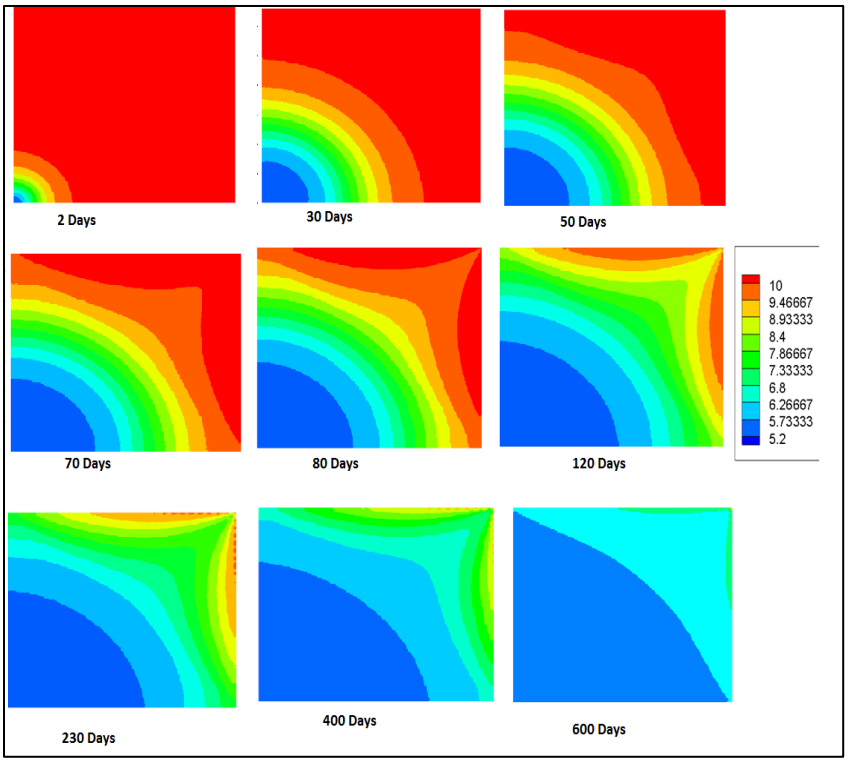


**Fig. 3-15 Permeability distribution in the reservoir with time (2D model).**

### 3.3. Effect of Injection and Production Conditions

In this section, the model was run at different injection and production pressures. The first case (Table 3-3) was used as a base case, then the injection pressure or the production pressure changed one per time to examine its effect. **Figs**. **3-16** and **3-17** show that the increasing of injection pressure or decreasing the production pressure improve the total flow rate but the injection pressure change is more effective than the production pressure change. The injection pressure and the production pressure almost does not affect the breakthrough time but it affects the methane production rate. The reduction in production pressure or increasing the injection pressure accelerate the methane production with no effect on the cumulative production.

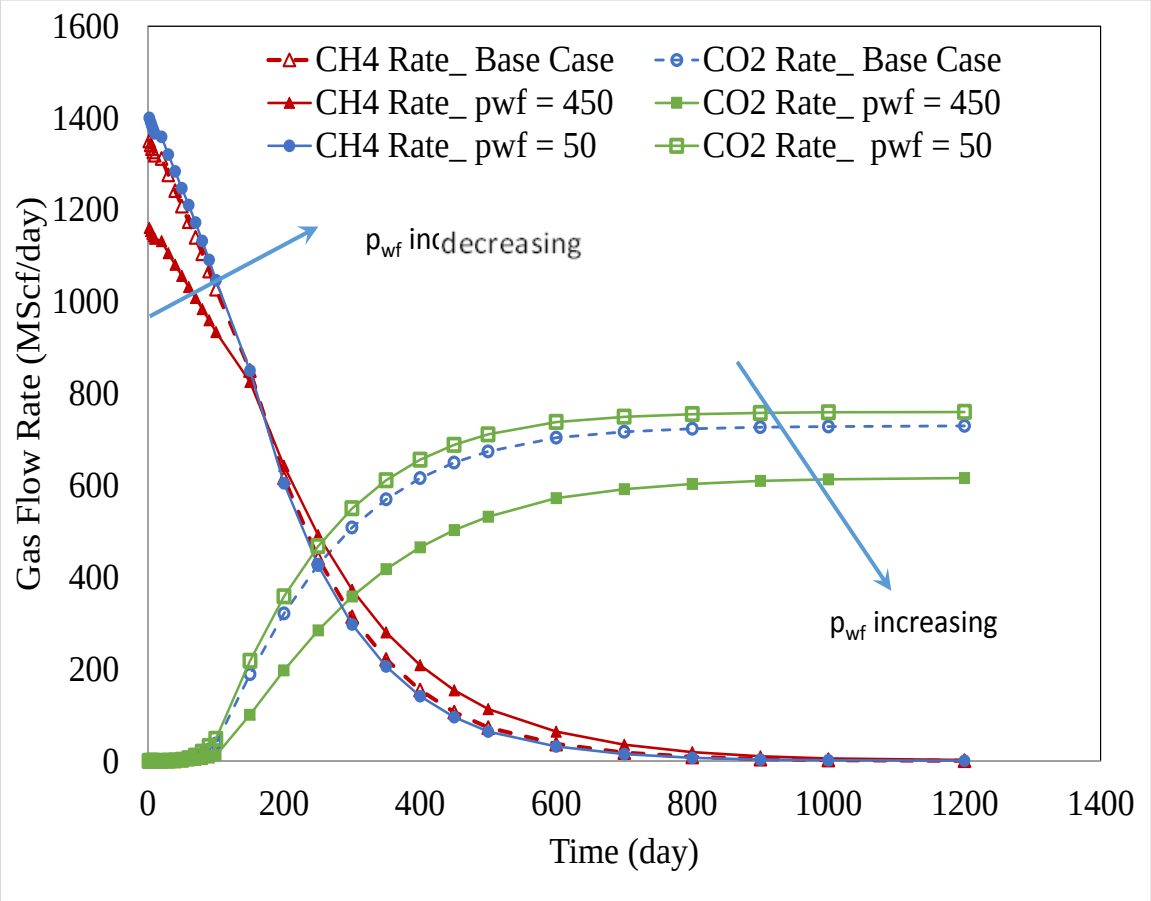


**Fig. 3-16 Effect of production pressure on $CO_2$ and $CH_4$ production behavior.**

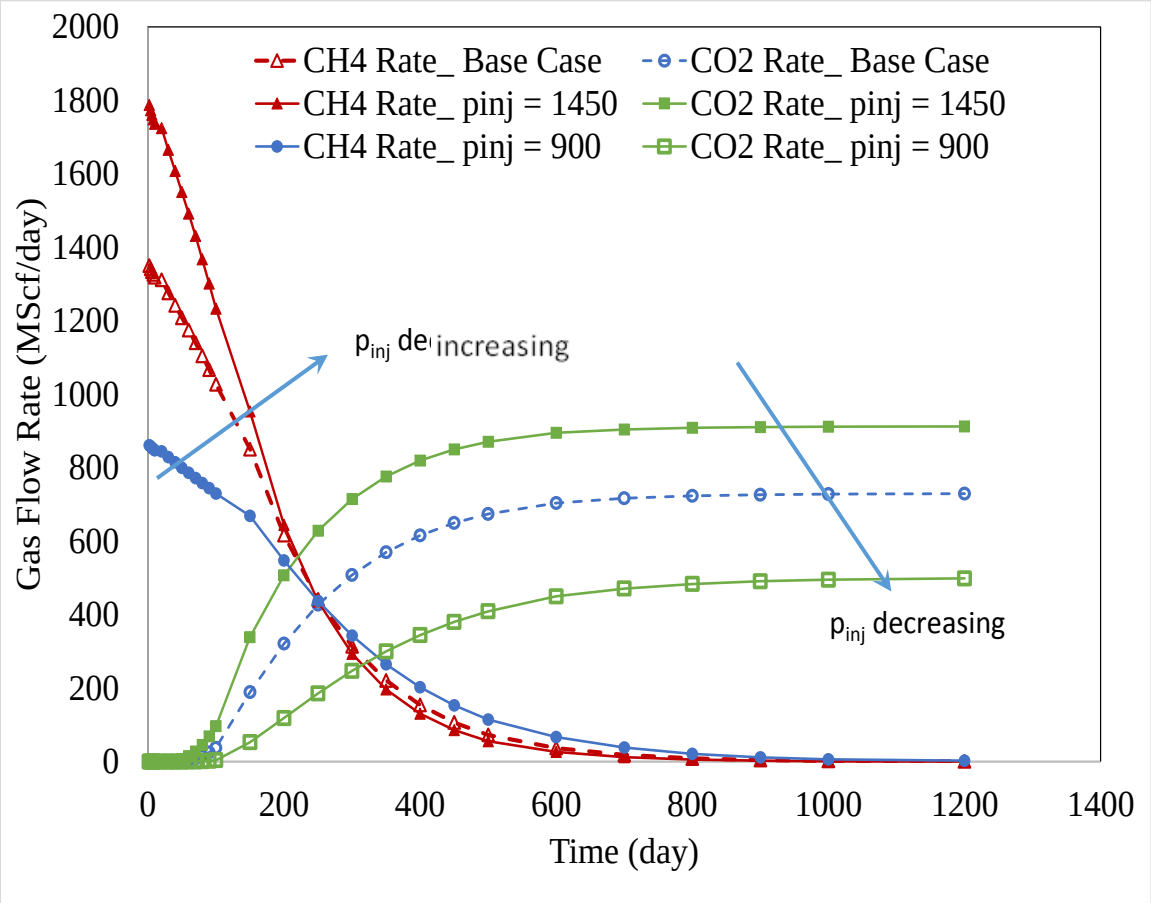


**Fig. 3-17 Effect of injection pressure on $CO_2$ and $CH_4$ production behavior.**

### 3.4. Effect of Injected Gas Properties

In this section, the model was run using different Langmuir pressures and volumes for the injected gas. The first case (Table 3-3) was used as a base case, then the Langmuir pressure or the volume changed one per time to examine its effect. **Figs**. **3-18** and **3-19** show that the Langmuir pressure or the volume doesn't affect the total flow rate, however, the total flow rate decreased with time as the Langmuir pressure decreased. This was due to permeability reduction as result of the matrix swelling increasing. Also, the decreasing of the Langmuir pressure of the injected gas delayed the $CO_2$ breakthrough. The methane production rate was improved due to the increasing of the Langmuir volume or decreasing the Langmuir pressure of the injected gas.

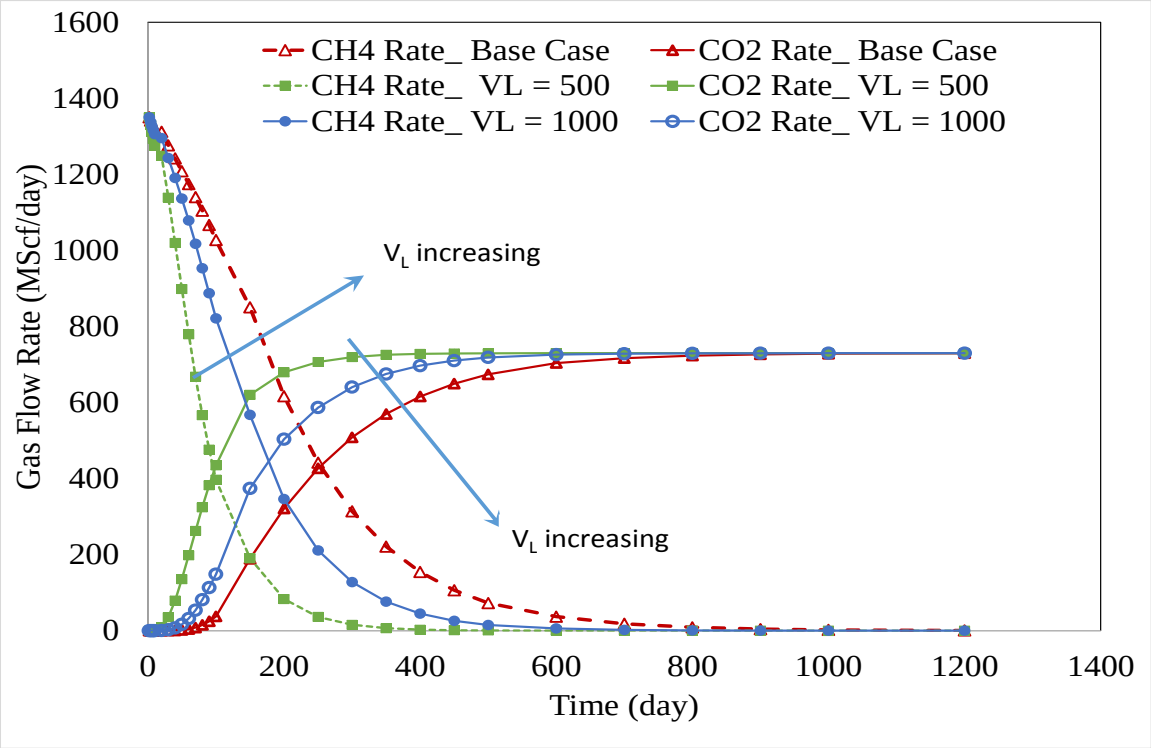


**Fig. 3-18 Effect of injected gas Langmuir volume on $CO_2$ and $CH_4$ production behavior.**

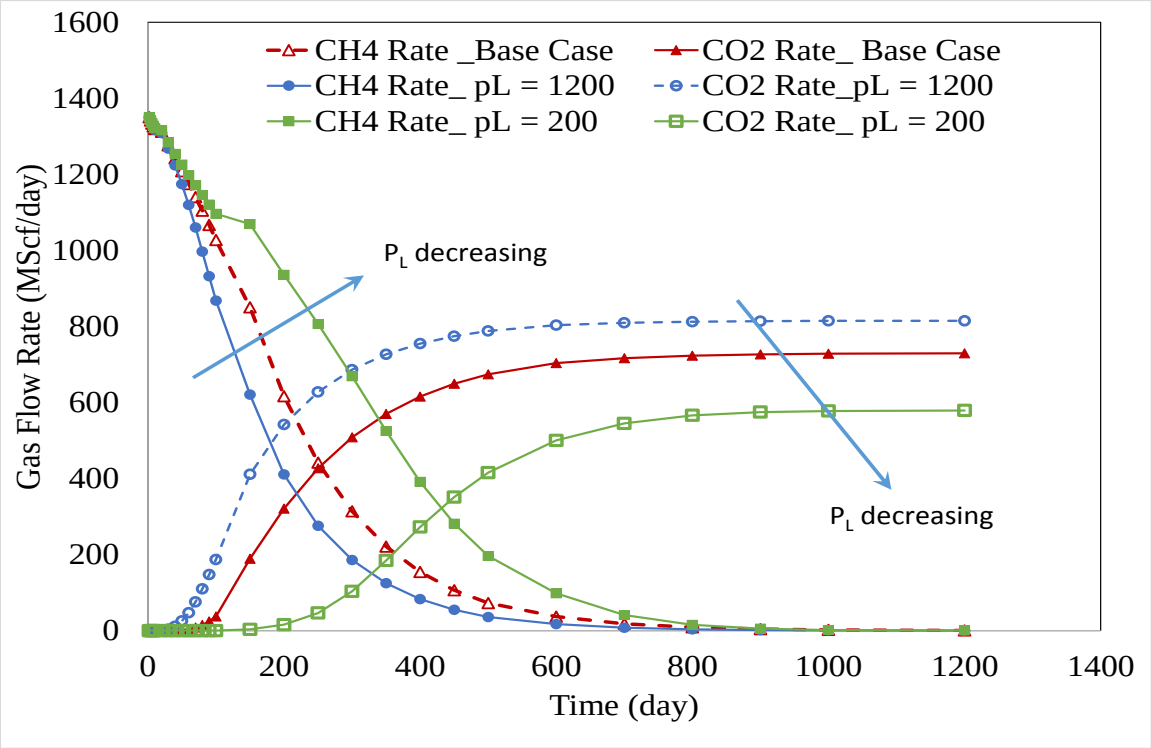


**Fig. 3-19 Effect of injected gas Langmuir pressure on $CO_2$ and $CH_4$ production behavior.**

# CHAPTER IV
# COAL WETTABILITY DURING $CO_2$ SEQUESTRATION IN COAL SEAMS[3]

## 4.1. Introduction

This chapter examines the effects of the coal seam water salinity and the injected gas composition on the wettability of a highly volatile bitumen coal–water–$CO_2$ system. A combination of contact angle, adsorption isotherm, and zeta potential measurements were used on the wettability investigation. In this study, the salinity was selected within the range of water salinities of different coal formations in different basins in the USA and Australia.(Hamawand et al. 2013) Also, the contact angle was measured through the dense phase. When a $CO_2$ bubble is placed on a mineral surface in the presence of a brine, typical scenarios for contact angle are as follows: 0°, completely water-wet (hydrophilic); 90°, neutral wettability; 180°, completely $CO_2$-wet (hydrophobic); > 90°, predominantly $CO_2$-wet; and < 90°, predominantly water-wet. The contact angle can be described by Young's equation(Young 1805) as follows:

$$\cos(\theta) = \left(\frac{\gamma_{SG} - \gamma_{SL}}{\gamma_{GL}}\right) \qquad 4\text{-}1$$

where $\theta$ is the contact angle measured in the liquid, $\gamma_{SG}$ is the gas/solid interfacial tension, $\gamma_{SL}$ is the liquid/solid interfacial tension, and $\gamma_{GL}$ is the gas/liquid interfacial tension (**Fig. 4-1)**.

[3] Reprinted with permission from "Effect of Water Salinity on Coal Wettability During CO2 Sequestration in Coal Seams" by Ibrahim, A. F., Nasr-El-Din, H. A. 2016. Energy & Fuels **30** (9): 7532–7542, Copyright 2016 by American Chemical Society.

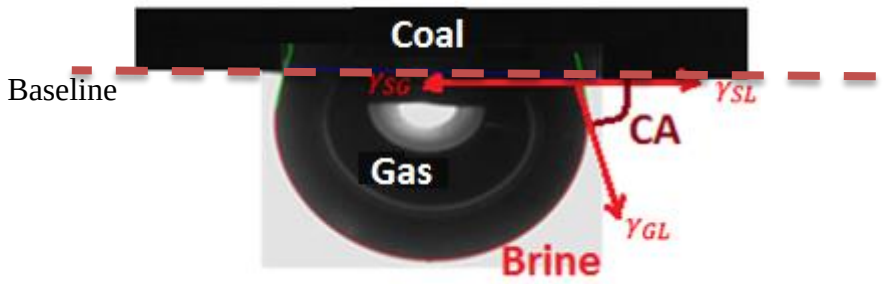


**Fig. 4-1 Schematic of a gas bubble showing the parameters in Young's equation.**

## 4.2. Materials

$CO_2$ and $N_2$ gas cylinders with purities greater than 99.99 mol% were used. The flue gas was prepared by mixing $CO_2$ and $N_2$ with the required concentrations (from 100% $CO_2$ to 100% $N_2$). NaCl, $MgCl_2$, and $CaCl_2$ salts (ACS grade) were added to deionized (DI) water with a resistivity of 18.2 Ω.cm at room temperature to prepare the brine with the required salinity.

Coal blocks were collected from the Bull Hill mine in Oklahoma. **Table 4-1** shows the proximate analysis for the coal sample.(Standard 2013) **Fig. 4-2** gives the EDS (energy-dispersive X-ray spectroscopy) mineral composition for the coal sample, and it shows a high carbon content of 82 wt%. Based on these measurements, this coal sample was classified as high volatile bitumen coal.

| Component | Concentration, wt% |
|---|---|
| Moisture | 0.2 |
| Volatile Matter | 47 |
| Fixed Carbon | 50.8 |
| Ash | 2 |

Table 4-1 Proximate,analysis for the coal sample.

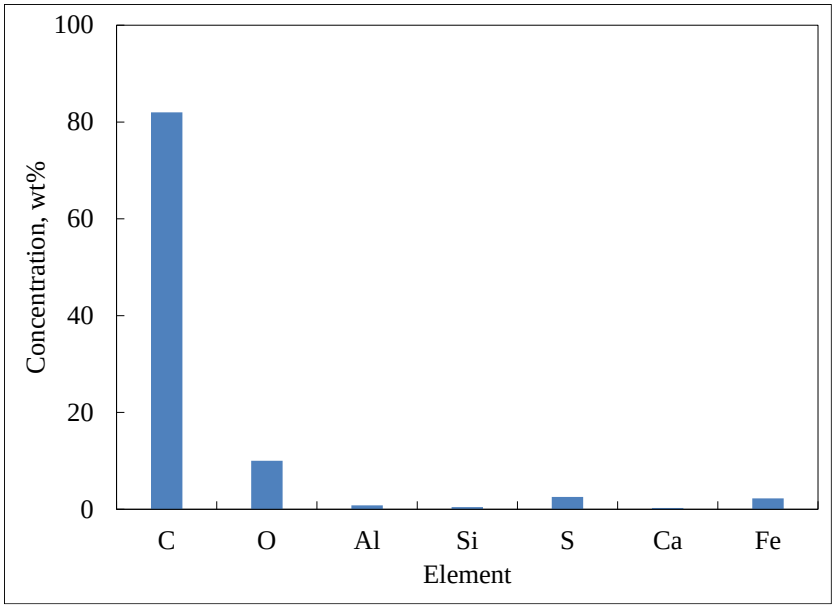


**Fig. 4-2 EDS analysis of a grinded coal sample.**

## 4.3. Experimental Setup and Procedures

**Contact Angle Measurements.** The captive bubble method was used to measure the contact angle in the coal–water–gas system. Contact-angle measurements were conducted using the drop-shape analysis system, DSA 100 (**Fig. 4-3**). The DSA system consisted of a hastelloy high-pressure cell (15 $cm^3$) with two transparent windows, a sample holder to keep the coal sample horizontal inside the cell, and a high-resolution camera linked to a computer for image capturing and processing. The cell was connected to a gas source, a stainless-steel piston accumulator, and a vacuum pump. A syringe pump was used to displace the water from the piston accumulator to the cell and pressurize it to the desired pressure (from atmospheric pressure up to 2000 psi). A capillary tube (needle with OD = 1 mm) was connected at the bottom of the cell and worked as a gas injection syringe, while the gas injection was controlled through a needle valve. The setup was adjusted so the fluid mixture can be circulated. A density meter was connected to the circulation loop to measure the density of the circulated fluid. Constant fluid density indicates (for more than 30 min) a complete saturation of the brine with $CO_2$ and equilibrium system condition.

Different coal samples with the dimensions of 0.25×0.7×1 in. were cut from the collected coal blocks. The surface of each sample was polished using a series of sandpapers (average particle diameter 35, 58.5, 100, and 125 μm) and was washed with water during the polishing operations. The sample was submerged in the required brine and evacuated using a vacuum pump to remove the air from the pores of the coal sample and force the water to fill the pore system. A new coal sample was used in each measurement.

The coal sample was set horizontally and placed inside the cell using a sample holder. The vacuum pump was used to evacuate the system (Fig. 4-3). The vacuum pump continued working while the water was injected into the cell. When the cell was filled with water, the vacuum pump was turned off. Valve 3 was closed, and the temperature was set at 40°C to make sure that $CO_2$ was always in a single phase, above the critical temperature.(Siemons et al. 2006; Sakurovs and Lavrencic 2011) The $CO_2$ was injected (through valve 4) to saturate the water and pressurize the system to the required pressure. The mixture was then circulated for more than five hours to make sure a complete saturation of the water with $CO_2$. The system was then left to rest for one hour (where the fluid density remains constant). A gas bubble was injected through the syringe by opening the needle valve slightly. The pressure inside the gas source accumulator had to be slightly higher than the cell pressure to overcome it.

Finally, an image was captured by the camera and then processed by DSA software. The baseline between the solid surface and the bubble (as in Fig. 4-1) was adjusted manually. The DSA software defines the bubble by the analysis of the gray level values of the image pixels. The program calculates the square root of the secondary derivative of the brightness level to get the point of highest change of brightness. The resulting drop shape was then fitted with different mathematical models. The first model tends to fit the bubble part near the baseline with a polynomial function (which is a result of numerous theoretical simulations). The slope at the three-phase contact point at the baseline, and from it the contact angle is determined using iteratively adapted parameters. The Young-Laplace method is also used to fit the bubble. The contact angle was then

calculated as a tanθ at the intersection of the baseline and the slope of the contour line (the green line in Fig. 4-1) at the three-phase contact point.

The pressure gradually increased to the next value, and the same manner was used to measure the next contact angle.

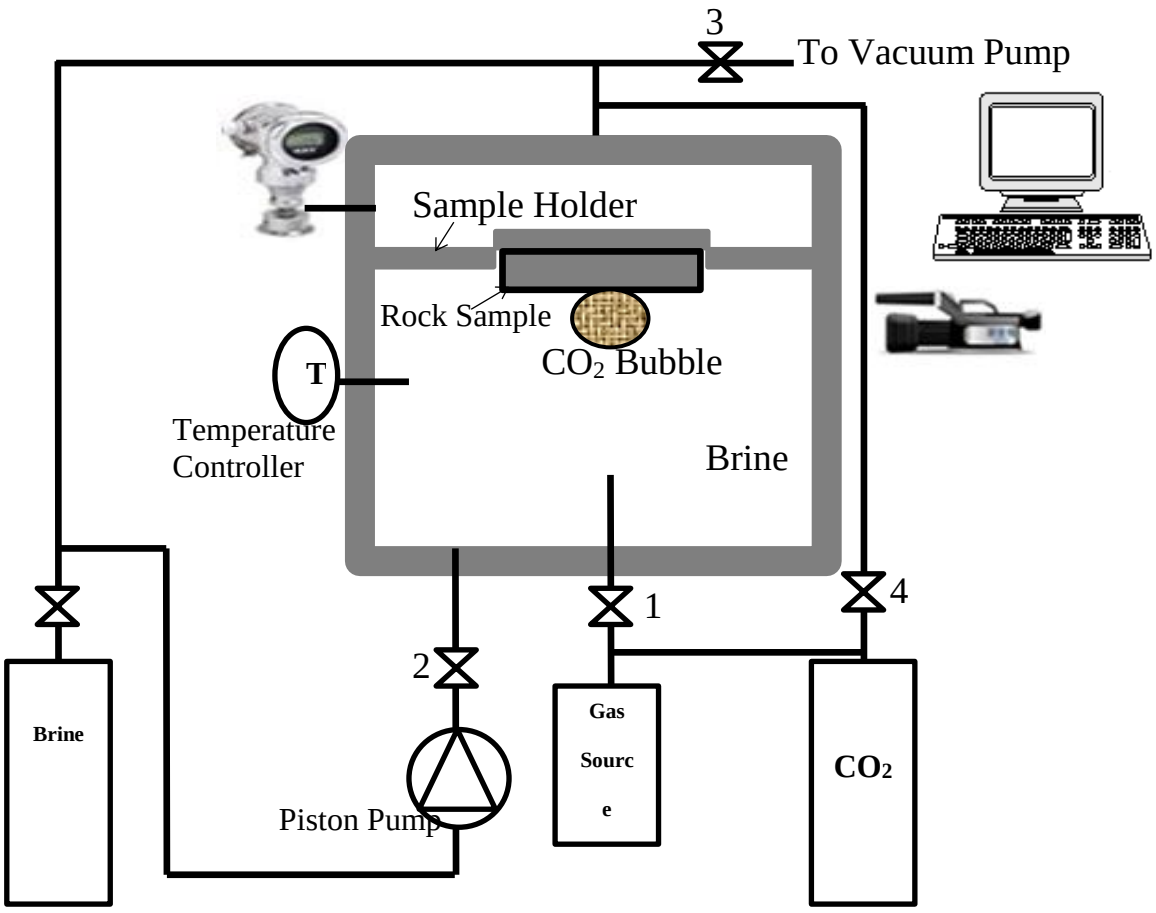


**Fig. 4-3 Schematic for the drop-shape analysis system that was used in contact-angle measurements.**

**Zeta Potential ($\xi$) Measurements**. A phase-analysis light-scattering (PALS) technique was used to determine the zeta potential of the suspensions.(Alotaibi et al. 2011) A polyether ether ketone (PEEK) electrode coated with palladium was used. A He-Ne laser

was used as a light source to measure the electrophoretic mobility of charged colloidal suspensions. A 1.5 $cm^3$ polystyrene cuvette was used to hold the sample.

To prepare the suspensions, coal samples were crushed by hand to pass through a #200 mesh (75 µm). Then, the coal samples were added to 1 g/l NaCl brine. A magnetic stirrer was used to mix the solution, and the pH was adjusted using HCl and NaOH for a pH range from 2 to 12 (10 pH values). Before each experiment, the solutions were kept still for five minutes to allow the coarse particles to settle out. Then, a 1.5 $cm^3$ sample was taken from the top using a pipet and transferred to a polystyrene cuvette.(Ozdemir 2013) For each experiment, the average of 10 runs was calculated and reported with a standard error of less than ± 3%.

**$CO_2$ Adsorption on Coal**. Adsorption isotherm measurements were conducted using the manometric method(Clarkson and Bustin 2000; Busch et al. 2003; Busch and Gensterblum 2011) to investigate the effect of water salinity on $CO_2$ adsorption on the coal surface at 40℃. **Fig. 4-4** shows the setup that was used for the measurements. It consisted of sample and reference cells (200 $cm^3$), both capable of withstanding high pressures (5,000 psi). A pressure transducer was connected to the system to measure the system pressure and was sent through a data acquisition system to a computer that records the data through LabVIEW™ software. The reference cell was connected to the gas cylinder. A vacuum pump was connected to the system to evacuate it. A stainless-steel mesh #325 was set at the ends of the sample cell to prevent migration of the coal particles.

Coal samples were crushed by hand and sieved through different sieve sizes. The samples that were collected between mesh sieves 20 and 40 (0.42 - 0.84 mm) were used in the measurements. The same particle size was used in all adsorption isotherm experiments to exclude the effect of surface area.(Maphala and Wagner 2012)

First, a 158 g coal sample was packed into the sample cell and saturated with 80 $cm^3$ of the required brine. The brine was then displaced by injecting $CO_2$ at varying flow rates, starting at low rates and then gradually increasing (1 ml/min to 10 ml/min), to reach the irreducible water saturation in the coal pack. Valve 3 was kept open until the pressure

in the sample cell was set to the atmospheric pressure. Valves 2 and 3 were closed, and $CO_2$ was then injected into the reference cell. Valve 1 was closed and the reference cell pressure was recorded ($P_r$). The number of moles in the reference cell was calculated using the gas equation of state:

$$\mathbf{n_r} = \frac{\mathbf{P_r V_r}}{\mathbf{Z_r RT}}, \quad 4\text{-}2$$

where $Z_r$ is the gas compressibility factor at reference cell conditions, calculated using Peng-Robinson EOS.[27](Peng, D.Y. and Robinson, D.B. 1976)(Peng, D.Y. and Robinson, D.B. 1976)(Peng, D.Y. and Robinson, D.B. 1976) Valve 2 was then opened, and the pressure was recorded until stabilization ($P_s$). The number of moles of $CO_2$ in the free phase was calculated from the stabilized pressure.

$$\mathbf{n_{free}} = \frac{\mathbf{P_s}\left(\mathbf{V_r} + \mathbf{V_{pore}}(\mathbf{1} - \mathbf{S_{wir}})\right)}{\mathbf{Z_s RT}} \quad 4\text{-}3$$

where $Z_s$ is the gas compressibility factor of free $CO_2$ in the system at stabilization pressure, and was calculated using Peng-Robinson EOS.[27] The number of $CO_2$ moles adsorbed on the coal surface was calculated as the difference between the number of $CO_2$ moles in the reference cell and the number of moles at $P_s$ and corrected for the adsorbed gas volume.

$$\mathbf{n_{adsorbed}} = (\mathbf{n_r} - \mathbf{n_{free}})/(\mathbf{1} - \frac{\boldsymbol{\rho_{free}}}{\boldsymbol{\rho_{adsorbed}}}) \quad 4\text{-}4$$

where $\rho_{adsorbed}$ is the density of adsorbed gas on the coal surface (for $CO_2$ = 1.18 g/cm$^3$).(Shimada et al. 2005) $\rho_{free}$ is the density of free gas the at stabilization conditions, calculated as follows:

$$\boldsymbol{\rho_{free}} = \frac{\mathbf{P_s M_{w\,CO2}}}{\mathbf{Z_s RT}} \quad 4\text{-}5$$

The adsorbed gas volume, $\mathbf{V_{adsorbed}}$, (scf) can be calculated by multiplying the number of moles by 379.2 (the volume of one mole of $CO_2$ at standard conditions $= \frac{\mathbf{Z_{sc}RT_{sc}}}{\mathbf{n\ P_{sc}}} = \frac{1\times10.72\times520}{1\times14.7} = 379.2$ scf).

For each pressure, the average of three measurements was calculated and reported with a standard error of less than ± 5%. In the ECBM industry and related reservoir simulation approaches, the well-known Langmuir equation is used as a simple method to provide a reasonable fit to most experimental data as a monolayer adsorption process:(Busch and Gensterblum 2011)

$$\mathbf{V_{adsorbed}} = \frac{\mathbf{V_L P}}{\mathbf{P+P_L}} \qquad 4\text{-}6$$

The data was fitted with the Langmuir equation (as a straight-line format ($\mathbf{P} = \mathbf{V_L}\ \frac{\mathbf{P}}{\mathbf{V_{adsorbed}}} - \mathbf{P_L}$) to estimate the Langmuir adsorption constants (by plotting the $\frac{\mathbf{P}}{\mathbf{V_{adsorbed}}}$ in the x-axis and P in the y-axis, $\mathbf{V_L}$ is the slope and $\mathbf{P_L}$ is intercept). This equation then can be used to estimate the adsorbed $CO_2$ volume at any pressure.

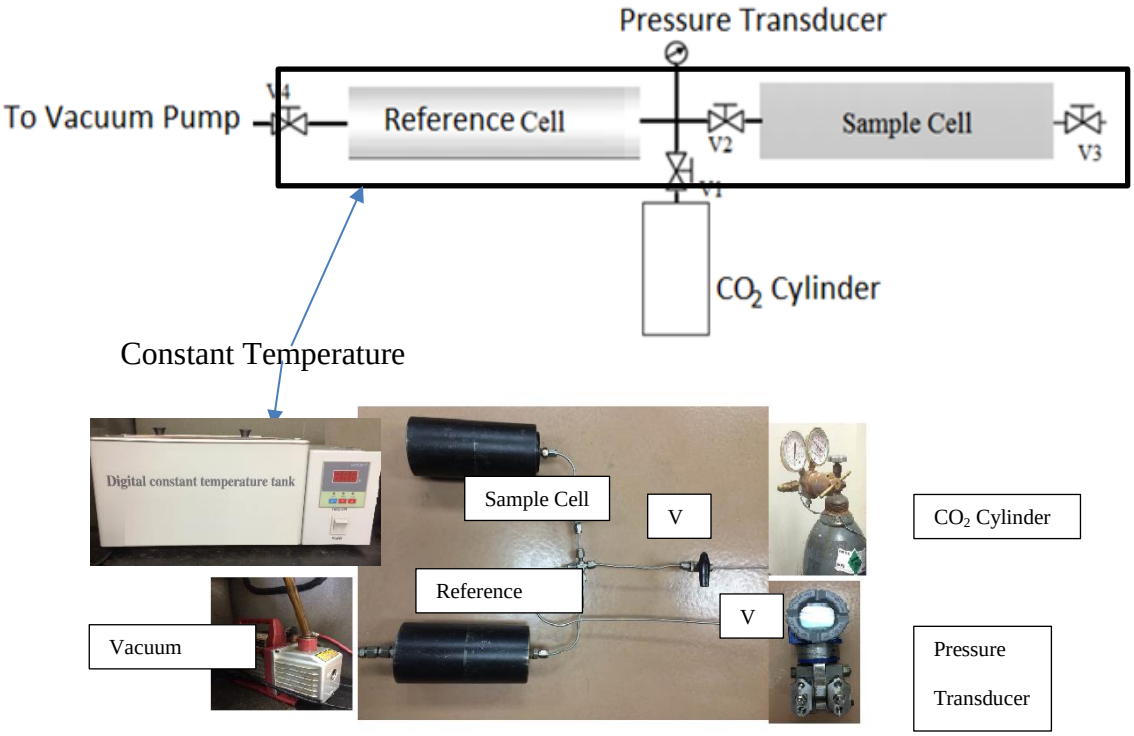


**Fig. 4-4 The set-up used to measure $CO_2$ adsorption on a coal sample (0.42 – 0.84 mm).**

**Coal Surface Analysis.** After contact angle measurements were conducted, the top surface of the coal specimens was analyzed using a SEM (Scanning Electron Microscope). The minerals on the coal surface were mapped using an Evex Mini Scanning Electron Microscope equipped with energy-dispersive X-ray spectroscopy (EDS). Also, SEM/EDS was used to analyze coal particles. In addition, a micro CT-scan was used after the contact angle measurements to determine the mineral matter and the fractures distribution in the coal specimens.

**Table 4-2** shows the element concentration was almost the same as the one from the grinded coal sample shown in Fig. 4-2, which reflect the homogeneity of the coal block. **Fig. 4-4** shows the mineral mapping on the top surface of coal specimen. The mineral mapping showed that the carbon and oxygen (reflect the organic content) were the base for the coal sample, and the carbon distribution was similar to the SEM photomicrograph of the coal surface. The inorganic mineral mapping showed a combination of iron-sulfate

and aluminosilicates components. **Fig. 4-5 and 4-6** show SEM photomicrographs for coal particles with different magnifications. The surface of the coal particles was not smooth but rough to an extent that increased the surface area and increased the $CO_2$ adsorption.(Li et al. 2013) **Fig. 4-7** shows micro CT-scan pictures of a coal specimen after contact angle measurements. Fig. 4-7 shows a map of the heavier mineral (i.e. silicates, iron sulfides) by the white areas and the fractures or voids by the black areas.

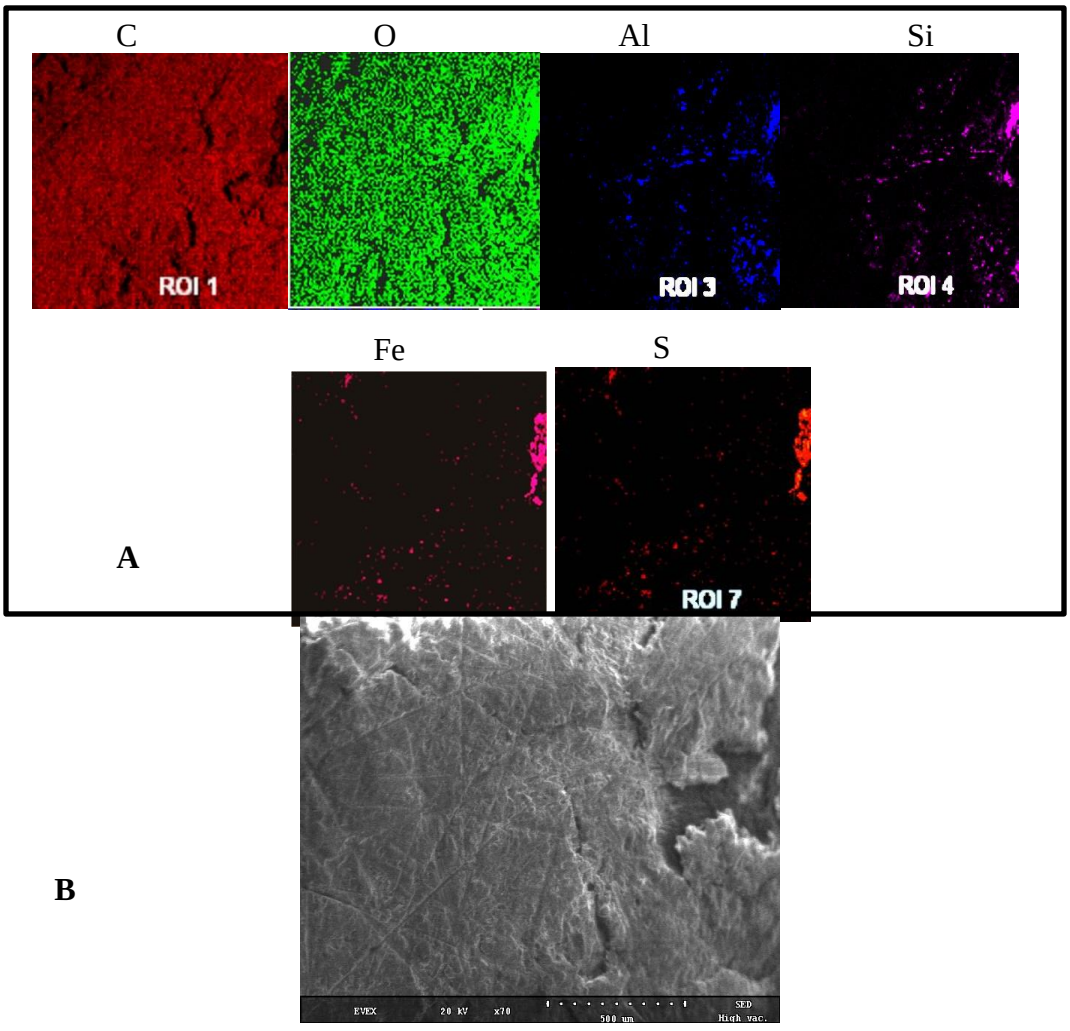


**Fig. 4-5 SEM/EDS analysis for the coal surface; (A) the mineral mapping on the coal surface, (B) SEM photomicrograph of the coal surface (70x).**

| Element | Concentration, wt% |
|---|---|
| C | 81 |
| O | 14.54 |
| Al | 0.6 |
| Si | 0.78 |
| S | 2.1 |
| Fe | 0.98 |

Table 4-2 EDS mineral analysis for the coal surface.

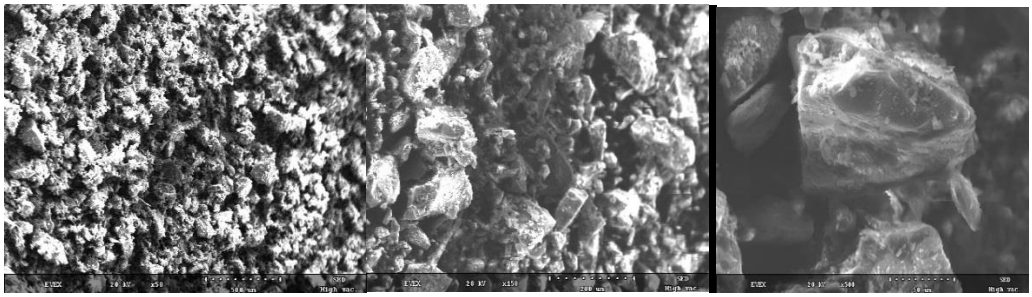

**Fig. 4-6 SEM pictures of coal particles with different magnification (50x, 150x, and 500x) to investigate the particle roughness.**

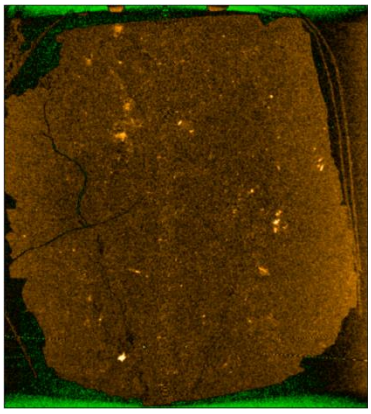

**Fig. 4-7 Micro CT-scan pictures of a coal specimen after contact angle measurements to map the heavier mineral (i.e. silicates, iron sulfides) by the white areas and the fractures or voids by the black areas.**

## 4.4. Results and Discussion

Contact-angle measurements were conducted at different pressures up to 2,000 psi. A general behavior for contact-angle experiments was observed. When the $CO_2$ bubble was released from the tip of the needle (in the equilibrium system), it floated on the coal surface. It moved to an optimum position in terms of gravity and interfacial force, which may not be directly above the needle. Once the bubble floated on the coal surface, the contact angle was measured as a function of time. The mean value of the right and left contact-angle values was recorded with an average error less than ± 5°. In most of the experiments, the contact angle remain constant from the beginning and the bubble size was constant; however, sometimes the contact angle slightly increased initially and then stabilized after a few minutes which indication for the equilibrium condition. Each experiment was repeated three times and the error was calculated as follows:

$$\in = \sqrt{\frac{1}{N}\sum_{1}^{N}(\boldsymbol{\theta_i} - \boldsymbol{\theta_m})^2} \qquad \textbf{4-7}$$

where N is the number of repeating the experiment, $\theta_i$ is the contact-angle value at each time, and $\theta_m$ is the average value.

The coal was water-wet ($\theta$ = 61°) for the DI water case at atmospheric pressure (**Fig. 4-8)**. As the pressure increased, the contact angle increased. The contact-angle increase was first high with a slope of 0.05 degree/psi ($\theta$ increased from 61° at atmospheric pressure to 110° at 1000 psi). After the pressure reached 1000 psi (where the $CO_2$ became a supercritical fluid), the contact angle became less steep with a slope of 0.01 degree/psi ($\theta$ increased from 114° at 1300 psi to 120° at 1900 psi). Similar performance was found by Ameri et al. where a sandstone sample changed sharply from intermediate $CO_2$-wet to $CO_2$-wet for the subcritical $CO_2$ phase, and then the contact angle slightly increased in the supercritical phase.(Ameri et al. 2013) Arif et al.(Arif et al. 2016) observed a similar trend in different coal ranks as shown in Fig. 4-8. Fig. 4-8 shows that the wettability altered from water-wet to $CO_2$-wet at pressures around 400 psi. The contact

angle increased to 123° at 1,950 psi, and the coal became more $CO_2$-wet. These results are in agreement with the literature presented by Shojai et al.[14] Fig. 4-8 shows the contact angle values for Siemons et al. are generally higher than the values in the present study. Two reasons may be contributed in this behavior. First, the contact angle measurements by Siemons et al. were conducted in non-equilibrium system where the water was not pre-equilibrated with $CO_2$. Consequently the mass transfer of $CO_2$ and water might have possibly affect the behavior.(Siemons et al. 2006) Second, the contact angle measurements by Siemons et al.[13] were conducted using anthracite coal, which is higher rank than the hvAb coal sample used in this study. According to Sakurovs and Lavrencic(Sakurovs and Lavrencic 2011) and Shojai et al.(Shojai Kaveh et al. 2012) the coal hydrophobicity increases as coal ranking decreases that affect the contact angle measurements. In comparing to the results by Shojai et al., a fair agreement with the contact angle measurements especial for hvBb coal sample and the difference between the two measurements is due to the coal rank-effect.

Moreover, Fig. 4-8 shows a comparison with contact-angle measurements by Arif et al.(Arif et al. 2016) for semi-anthracite, medium volatile bituminous, of lignite coal samples at 49℃**.** Lower values were found in the case of medium volatile bituminous, and lignite coal samples comparing to those of the present work. Lower coal rank and higher temperatures may account for these differences in the contact-angle values. Contact-angle measurements for semi-anthracite bituminous coal should be higher than those of the present work similar to the results obtained by Siemons et al.,[13] but the high temperature negates the high-rank effect.

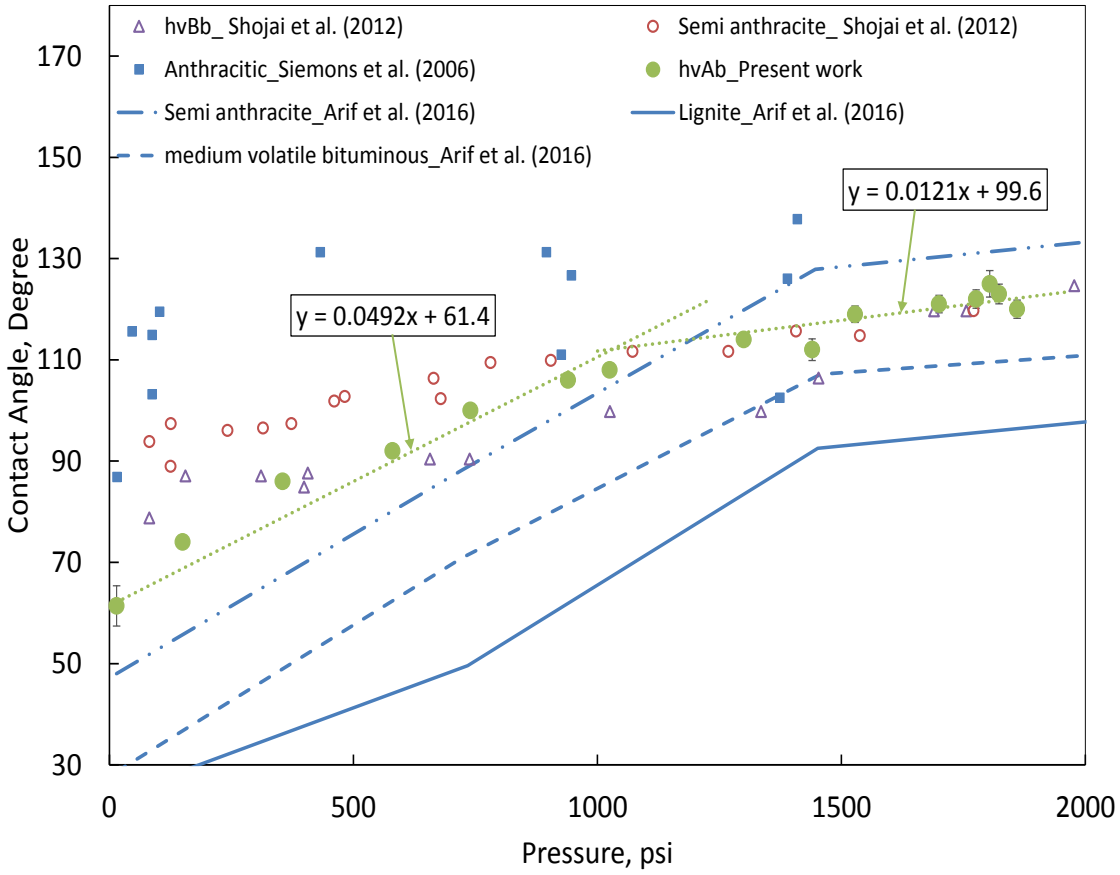


**Fig. 4-8 Comparison of determined contact-angle values plotted against those of (Siemons et al. (DI water, and 45℃), Shojai et al. (DI water, and 40℃), and Arif et al. (DI Water, and 49℃).**

The contact angle was measured at different NaCl concentrations up to 20 g/l NaCl, to investigate the effect of salt concentration on coal wettability. **Fig. 4-9** shows that the contact angle shifted up as the NaCl concentration increased the coal became more $CO_2$-wet, but this effect decreased with pressure.

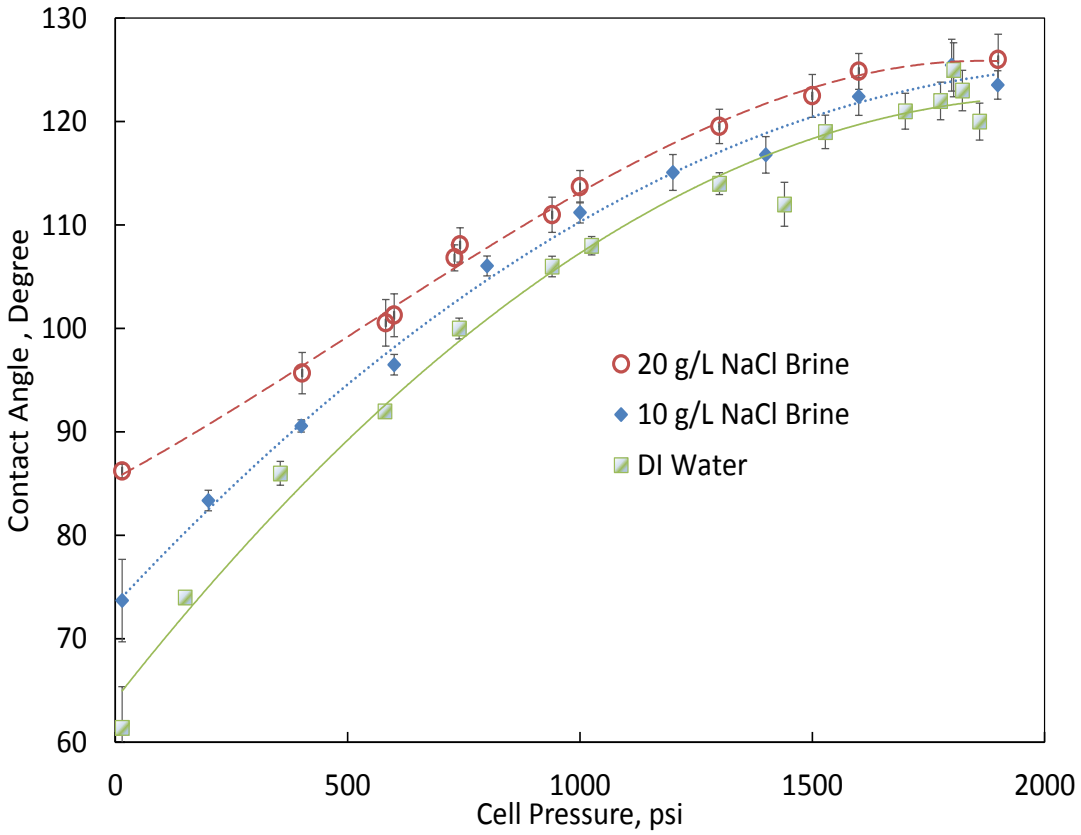


**Fig. 4-9 Contact angle as a function of cell pressure in the coal–water–$CO_2$ system at different NaCl concentrations.**

To understand these results, adsorption isothermal measurements were conducted using coal samples from the same block, which were initially saturated with brine at different salt concentrations. **Fig. 4-10** shows the adsorption isotherm at different NaCl concentrations. Result demonstrate that the $CO_2$ adsorption increased as the NaCl concentration increased. The Langmuir adsorption volume changed from 1,330 scf/ton in the DI water case to 1,788 scf/ton in the 20 g/l NaCl brine. According to Shojai et al.[14], the wettability behavior of $CO_2$ on the coal surface was greatly affected by $CO_2$ adsorption. Consequently, the increase in the contact angle with NaCl concentration is a reflection of the adsorption isotherm behavior as appears in Fig. 4-9.

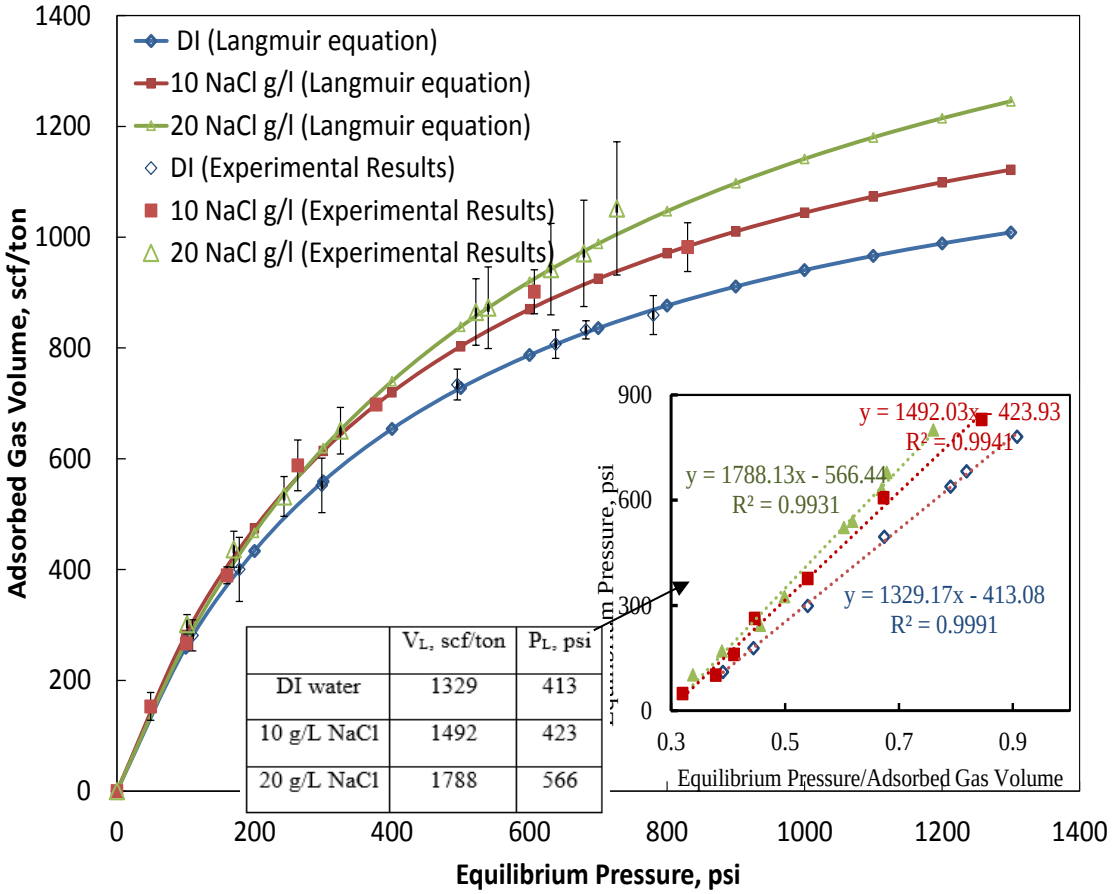


**Fig. 4-10 $CO_2$ adsorption isotherm as a function of salt concentrations, and fitted with Langmuir equation.**

Electrostatic interaction is one of the most important adsorption mechanisms. Zeta potential is a measure of the magnitude of electrostatic interactions between charged surfaces. **Fig. 4-11** shows the zeta-potential measurements for different salt concentrations versus pH. The zeta potential decreased as pH increased, and it changed from positive to negative at pH values between 7 and 8 (isoelectric point). Fig. 4-11 shows that as salt concentration increased, the absolute value for zeta potential decreased, which is in agreement with the literature.(Harvey et al. 2002; Salgın et al. 2012) The charge density and the electrostatic potential around the suspensions decrease (decay) exponentially with distance away from the particle surface. The inverse of the decay constant is called the Debye double layer thickness, a function of the ionic strength, which is, in turn, a function

of the salt concentrations. The higher the salt concentration, the faster the decay and the smaller the double layer thickness (the lower the absolute value of the zeta potential).(Salgın et al. 2012)

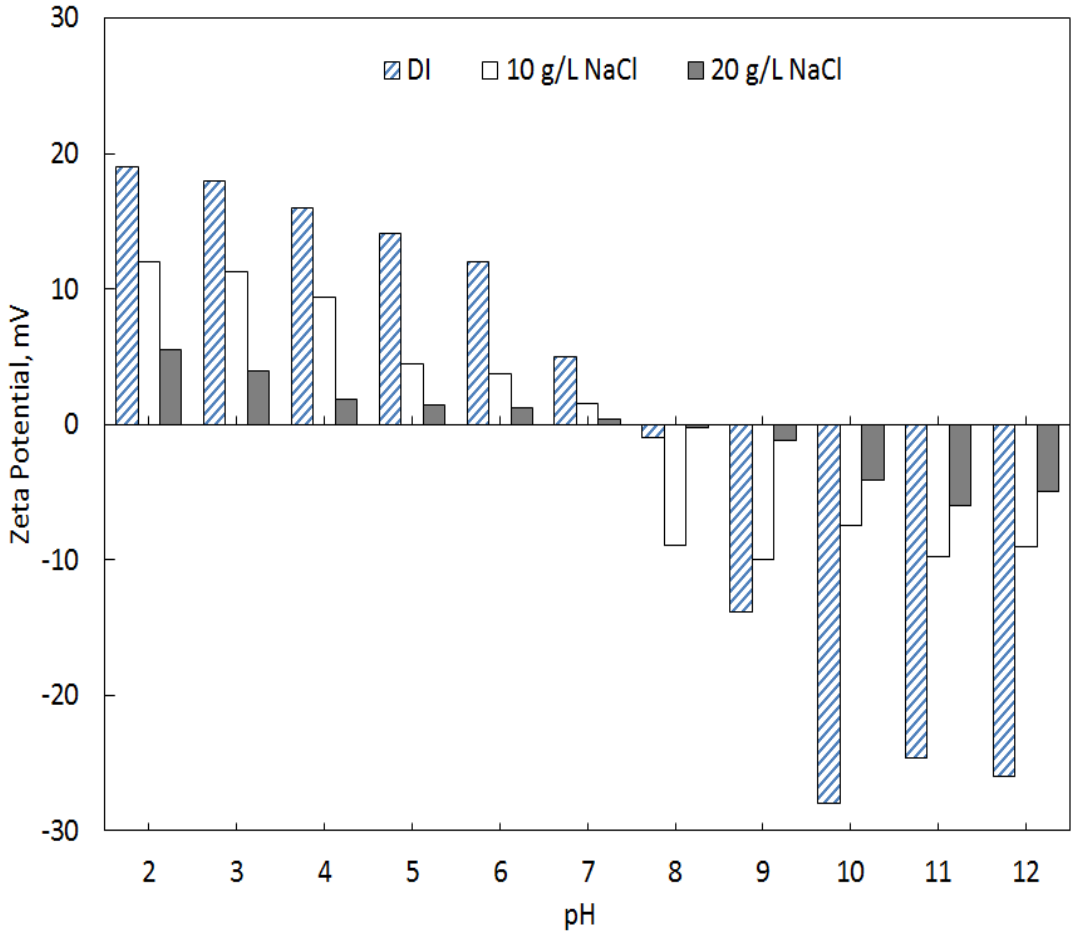


**Fig. 4-11 Zeta potential of coal particles (75 μm) in DI water and different salt solutions as a function of pH.**

Two factors affected the wettability behavior of the coal-water-$CO_2$ system during the pressure increase. First, the solubility of $CO_2$ in water increased, and $CO_2$ adsorption on the coal surface increases at high pressure. As the solubility of $CO_2$ in water increased, the pH decreases (the $CO_2$ in water forms a carbonic acid that decreases the pH).

Farokhpoor et al. (Farokhpoor et al. 2013) described the pH variation with the $CO_2$ solubility as follows:

The carbonic acid was produced from the reaction of dissolved $CO_2$ with water according to **Eq. 4-8**

$$\mathbf{CO_2 + H_2O \Leftrightarrow\ H_2CO_3} \qquad 4\text{-}8$$

The reaction equilibrium constant can be defined as $K_1 = \frac{[H_2CO_3]}{[CO_2]}$.

$H_2CO_3$ dissociates in water according to **Eq. 4-9**:

$$\mathbf{H_2CO_3 \Leftrightarrow HCO_3^- + H^+} \qquad 4\text{-}9$$

The reaction equilibrium constant can be defined as $K_2 = [HCO_3^-] \times [H^+]/[H_2CO_3]$.

Millero and Roy[33] reported that the equilibrium constants for Eqs. 8 and 9 are $K_1 = 2.612 \times 10^{-2}$ and $K_2 = 9.7 \times 10^{-7}$.

$HCO_3^-$ and $H_2O$ dissociate according to **Eqs. 4-10** and **4-11**:

$$\mathbf{HCO_3^- \Leftrightarrow CO_3^{-2} + H^+} \qquad \mathbf{K_c = 4.69 \times 10^{-11}} \text{ at } 25°C \qquad 4\text{-}10$$

$$\mathbf{H_2O \Leftrightarrow OH^- + H^+} \qquad \mathbf{K_w = 1.8 \times 10^{-16}} \text{ at } 25°C \qquad 4\text{-}11$$

Eqs. 4-8 – 4-11 describes the $CO_2$-$H_2O$ reaction system. Conducting a charge balance on the system yields the following equation.

$$[\mathbf{H^+}] = [\mathbf{HCO_3^-}] + \mathbf{2}[\mathbf{CO_3^{-2}}] + [\mathbf{OH^-}] \qquad 4\text{-}12$$

The coefficient (2) in **Eq. 4-12** is present because each mole of $CO_3^{-2}$ requires 2 moles of $H^+$ to neutralize.The dissociation of $\mathbf{H_2O}$ and $\mathbf{HCO_3^-}$ is very small so the concentration of $[CO_3^{-2}]$ + $[OH^-]$ can be ignored. Therefore Eq. 12 can be reduced to **Eq. 4-13**.

$$[\mathbf{H^+}] = [\mathbf{HCO_3^-}] \qquad 4\text{-}13$$

The pH can be calculated with $pH = -\log_{10}[H^+]$.

**Fig. 4-12** shows the solubility of $CO_2$ in DI water and 20 gm/L NaCl brine and pH with saturation pressure. In both brine and DI water, pH decreased rapidly with saturation pressure at the beginning then slightly decreased. pH decreasing reduces the density of the

negative charge at the water/$CO_2$ and solid/water interfaces.(Chiquet et al. 2007) Hence, the repulsive force between the two interfaces becomes less effective at high pressure, that destabilizes the water film on coal surface, and the coal becomes more hydrophobic.

Furthermore, adsorption-isotherm measurements show that the $CO_2$ adsorption onto the coal surface increased along with pressure as shown in Fig. 4-10, which in agreement with Busch and Gensterblum's results.[25] Hence, the gas interfacial tension to the solid decreased significantly,(Espinoza and Santamarina 2010) which increased the contact angle with pressure. Additional analysis of the interfacial forces will be presented in the next section.

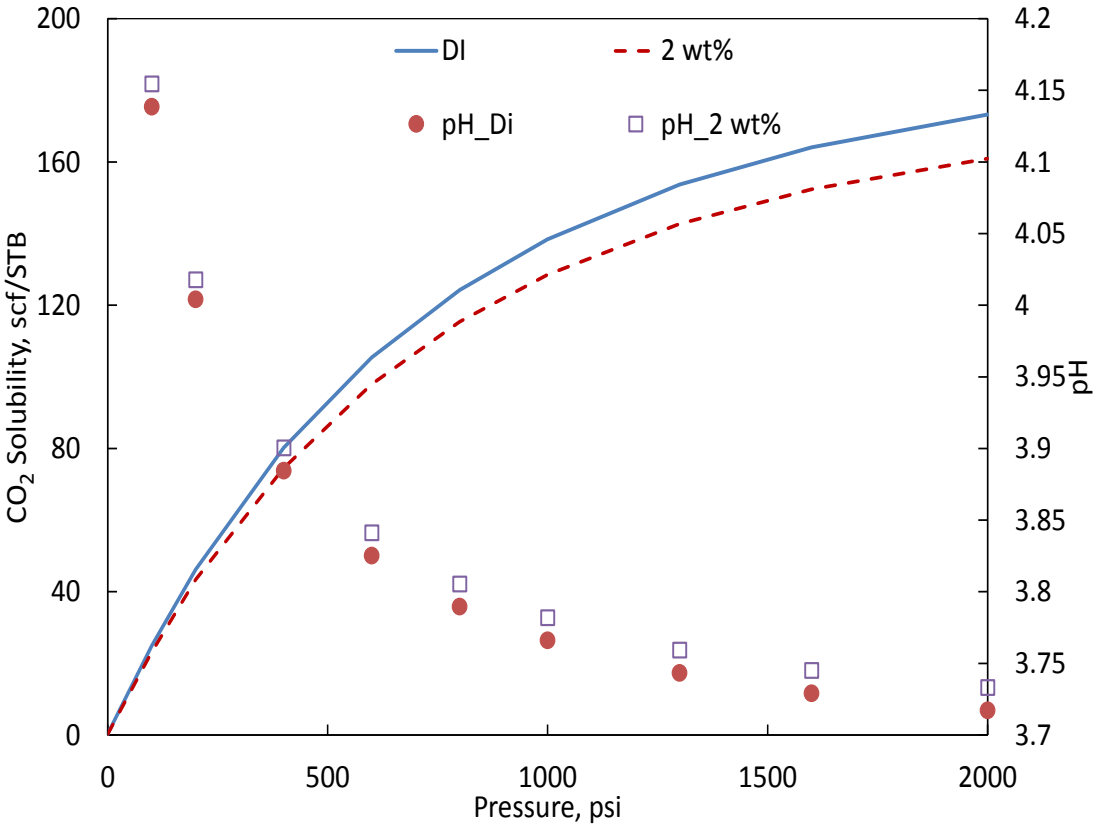


**Fig. 4-12 pH and $CO_2$ solubility as a function of salinity and pressure.**

As the salt concentration increases, it slightly decreases the solubility of $CO_2$ in water but this has a low effect on the pH (Fig. 4-12). For example at 2000 psi, a 175 scf of $CO_2$ dissolved in STB of DI water was needed to decrease the pH to 3.72. Compared to 2 wt% NaCl brine, $CO_2$ solubility is 165 scf/STB. The solubility difference is around 10, which changes the pH by only 0.03 (from 3.71 to 3.74), as it is a logarithmic scale difference. As a result, the effect of salt (within the studied range) on the pH can be neglected. Furthermore, as salt concentration increases, it compresses and destabilizes the hydrated layers (double layer) surrounding the coal surface, causing a reduction in the absolute value of the zeta potential, and making the coal surface more hydrophobic. The destabilization of the hydrated layer improves the contact of the $CO_2$ with the coal surface, resulting in a faster diffusion of the $CO_2$ from the gas phase to the coal surface, which enhances the $CO_2$ adsorption (as appear in adsorption isotherm measurements). All of these parameters enhance the coal to $CO_2$ wettability and increase its hydrophobicity. Similar results were observed by Nasralla et al. in the salinity effect on the wettability of oil-brine-sandstone system.(Nasralla et al. 2013) These researchers found that the sandstone became less water wet with salinity increasing as a result of the reduction of the negative charge on the brine/rock interface, which shrinks and destabilizes the water film surrounding the rock.

The effect of salinity on the contact angle can be explained from Young's equation as a function of the three interfacial forces. Kwok and Neumann relate the contact angle to the gas interfacial tension to the solid ($\gamma_{SG}$), the liquid interfacial tension to the solid ($\gamma_{SL}$), and the gas/liquid surface tension ($\gamma_{GL}$).(Kwok and Neumann 2000) This relation is called the equation of state, as shown below(Kwok and Neumann 2000);

$$\cos\theta = 1 - 2\sqrt{\gamma_{SL}/\gamma_{GL}}\left(1 - B_1(\gamma_{GL} - \gamma_{SL})^2\right) \quad 4\text{-}14$$

$\gamma_{SG}$ can be calculated as follows:

$$\gamma_{SG} = \gamma_{SL} + \gamma_{GL} - 2\sqrt{\gamma_{SL}\gamma_{GL}}\left(1 - B_1(\gamma_{GL} - \gamma_{SL})^2\right) \quad 4\text{-}15$$

To understand the effect of water salinity on coal wettability and its relation with the interfacial tension forces, the same approach by Ameri et al.(Ameri et al. 2013) was applied in this study. Ameri et al.(Ameri et al. 2013) used the equation of state to predict

the contact-angle values with pressure. This approach was based on using the gas/liquid interfacial tension data versus pressure and a couple of contact angle values to predict the contact angle with pressure and to estimate both gas/solid and liquid/solid interfacial tensions. **Fig. 4-13** shows the gas/liquid interfacial tension in DI water and NaCl brine. This experimental data was collected by Ameri et al., showing that the interfacial tension slightly increases with increasing NaCl concentration.

For DI water and NaCl brine cases, Eq. 4-14 was solved by using two set of values for contact angle and gas/liquid surface tension ($\gamma_{GL}$) to estimate B1 and $\gamma_{SL}$ in both cases. B1 and $\gamma_{SL}$were estimated to be 1.8E-4 $(m/mN)^2$ and 20 mN/m, respectively, in the case of DI water compared to 9.135E-5 $(m/mN)^2$, and 22 mN/m in the case of 20 g/L NaCl brine. These values were then used to calculate the contact angle and the $\gamma_{SG}$ versus pressure using eqs. 14 and 15.

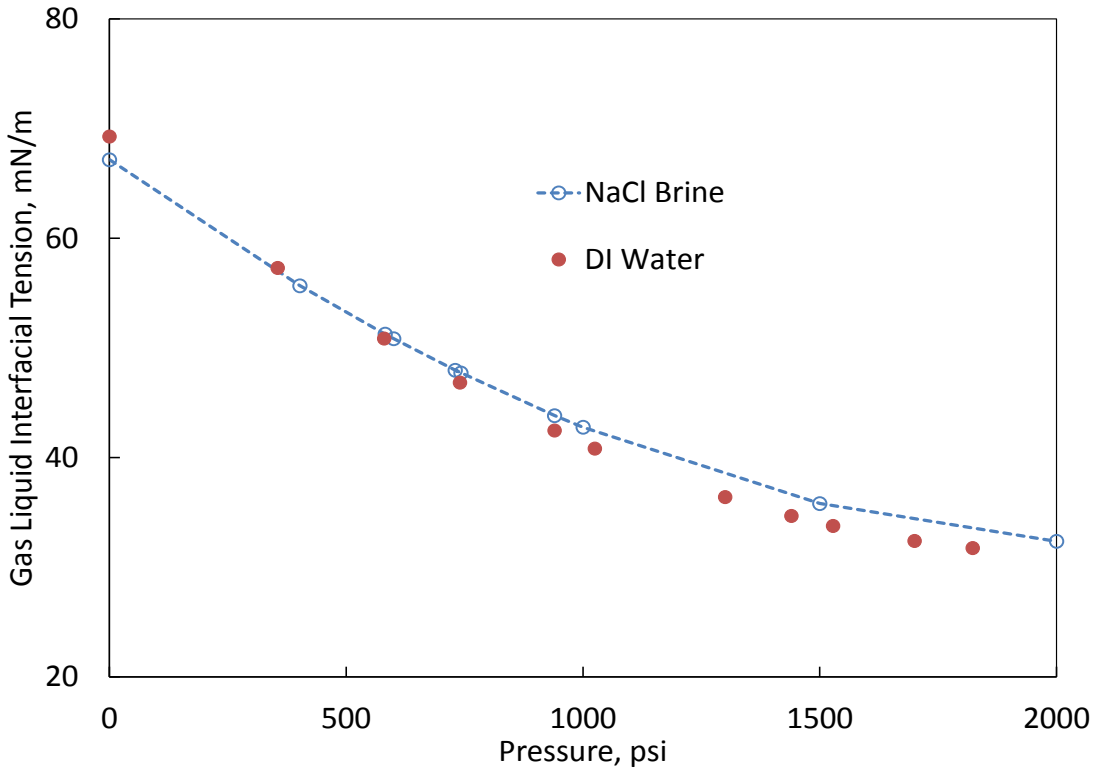


**Fig. 4-13 Gas/liquid interfacial tension in DI water and NaCl brine, as in Ameri et al.(Ameri et al. 2013).**

**Fig. 4-14** shows the calculated and the experimental contact-angle results, and a good match was observed in the case of DI water and NaCl brine. The average error between the experimental and the calculated data can be calculated as following:

$$\boldsymbol{Error} = \frac{\mathbf{1}}{\boldsymbol{N}} \sum_{\mathbf{1}}^{\boldsymbol{N}} \frac{(\boldsymbol{\theta_{calc}} - \boldsymbol{\theta_{exp}})}{\boldsymbol{\theta_{exp}}}, \quad 4\text{-}16$$

where, n is the number of points, and $\theta_{calc}$ and $\theta_{exp}$ are the contact-angle values as calculated from Eq. 4-14 and the experimental results, respectively. The average error was found to be 1.9 and 1.2 % for DI water and NaCl brine, respectively. Fig. 4-14 show that Eq. 4-14 can be used to reproduce the contact-angle values within an error less than 2%. Broadly, the EOS method can be used to examine the wettability performance of a certain surface if two reliable values of contact angle and interfacial tension are available for the system.

**Fig. 4-15** shows the estimated $\gamma_{SG}$ as function of pressure and salinity. It shows that $\gamma_{SG}$ decreases with pressure. As $\gamma_{SG}$ decreases with pressure at constant $\gamma_{SL}$, the numerator in Young's equation (Eq. 4-1) will be more negative. Also, the decrease of $\gamma_{GL}$ in the denominator will make the cos(θ) more negative. This results agrees with the result by Espinoza and Santamarina[34] as the gas interfacial tension to the solid decreased significantly with $CO_2$ adsorption onto the coal surface.

Lower $\gamma_{SG}$ values were found in case of NaCl brine comparing to DI water at low pressure (< 1000 psi) that is indication for increasing the coal surface hydrophobicity with salinity. Moreover, these results also confirmed by the adsorption isotherm measurements in Fig. 4-10.

The effect of salinity on $\gamma_{SG}$ decreased at high pressure. As a result, the contact-angle values for brine and DI water converge at high pressure.

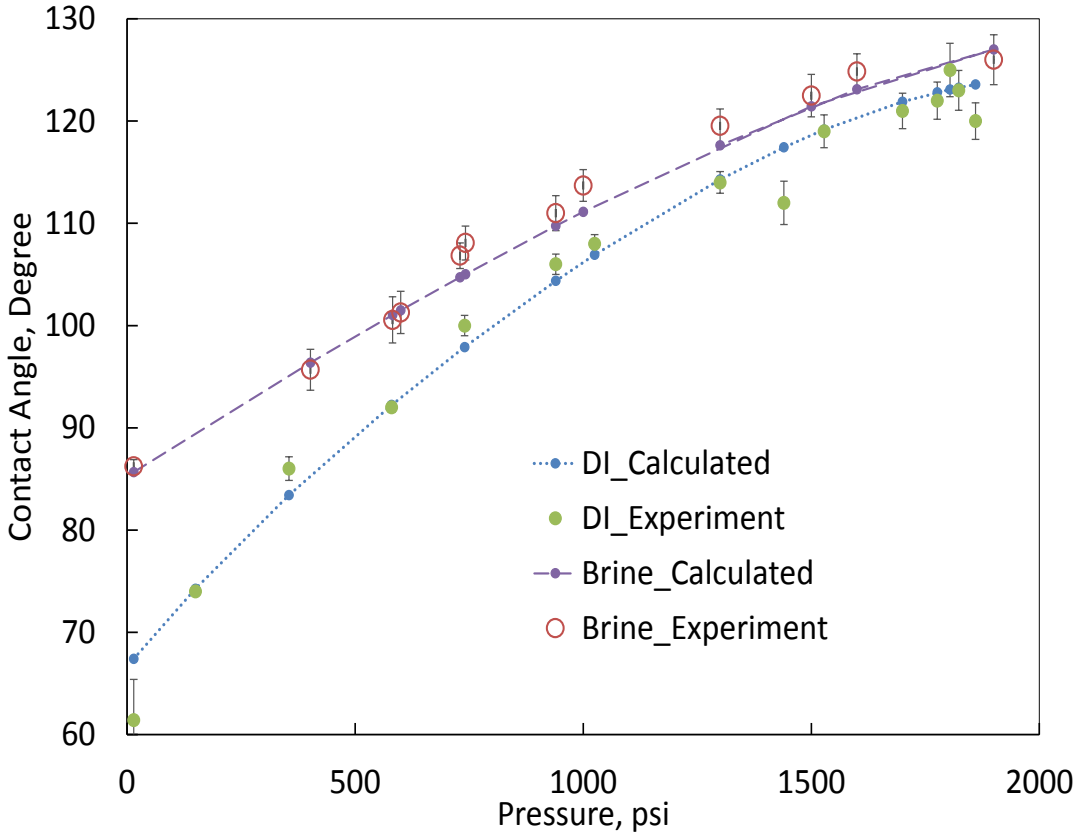


**Fig. 4-14 The calculated and the experimental contact angles.**

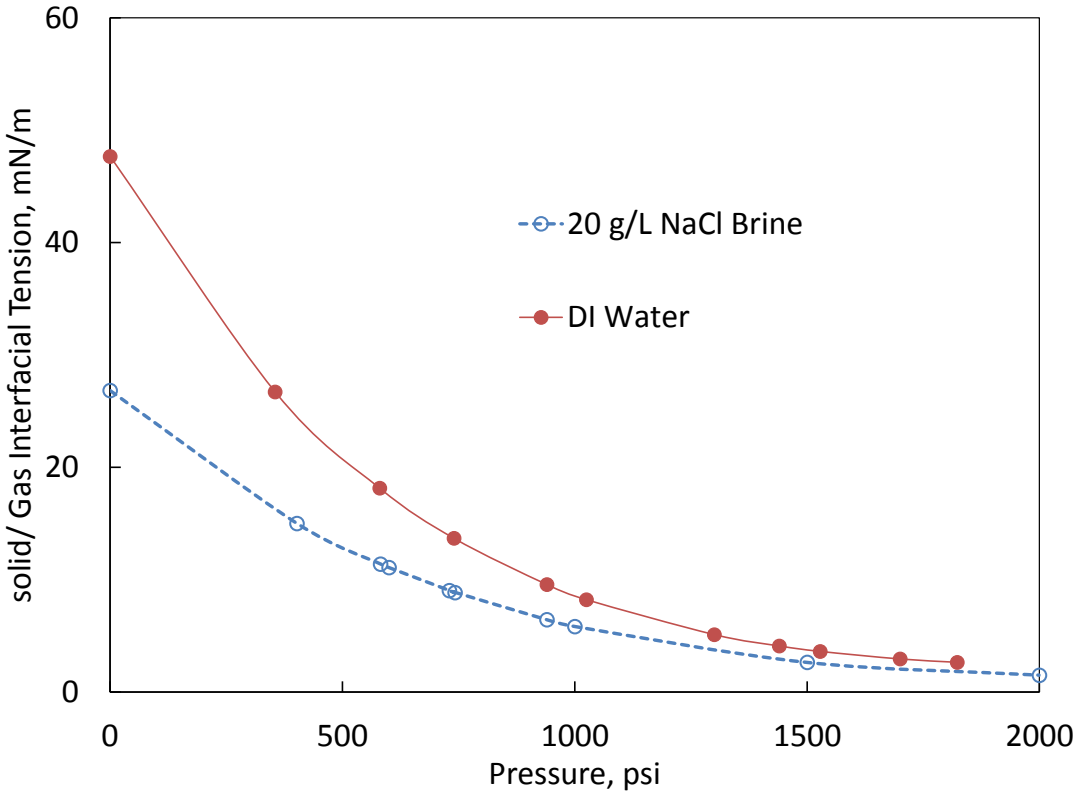


**Fig. 4-15 The estimated $\gamma_{SG}$ as a function of pressure and salinity.**

To investigate the effect of divalent cations on the contact-angle behavior, contact angle was measured at 500 psi and 1500 psi for 20 g/L $CaCl_2$ brine. Then, the EOS was used to predict the contact-angle behavior with pressure. $CO_2$-brine interfacial tension was used from the experimental measurements by Aggelopoulos et al. (2010, 2011).[37,38] B1 and $\gamma_{SL}$were estimated to be 1.6E-4 $(m/mN)^2$ and 24 mN/m, respectively. These values were then used to calculate the contact angle and the $\gamma_{SG}$ using eqs. 14 and 15 versus pressure. **Fig. 4-16** shows the contact angle values in comparing to those for DI water and NaCl brine cases. $CaCl_2$ increased the contact angle values comparing to DI water, but its effect was slightly lower than for NaCl. The estimated $\gamma_{SL}$ was higher than that for DI water (19 mN/m) and NaCl (22 mN/m), which indicates to higher water hydrophobicity. This behavior was confirmed by zeta-potential measurements as shown in **Fig. 4-17**. The low absolute zeta potential in the case of $CaCl_2$ brine represents the destabilization of

water layer sandwiched between the $CO_2$ bubble and the coal surface (decrease the double layer thickness). As a result, the contact angle was higher than that of DI water and the rock become more $CO_2$-wet. The effect of $CaCl_2$ on contact angle was slightly lower than NaCl effect. This can be explained by the contradictory effect of the $CO_2$-brine interfacial tension changes. Based on results obtained by Aggelopoulos et al.,[38] the $CO_2$-brine interfacial tension is higher in case of $CaCl_2$ comparing to NaCl brine. As a result, the increase of the denominator in Young's equation (Eq. 4-1) will make the cos(θ) less negative and the contact angle decreases.

These results indicate that the presence of salts in the formation water increases the contact angle and make the coal surface more $CO_2$-wet, but this behavior is also affected by the $CO_2$-brine interfacial-tension changes.

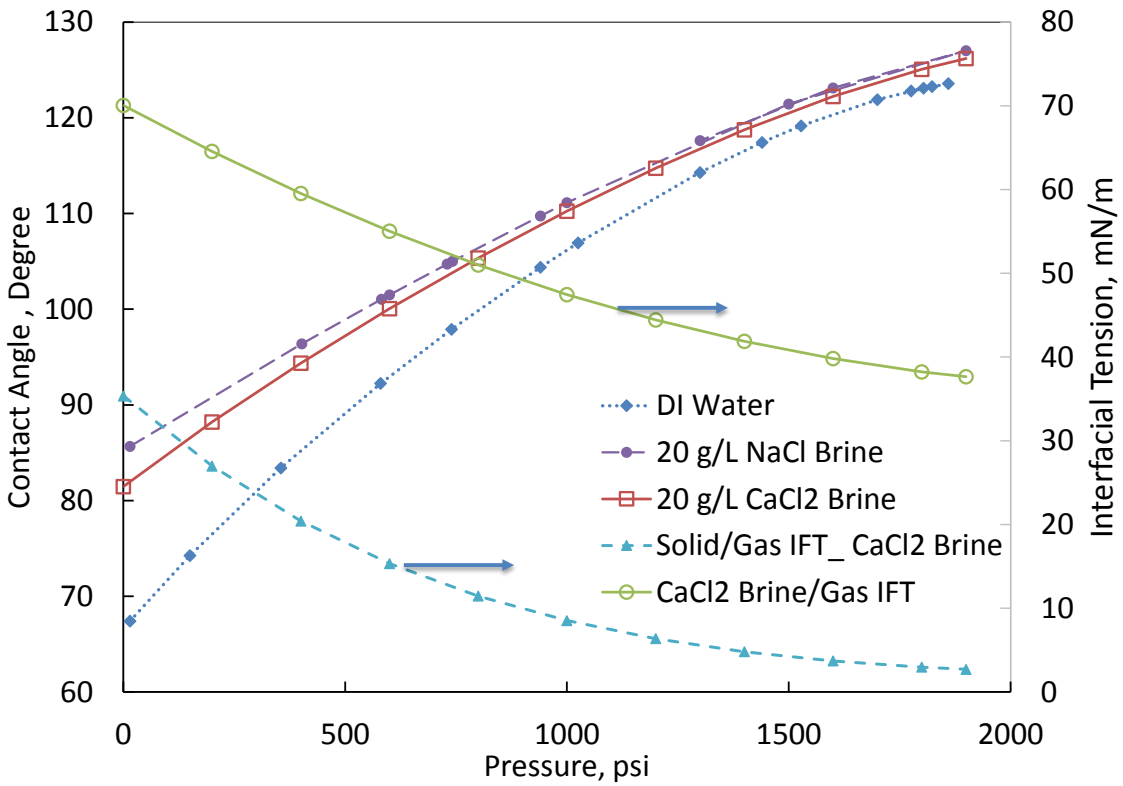


**Fig. 4-16 The estimated contact angles in the case of $CaCl_2$ brine comparing to those for DI water and NaCl brine, $CaCl_2$ brine -$CO_2$ interfacial tension after Aggelopoulos et al.,[37,38] and the estimated $\gamma_{SG}$ as a function of pressure.**

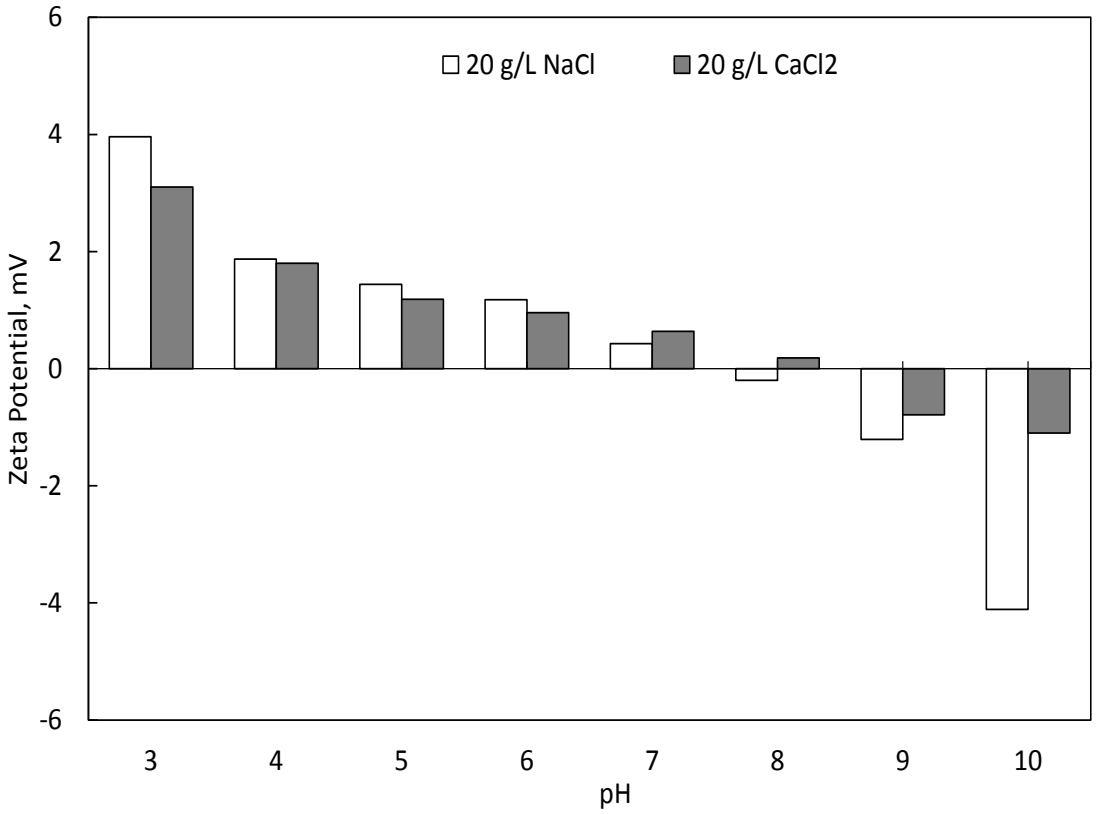


**Fig. 4-17 Zeta potential of coal particles (75 μm) in $CaCl_2$ brine compared to NaCl brine as a function of pH.**

To examine the effect of temperature on the contact angle measurements, contact-angle experiments were conducted at different temperatures in case of DI water. **Fig. 4-18** shows the effect of temperature on the contact-angle values. As the temperature increased, the contact angle decreased. Similar behavior was found by Arif et al.(Arif et al. 2016) As the temperature increased, the $CO_2$ adsorption to the coal surface decreased.[25] As a result, the gas interfacial tension to the solid increased,(Espinoza and Santamarina 2010) which decreased the contact angle with temperature.

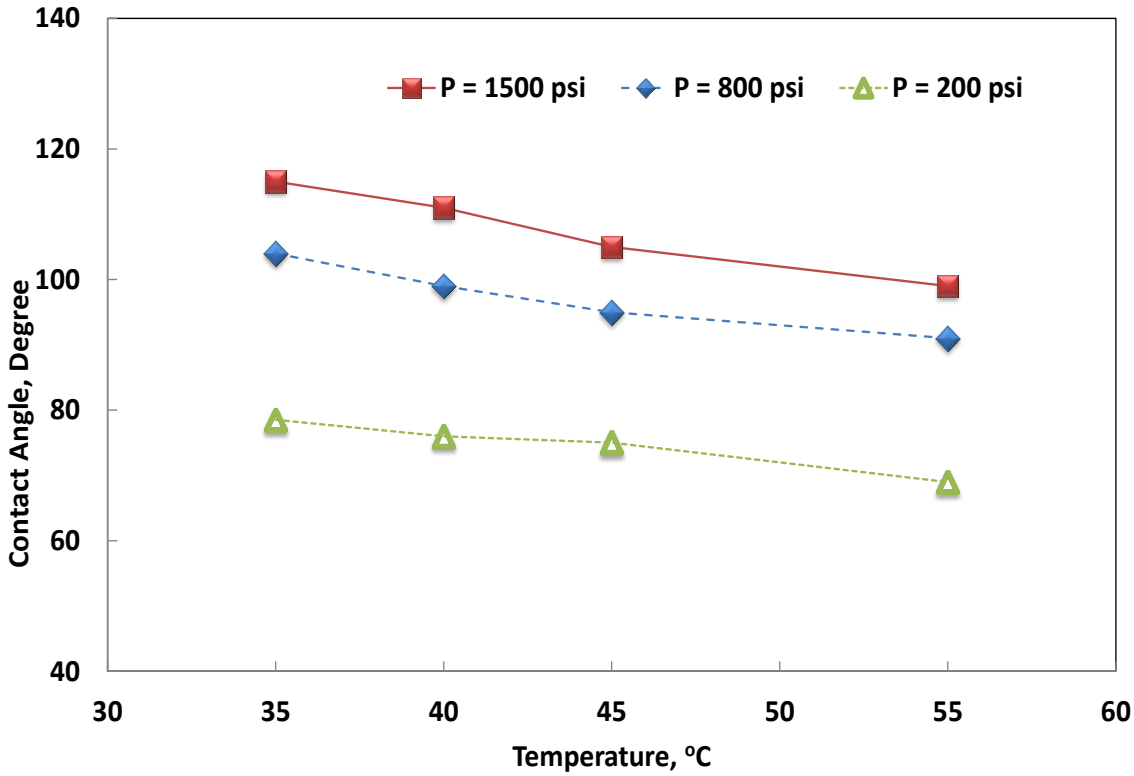


**Fig. 4-18 The contact-angle measurements as a function of temperature.**

The effect of the presence of other gasses in the system on the wettability of the coal surface was examined by measuring the contact angle in the case of DI water at different $N_2$ concentrations. **Fig. 4-19** shows the contact angle measurements as a function of nitrogen concentration. The contact-angle values decreased as nitrogen concentration increased, and the corresponding slope increased with pressure. This is in an agreement with the results by Shojai et al.(Shojai Kaveh et al. 2011; Shojai Kaveh et al. 2012) At 100% $N_2$, the coal remained water-wet, even at high pressures (contact angle was 75 at 1500 psi). These changes occur because of the $N_2$ adsorption rate and capacity of the coal surface being lower than that of $CO_2$.[25] Moreover, Chow et al.[36] show that the gas/liquid interfacial tension increased as nitrogen concentration increased in the gas phase, which contributed to the reduction in the contact-angle values.

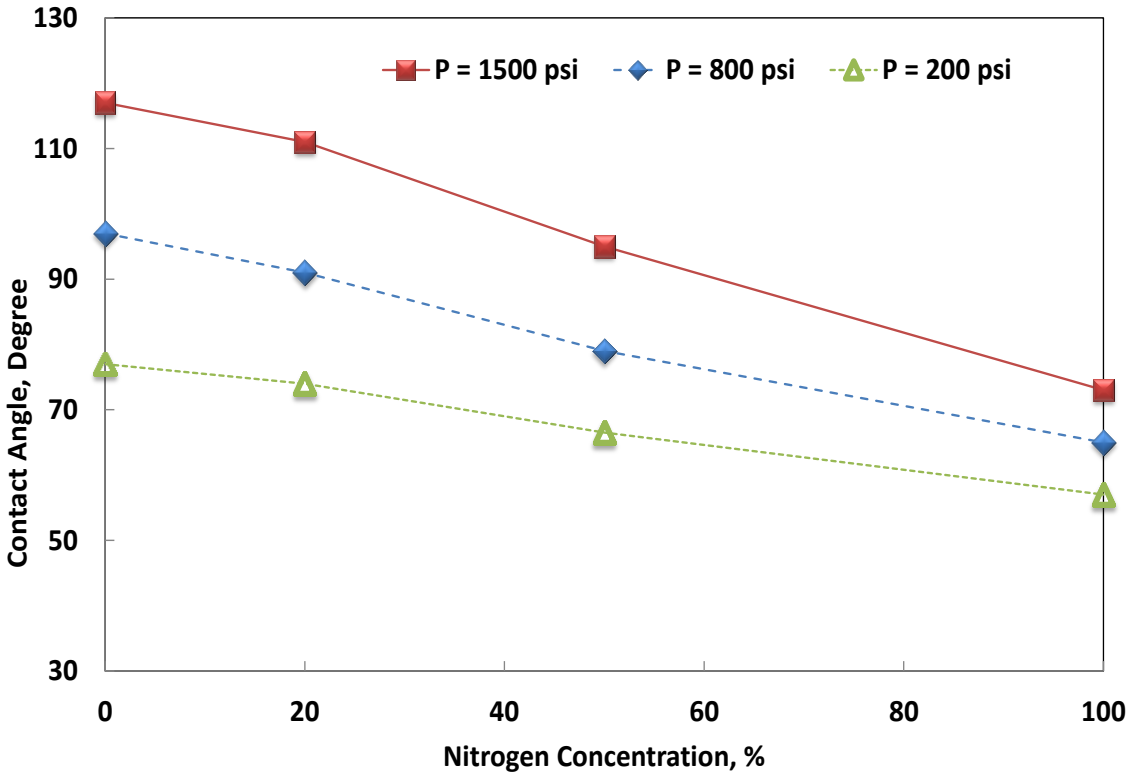


**Fig. 4-19 The contact-angle measurements as a function of nitrogen concentration of the injected gas.**

To review the application of $CO_2$ sequestration in coal formations, $CO_2$ can be stored in coal via three ways: free gas within the pore space or fractures in the coal, adsorbed molecules on the organic surface of the coal, and dissolved in groundwater within the coal. Based on these results, the storage capacity of $CO_2$ in coal increased as the formation water salinity increased as a free gas (where the displacement efficiency increases as the coal becomes more $CO_2$-wet). Furthermore, the capacity of the coal to store $CO_2$ as an adsorbed phase increases, due to the $CO_2$ adsorption isotherm increase. For example, at 1000 psi, the $CO_2$ storage as an adsorbed phase is 1141 scf/ton (0.028 scf/ft$^2$ of coal surface area) at 20 g/L NaCl, compared to 940 scf/ton (0.023 scf/ft$^2$ of coal surface area) with DI water. Similar performance can be predicted as a function of formation pressure.

These results may also be helpful in hydraulic fracturing applications. As the coal becomes less water wet as the water salinity increases, the fluid flowback after the

hydraulic fracturing operation could improve by using high-salinity water in the hydraulic fracturing, but more analysis is needed for this application.

# CHAPTER V
# COREFLOOD STUDY
# CARBON DIOXIDE SEQUESTRATION IN UNMINEABLE COAL FORMATIONS[4]

The objective of this study is to examine the effects of the salinity (NaCl) of coal seam water, injected gas composition, injection flow rate, and $CO_2$ gas state (formation pressure) on the $CO_2$ sequestration in volatile bitumen coal.

## 5.1. Experimental Studies

### Materials

A $CO_2$ cylinder with purity greater than 99.99 mol% was used. NaCl salt (ACS grade) was added to deionized (DI) water with a resistivity of 18.2 mΩ.cm at room temperature to prepare the brine with the required salt concentration. The brine densities and viscosities were measured using a pycnometer and capillary viscometer respectively (**Table 5-1**). Bitumen coal blocks were obtained from the Bull Hill mine in Oklahoma. **Tables 5-2 and 5-3** give the EDS mineral composition the proximate analysis using the thermogravimetric technique (Standard 2013) for the coal sample.

| NaCl Concentration, g/L | DI | 10 | 20 |
|---|---|---|---|
| Density, g/cm$^3$ | 0.997 | 1.005 | 1.012 |
| (computed tomography) CT number | 0 | 18 | 35 |
| Viscosity, cP | 0.996 | 1.02 | 1.036 |

Table 5-1 Density and CT number as a function of NaCl concentrations at 25°C.

[4] Reprinted with permission from "Effects of Formation-Water Salinity, Formation Pressure, Gas Composition, and Gas-Flow Rate on Carbon Dioxide Sequestration in Coal Formations" by Ibrahim, A. F., Nasr-El-Din, H. A. 2017. SPE J. Preprint, Copyright 2017 by Society of Petroleum Engineers.

| Element | C | O | Al | Si | S | Ca | Fe |
|---|---|---|---|---|---|---|---|
| Concentration, wt% | 82 | 10 | 0.8 | 0.44 | 2.53 | 0.25 | 2.23 |

Table 5-2 Composition of the coal used in the present study from EDS analysis.

| Component | Moisture | Volatile Mater | Fixed Carbon | Ash |
|---|---|---|---|---|
| Concentration, wt% | 0.2 | 47 | 50.8 | 2 |

Table 5-3 Proximate analysis for the coal sample using the thermogravimetric technique.

**Core Preparation**

Cylindrical coal cores were drilled to 6 in. length and 1.5 in. diameter. A heat-shrinkable Teflon liner was used to laminate the core to avoid breaking and prevent $CO_2$ diffusion through the rubber sleeve to the overburden oil. The cores were dried in an oven for two hours at 180°F, and then the dry core weight was measured. The cores were saturated under vacuum with NaCl brine, and then the weight of the saturated cores was measured. The pore volume was calculated from the brine density and weight difference in both the dry and saturated cases. The cores were stored in the NaCl brine until it was time to run the experiment to avoid exposing the coal to air and oxidizing.

**CT-Scan Analysis**

X-ray computed tomography (CT) has emerged as a powerful tool for non-destructive imaging due to its simplicity and high-resolution images (Taud et al. 2005). When a CT scan is operated, the X-ray source rotates around the object, and the transmitted X-ray intensity is recorded by a series of detectors. The recorded data is converted into numerical values or CT numbers. CT numbers are represented in Hounsfield units. A Hounsfield unit represents a relative change in the attenuation density. The scale is set so that air has a value of -1000, DI water is zero, and compacted bone is 1000. Three different sample tubes were filled with the required brines and scanned in order to obtain the CT number of each brine (Table 5-1).

By repeating the experiment twice, once dry (air-saturated) and the other brine-saturated, a difference in the recorded CT number will arise from the difference between both the brine and air density. This difference is proportional to the volume occupied by either fluid, and an estimation of the porosity can be calculated using Eq. 5-1 (Akin and Kovscek 2003).

$$\emptyset = \frac{CT_{sat} - CT_{dry}}{CT_{brine} - CT_{air}} \qquad \textbf{5-1}$$

where $\emptyset$ is the core porosity, $CT_{sat}$ and $CT_{dry}$ are the CT numbers of the coal core in brine saturated and dry cases, respectively, and $CT_{brine}$ and $CT_{air}$ are the CT numbers of the brine and air, respectively.

The coal cores were scanned to estimate the porosity profile along the core (**Fig. 5-1)**.

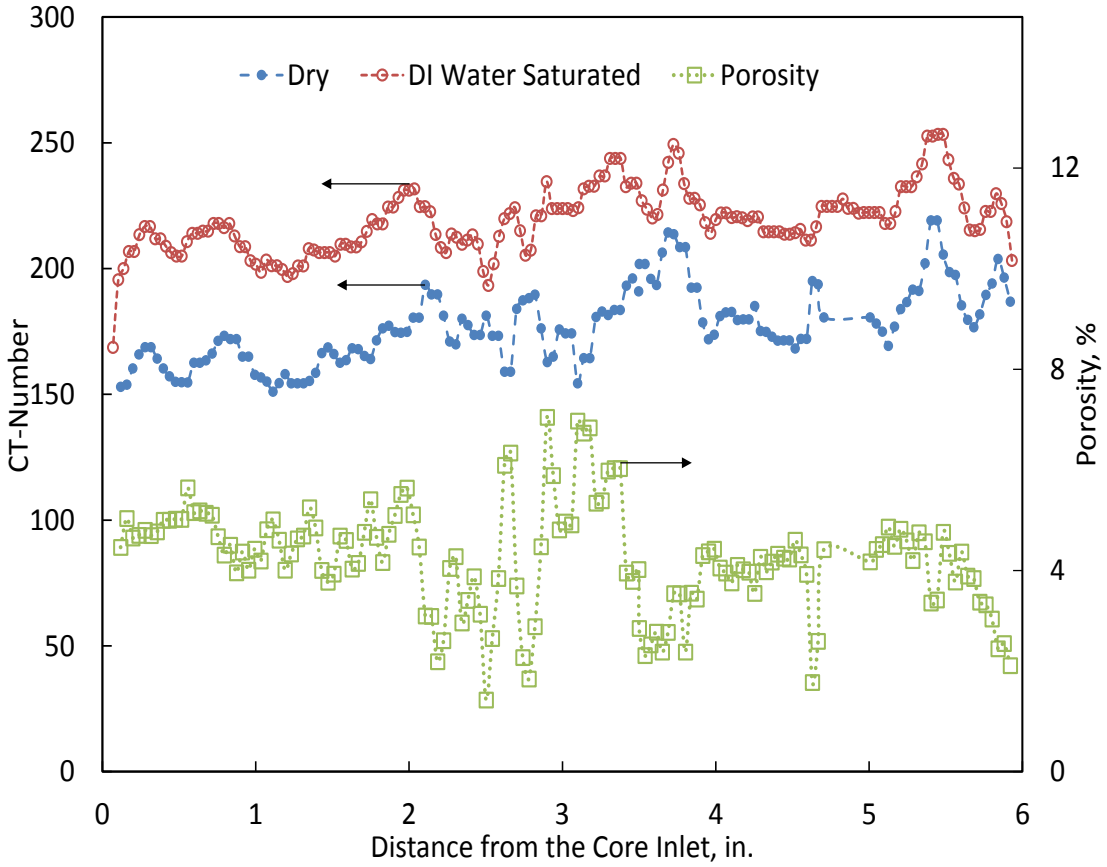


**Fig. 5-1 CT scans for the coal core in dried and DI water-saturated cases (Core 1).**

## Coreflood Setup

**Fig. 5-2** shows a schematic diagram for the setup used for the coreflood tests. Two stainless steel piston accumulators with a capacity of two liters were used to store the synthetic brine and the $CO_2$. A syringe pump model ISCO 1000D™ was used to displace the fluids from the piston accumulators. Swagelok™ valves model SS-41S21 were installed at the accumulators' outlet to control the fluids alternating during the injection. To monitor the pressure at the core inlet, a pressure gauge was installed at the coreholder inlet. A Phoenix Instruments® hassler type core holder was used to hold the core during the coreflood test and it was set vertically. A Mity Mite® backpressure regulator (S91W) was installed at the core outlet to maintain the outlet pressure. It was adjusted by a nitrogen

cylinder. A Highly Saturated Nitrile (HSN)$^{TM}$ rubber sleeve was used to resist $CO_2$ diffusion into overburden fluids. An Enerpac P-392$^{®}$ hand pump was used to apply overburden pressure around the core. The overburden pressure was kept at 200 psi higher than the core inlet pressure. A pressure transducer was used to measure the pressure drop across the core and sent through a data acquisition system to a computer that records the data through LabVIEW$^{TM}$ software.

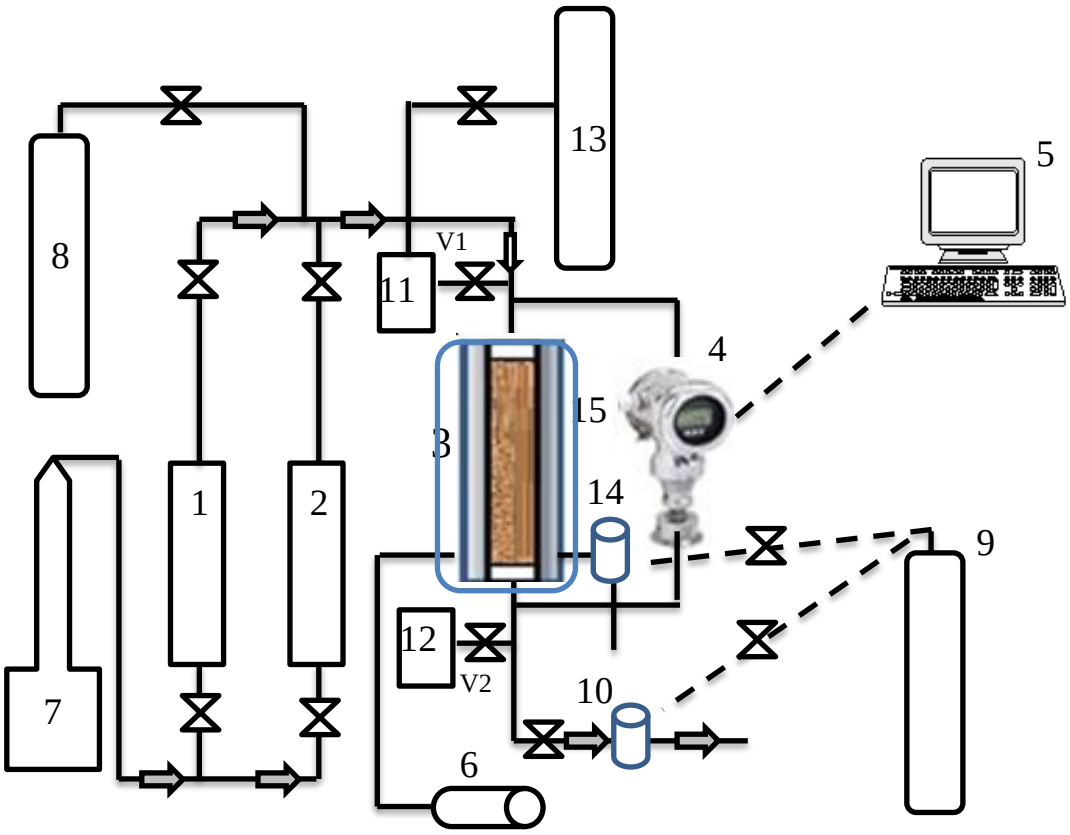


**Fig. 5-2 Schematic for coreflood setup. 1 = Water accumulator, 2 = CO2 accumulator, 3 = Core Holder, 4 = Pressure Transducer, 5 = PC Recorder, 6 = hand pump for overburden pressure, 7 = syringe pump, 8 = CO2 cylinder, 9 = N2 cylinder, 10 = Back pressure regulator, 11, 12 = upstream and downstream volumes for pulse decay measurements that connected with valves V1 and V2, 13 = He cylinder, 14 = overburden pressure regulator, 15 = heating jacket.**

**Experimental Procedure**

The coreflood tests were designed to simulate the injection of $CO_2$ into coal formations. A slug of synthetic brine was injected into the coal cores to measure the initial absolute core permeability, followed by a slug of $CO_2$. Finally, a slug of the same brine was used to displace the $CO_2$ and measure the final effective water permeability. Tests were run at room temperature. **Table 5-4** gives the conditions for the different coreflood experiments. A base case was conducted by injecting 100% $CO_2$ gas at an injection rate of 1 $cm^3$/min, 1100 psi back pressure, and DI water. Then, one parameter was changed to examine its effect on the $CO_2$ sequestration performance.

The core was placed inside the coreholder, and brine was injected at the required flowrate. The pressure drop across the core was monitored, and the stabilization pressure was used to calculate the permeability, using Darcy's equation for linear and laminar flow. $CO_2$ was injected at a constant rate (same as brine injection flow rate) until the pressure drop across the core stabilized and no more water was coming out of the core. Displaced water volume was monitored to estimate the residual water saturation. Then, the same brine was injected to displace the gas out of the core, and the pressure drop across the core was monitored until stabilization and no gas bubbles were observed at the outlet.

| Core # | Weight porosity, fraction | CT porosity, fraction | Initial absolute water permeability, md | NaCl concentration, g/L | Back pressure, psi | Injection flow rate, $cm^3$/min | Injected gas | Case |
|---|---|---|---|---|---|---|---|---|
| **1** | 0.04 | 0.038 | 2.5 | 0 (DI water) | 1100 | 1 | $CO_2$ | Base case |
| **2** | 0.053 | 0.05 | 7.5 | 10 | 1100 | 1 | $CO_2$ | Examine water salinity effect |
| **3** | 0.045 | 0.042 | 5.8 | 20 | 1100 | 1 | $CO_2$ | |
| **4** | 0.039 | 0.035 | 3.8 | 0 (DI water) | 300 | 1 | $CO_2$ | Examine back pressure effect |
| **5** | 0.043 | 0.0/4 | 7.5 | 0 (DI water) | 50 | 1 | $CO_2$ | |
| **6** | 0.04 | 0.039 | 6.7 | 0 (DI water) | 1100 | 2 | $CO_2$ | injection rate effect |
| **7** | 0.04 | 0.041 | 6 | 0 (DI water) | 1100 | 4 | $CO_2$ | |
| **8** | 0.052 | 0.048 | 10 | 0 (DI water) | 300 | 1 | 50% $N_2$, 50% $CO_2$ | Examine Gas Composition |
| **9** | 0.058 | 0.054 | 8 | 0 (DI water) | 300 | 1 | $N_2$ | |

**Table 5-4 Properties of coal cores and the coreflood experimental conditions.**

## 5.2. Results and Discussion: Experimental

Table 5-4 gives the properties of coal cores used and the experimental conditions. All cores were cut from the same coal block, and the initial permeability varied between 3 and 10.

A general trend for the pressure drop (DP) across the core was found in the coreflood experiments (**Fig. 5-3)**. In the first stage, DP increased gradually until stabilization (the absolute permeability can be calculated). Once the $CO_2$ was injected (the second stage), the pressure dropped suddenly due to low $CO_2$ viscosity compared to brine viscosity (Meehan 1980; Fenghour and Wakeham 1997). The $CO_2$ displaced the brine from the core; while increasing the $CO_2$ saturation inside the core, the pressure drop across the core continuously decreased. Once the water saturation reached the irreducible condition, where no more water was produced from the core, the pressure drop stabilized. In the third stage, the pressure drop increased suddenly, then decreased with time until stabilization. The pressure drop at the start of the third stage is usually higher than the stabilized pressure (DPs) of this stage, because of the two-phase flow at the beginning of the third stage and the reduction of the absolute core permeability.

The DPs during the third stage was always higher than that of the first stage. The increase in the stabilized pressure drop across the core ($\Delta DP_s$) for the experiments (equal to the decrease in the effective water permeability ($\Delta k_{rw}$)) was calculated as follows:

$$\Delta \boldsymbol{k_{rw}} = \Delta \boldsymbol{DP_s} = \frac{\boldsymbol{DP_{s3} - DP_{s1}}}{\boldsymbol{DP_{s3}}} \qquad 5\text{-}2$$

where $DPs_1$, and $DPs_3$ are the stabilized pressure drop across the core during the first and third stages, respectively. The ΔDPs was always positive because the reduction of the effective water permeability during the third stage compared to the first stage. In the first stage, the core was 100% saturated with water, and the effective water permeability was equal to the initial absolute core permeability, where the relative water permeability equals 1. The effective water permeability in the third stage is a function of that at the residual gas saturation and the final absolute core permeability, as follows:

$$\mathbf{k_w = k \times k_{rw}(s_{gr})} \quad 5\text{-}3$$

where k is the absolute core permeability after gas injection, and $k_{rw}(S_{gr})$ is the relative water permeability at the residual gas saturation ($S_{gr}$).

The Darcy equation for water in linear steady-state flow can be described as follows:

$$\mathbf{Q_w = \frac{k_w A\ DPs}{\mu_w L}} \quad 5\text{-}4$$

where $k_w$ is the effective water saturation, A is a cross-section area, L is the core length, and $\mu_w$ is the water viscosity. As $\mu_w$, $Q_w$, A, and L are constants, the change in the stabilized pressure drop will be an indicator of the change in the effective water permeability. The reduction in effective water permeability may be due to reduction in relative water permeability (Anderson 1987), or the reduction in the core absolute permeability. The absolute coal permeability decreased due to matrix swelling when the coal was exposed to carbon dioxide (Palmer 2009; Battistutta et al. 2010; Liu and Harpalani 2013). Hence, the increase in the stabilized pressure drop was used as an indicator for the effect of the studied parameters on the $CO_2$ sequestration performance.

**Effect of Back Pressure.** To examine the effect of pressure and $CO_2$ state on the $CO_2$ sequestration process, three coreflood experiments were conducted at different back pressures. $CO_2$ was examined as a gas phase with back pressures of 50 and 300 psi, and as a supercritical fluid with the back pressure of 1100 psi. Fig. 5-3 shows the pressure drop across the core for three coreflood experiments as a function of back pressure. DI water was injected in the first and third stage. In the second stage, 15 pore volumes of $CO_2$ were injected during the three experiments at the same rate (1 $cm^3$/min) to ensure the same contact time between the $CO_2$ and the coal. The pressure drop in the second stage increased as the back pressure increased. Two factors account for the pressure-drop increases. First,

the $CO_2$ viscosity increased from 0.014 cp at 50 psi to 0.075 cp at 1100 psi (Meehan 1980; Fenghour and Wakeham 1997). Second, $CO_2$ adsorption increased at high formation pressure. As a result, matrix swelling became higher (Battistutta et al. 2010).

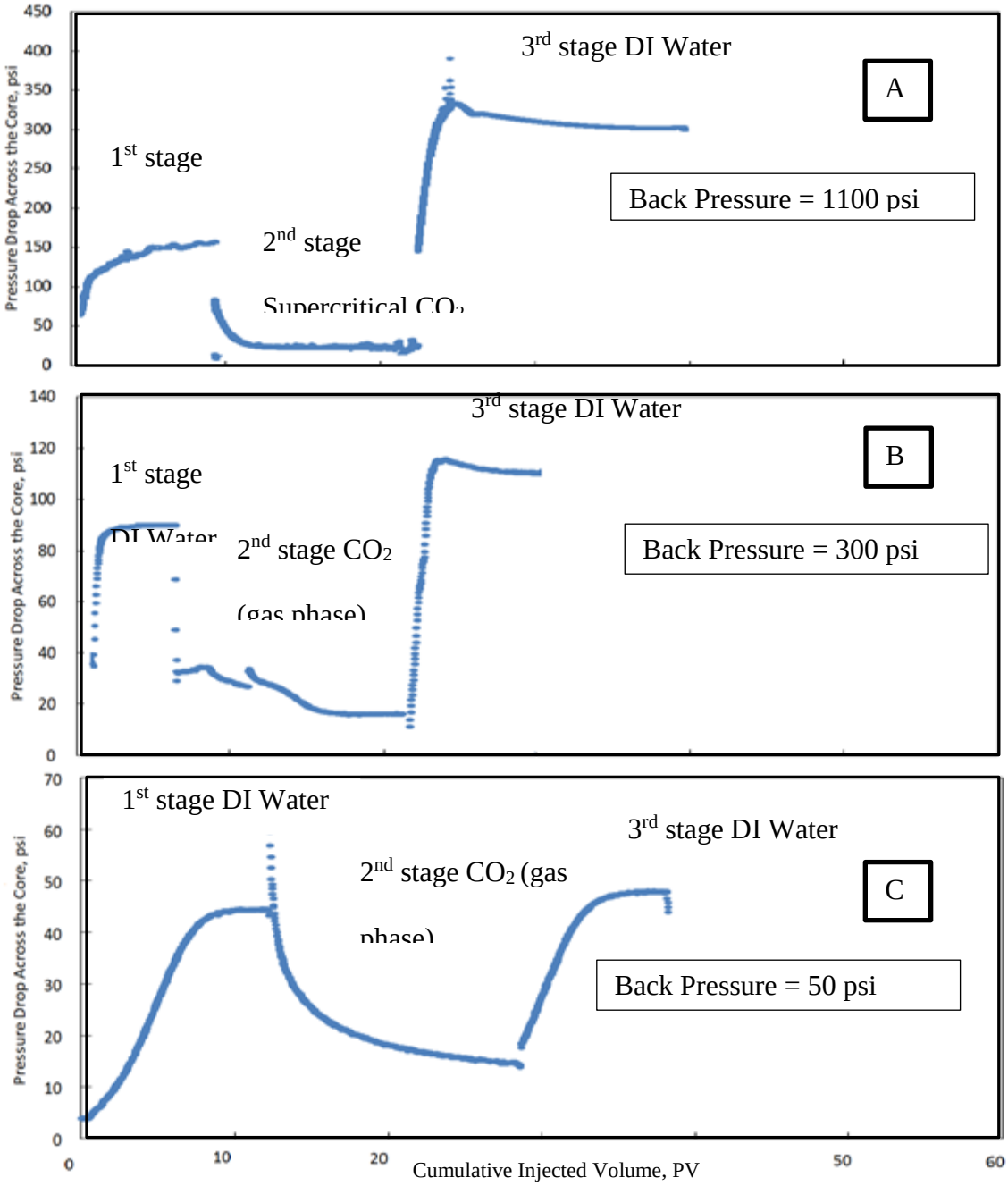


**Fig. 5-3 The pressure drop across the core for three coreflood experiments as a function of back pressure with injection rate 1 cm$^3$/min. A: Back pressure = 1100 psi, B: Back pressure = 300 psi, and C: Back pressure = 50 psi**

**Fig. 5-4A** shows ΔDPs ($\Delta k_{rw}$) (calculated from Eq. 5-2) as a function of back pressure. It shows that the higher the back pressure, the higher the ΔDPs ($\Delta k_{rw}$). The effective water permeability decreased by 8% at 50 psi back pressure, compared to 48% at 1100 psi. Two factors account for the increase of ΔDPs with back pressure. First, as the pressure increased, the coal became $CO_2$ wet (Shojai Kaveh et al. 2012). As a result, the residual $CO_2$ saturation increased and the relative water permeability decreased. Hence, the effective water permeability decreased and the pressure drop increased. Second, as the pressure increased, the $CO_2$ adsorption in coal surface increased (Busch et al. 2003) and matrix swelling increased. As a result, the absolute coal permeability decreased and the pressure drop increased. Consequently, the capacity of the coal to store $CO_2$ as adsorbed phase increased at high pressure, but the gas injectivity will be lower.

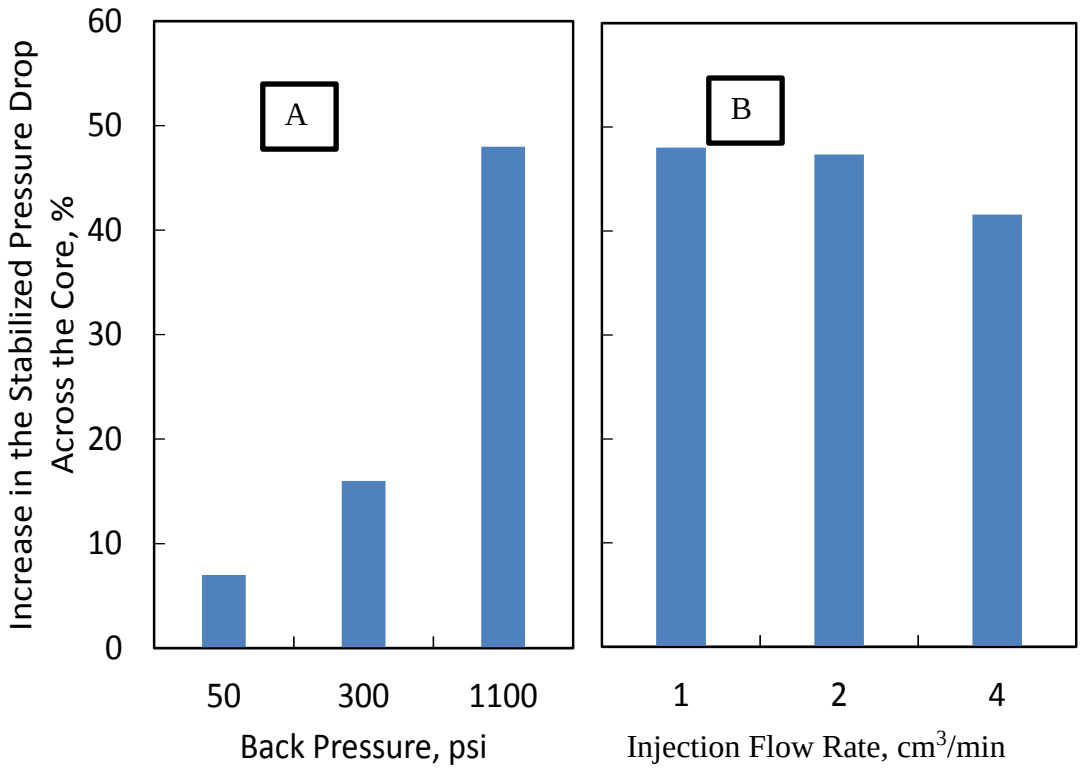


**Fig. 5-4 The increase in the stabilized pressure drop across the core (the decrease in the effective water permeability). A: as a function of back pressure at injection rate 1 $cm^3$/min, and B: as a function of injection flow rate at 1100 psi with DI water.**

**Effect of Injection Flow Rate.** To examine the effect of injection flow rate on the $CO_2$ sequestration in coal, three coreflood experiments were conducted at 1, 2, and 4 $cm^3$/min at the same $CO_2$ injection volume at a back pressure of 1100 psi. **Fig. 5-5** shows the pressure drop across the core at different injection flow rates. Fig. 5-4B shows the increase of ΔDPs as a function of injection flow rate. The plotted data shows that, as the injection flow rate increased, the ΔDPs slightly decreased. The effective water permeability decreased by 41% at 4 $cm^3$/min, compared to 48% at 1 $cm^3$/min. As the injection flow rate increased, the contact time of $CO_2$ to the coal surface decreased. Hence, the $CO_2$ adsorption to the coal matrix decreased (Vishal et al. 2015). As a result, the change in ΔDPs decreased.

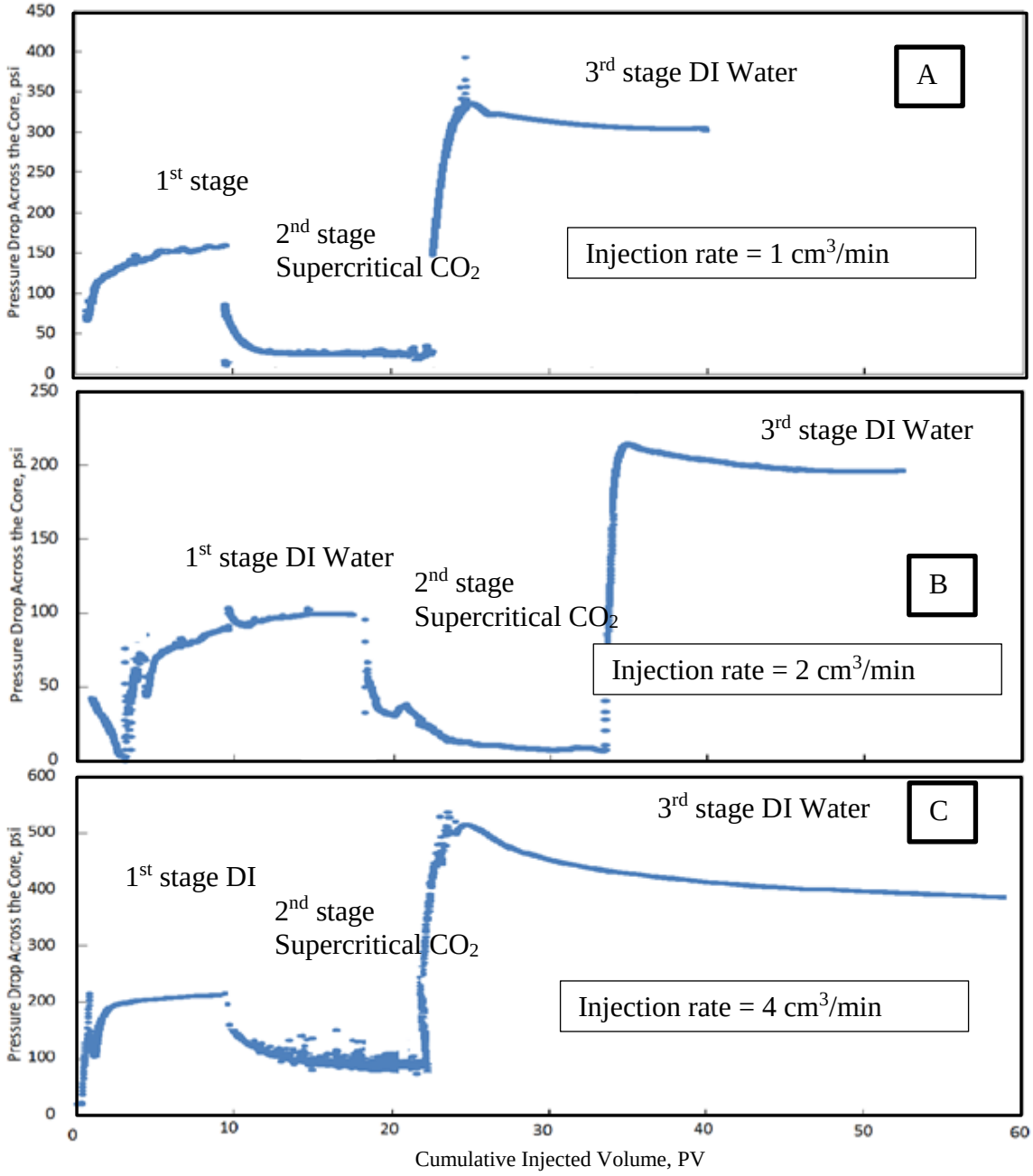


**Fig. 5-5 The pressure drop across the core as a function of the injection flow rate at a back pressure of 1100 psi. A: Injection rate = 1 $cm^3$/min, B: Injection rate = 2 $cm^3$/min, and C: Injection rate = 4 $cm^3$/min.**

**Effect of Injected Gas Composition.** To examine the effect of gas composition, three different cores were saturated with DI water. Gas streams with different gas compositions (100% $CO_2$, 50/50 $N_2/CO_2$, 100% $N_2$) were injected into these cores. **Fig. 5-6** shows the

residual water saturation at the end of gas injection and is a reflection of the displacement efficiency. As the $N_2$ concentration increased in the gas stream, the residual water saturation increased, and the reduction in core permeability decreased. Concurrently, the gas adsorption to the coal surface decreased, and the coal became more water-wet (as in chapter 4). As a result, the relative permeability to gas was higher (Anderson 1987) that lead to a gas breakthrough and lower water displacement efficiency. The residual water saturation increased to 50% in the case of pure $N_2$. Fig. 5-6 shows that the as the $N_2$ concentration increased in the injected gas the increasing of the $DP_s$ decreased, which is a result of reduction gas adsorption and coal hydrophobicity. These results were in agreement with results proposed by Mazumder et al. (2008). These researchers found that flue gas experiments had lower sweep efficiency compared to the $CO_2$ flooding experiments as a result of lower $N_2$ adsorption to coal surface compared to $CO_2$.

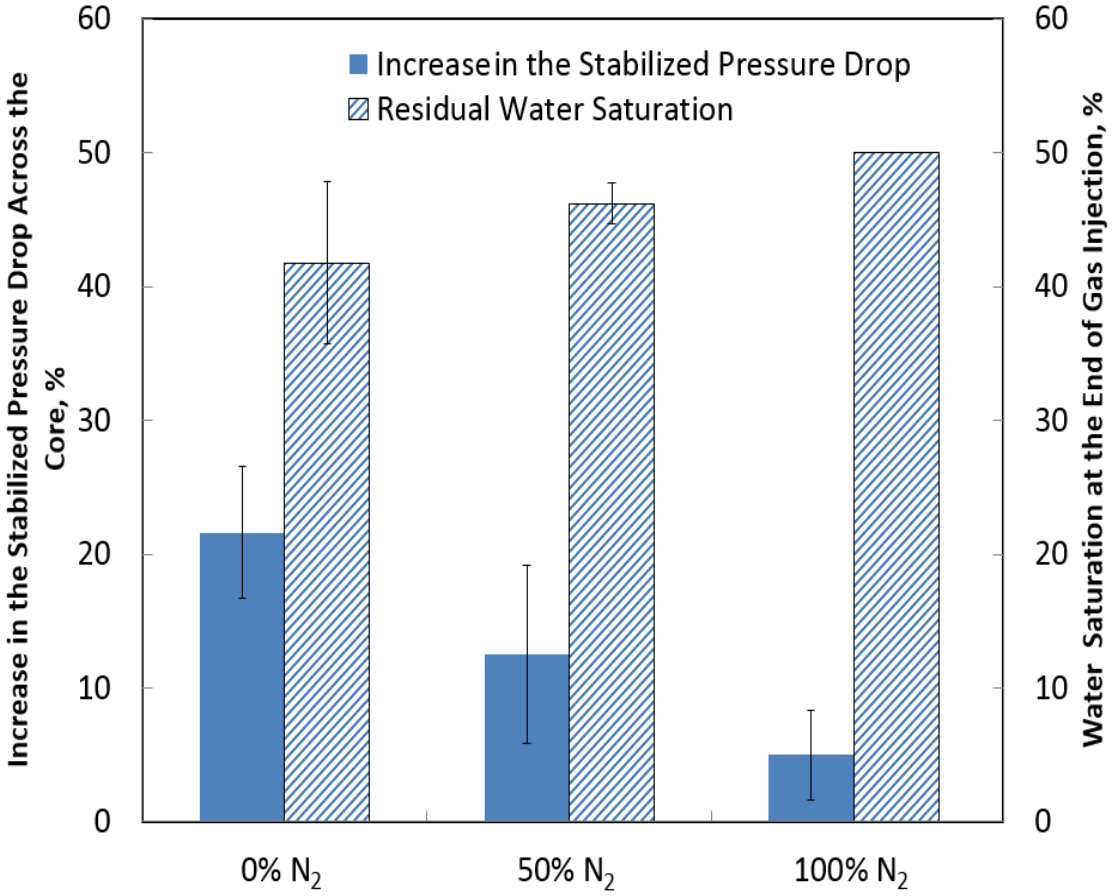


**Fig. 5-6 Increase in the stabilized pressure drop across the core (the decrease in the effective water permeability) and residual water saturation as a function of $N_2$ concentration in the injected gasses.**

**Effect of Formation Water Salinity.** To examine the effect of water salinity, six coreflood experiments were conducted at different NaCl concentrations (0-20 g/L). Two sets of experiments were run, one at 300 psi back pressure, and another set at 1100 psi. **Fig. 5-7** shows the increase of ΔDPs as a function of NaCl concentration. As salt concentration increased, the ΔDPs slightly increased. The results from chapter 4 showed that the $CO_2$ adsorption increased as water salinity increased. Consequently, the change in the absolute permeability increased with the water salinity increase. As a result, the effective water permeability decreased and the ΔDPs increased. The coal became more hydrophobic as the salinity increased. Hence, the coal became more gas-wet, the gas filled the small coal pores, and the residual gas saturation increased. As a result, the relative

water permeability decreased, which decreased the effective water permeability and increased the ΔDPs. However, as the pressure increased, the effect of salinity on coal wettability decreased, and the contact angle values at (15 g/L NaCl brine) converged to the DI water case. As a result, the pressure effect is more dominant than the salinity effect on the ΔDPs.

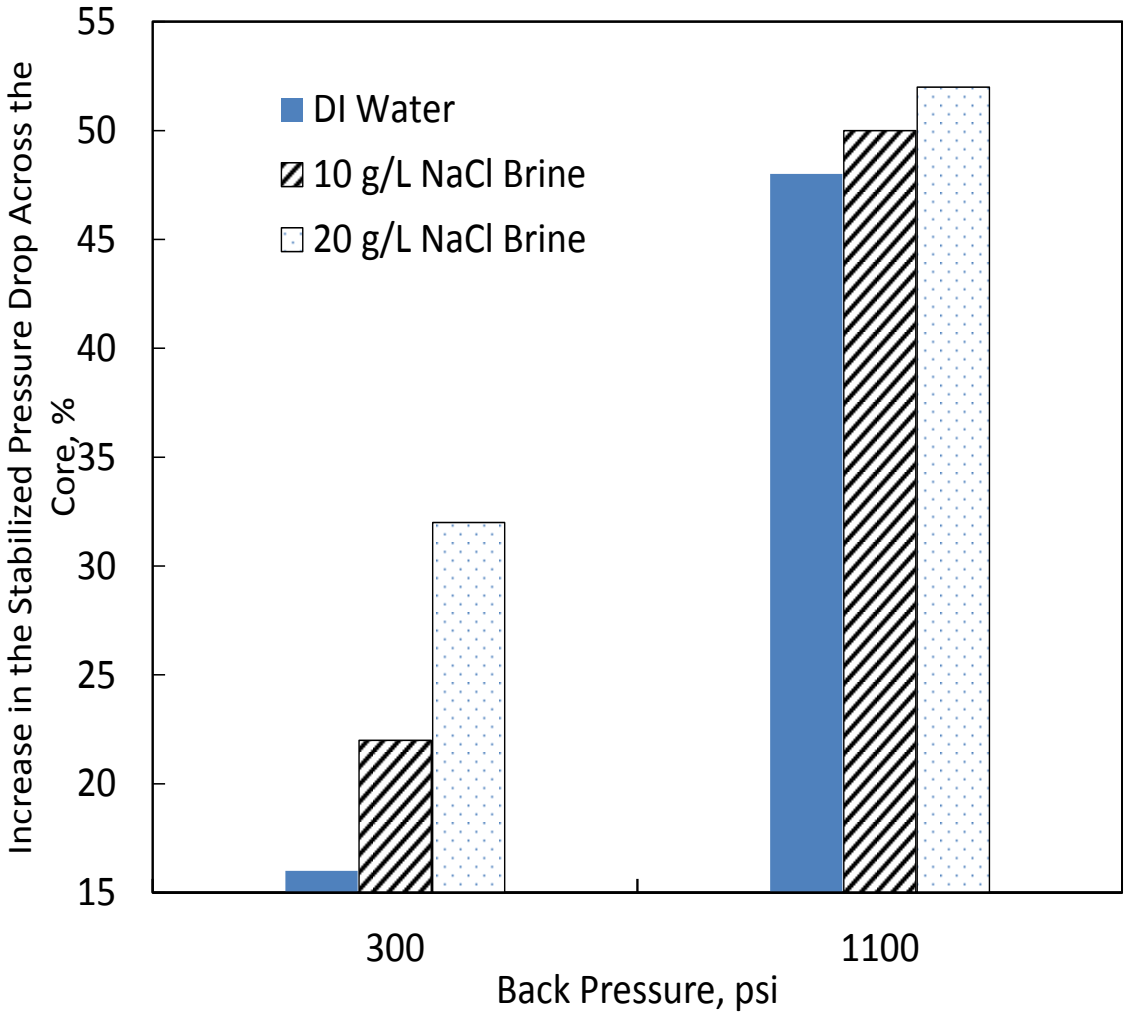


**Fig. 5-7 The increase in the stabilized pressure drop across the core as a function of NaCl concentration at 300 and 1100 psi and 1 $cm^3$/min.**

## 5.3. Permeability Dynamics

This section discusses the change in the absolute coal permeability that was measured as a function of injection pressure. A dry core was used in these measurements to exclude the effect of a change in relative permeability. Initially, a pulse decay method was employed to measure the core permeability using helium (Feng et al. 2016). **Fig. 5-8a** shows the pressure drop between the upstream and downstream. The pressure drop initially decreased rapidly, then stabilized at a residual pressure difference ($Pc_{,residual}$). This residual pressure is due to the capillary effects and is dominated by the wettability of the coal surface and the pore structure (Han et al. 2010). Pulse decay measurements were repeated three times at different average pressures and, Fig. 5-8b shows the semi-log analysis for the three pulses. The Klinkenberg effect was excluded by plotting the permeability against (1/average flow pressure), and the corrected permeability value is the intercept with the y-axis. The residual pressure difference during these pulse-decay measurements was equal at the same back pressure. $CO_2$ was injected at a constant pressure, and the injection flow rate was allowed to change. As the injection pressure was constant, the change in the injection flow rate is a reflection of the injectivity behavior (injectivity index = injection flow rate/ (injection pressure-back pressure)). **Fig. 5-9** shows the injectivity reduction during $CO_2$ injection at back pressure 400 psi. Initially, the injectivity index remained constant, but then continuously decreased with $CO_2$ injection and then stabilized at 40% of its initial value. Injectivity index reduction is due to coal swelling that decreases the coal permeability. Once the coal surface saturated with the adsorbed $CO_2$ and the system reached equilibrium condition at this pressure, the coal permeability remains constant and the injectivity stabilizes. The pulse-decay method (using helium) was then used to measure the core permeability at this condition while maintaining an average pressure higher than the back pressure during the $CO_2$ injection stage to prevent $CO_2$ desorption from coal surface.

$CO_2$ injection followed by pulse-decay measurements were repeated at different back pressures up to 1100 psi (The overbalance pressure was kept 200 psi higher than the injection pressure to prevent fracture expansion due to increasing the injection pressure).

Similar injectivity behavior was found at each back pressure. **Fig. 5-10** shows the permeability change with back pressure. The permeability continuously decreased with the pressure to 0.2 of its initial value at back pressure = 1100 psi. Furthermore, the residual pressure difference increased which indicates a change in the pore structure due to $CO_2$ adsorption onto coal surface.

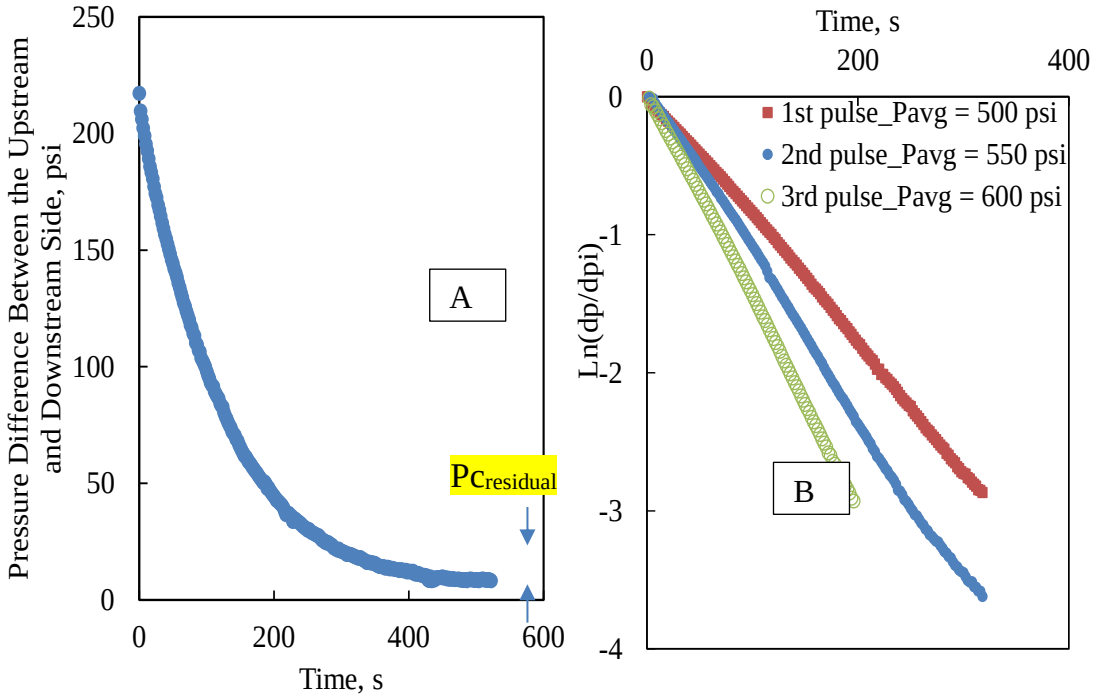


**Fig. 5-8 Pulse-decay permeability measurements at backpressure = 400 psi; A- Pressure drop between the core upstream and downstream, B-Semi-log analysis for the three pulses at average pressures 500, 550, and 600 psi.**

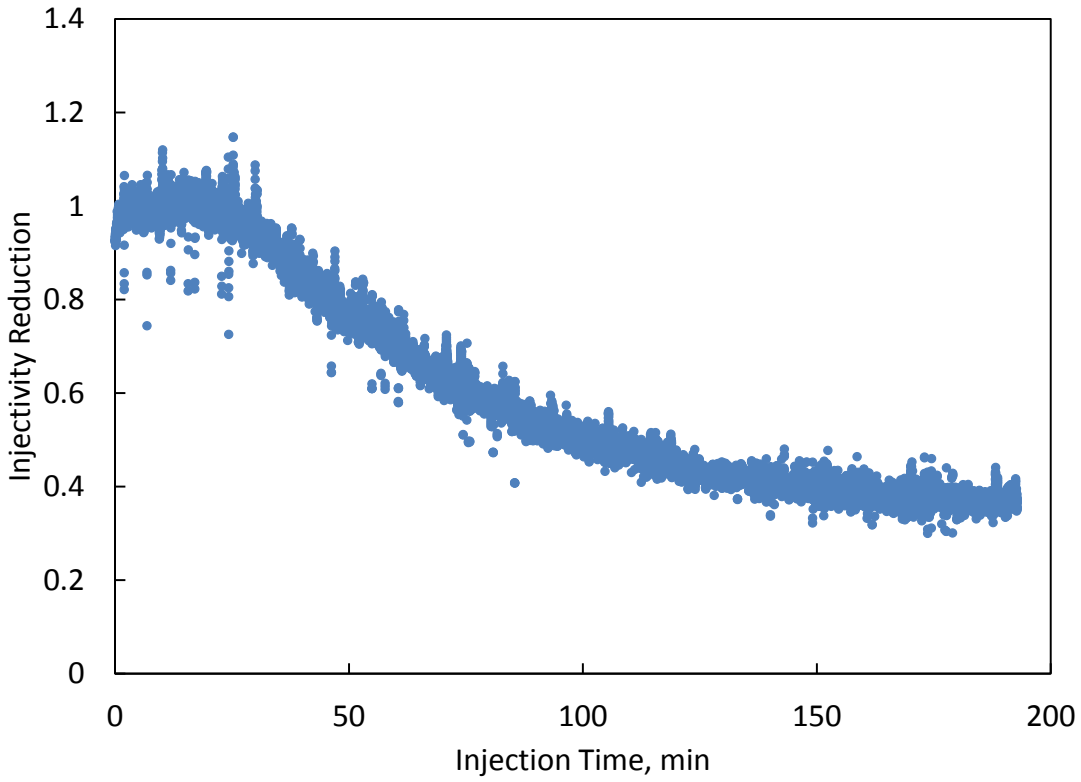


**Fig. 5-9 Injectivity reduction during $CO_2$ injection at a back pressure of 400 psi.**

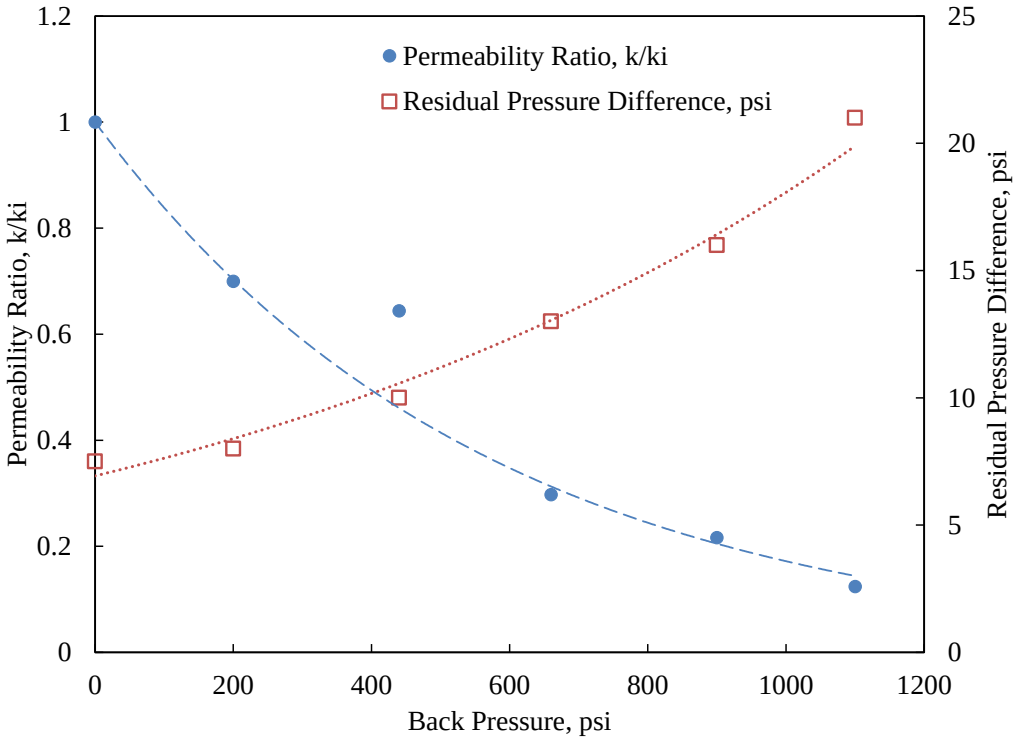


**Fig. 5-10 Permeability ratio and residual pressure difference (upstream pressure - downstream pressure) as a function of back pressure.**

## 5.4. Numerical Simulation

A simulation study was conducted to simulate and cross-validate the experiments in the core scale using a commercial simulator. This simulator was used to match the pressure drop across the core from the experimental data by adjusting the relative permeability curves. The water saturation, porosity, and permeability distribution along the core were estimated. A cylindrical core was divided into radial grid blocks with 3×1×18 blocks in the r, θ, and z directions, respectively (**Fig. 5-11**). Initial porosity and permeability were taken from the actual experimental measurements. The flow was assumed in the z direction from the inlet to the outlet. Two additional grids were added on the inlet and the outlet of the core with high permeability in the r, θ, and z directions to reflect the flow distributor for the core. **Table 5-5** presents the input parameters for the simulation study.

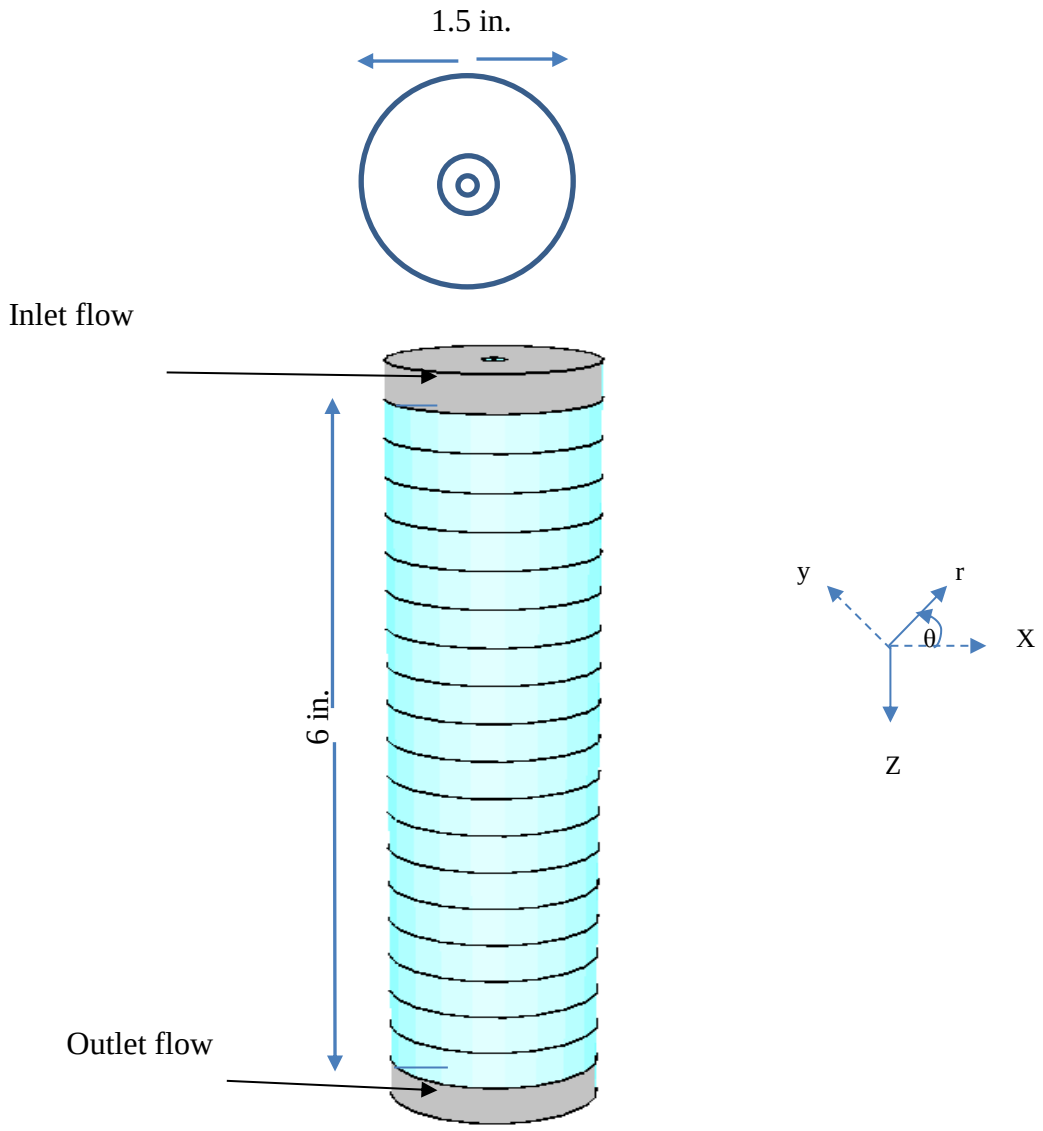


**Fig. 5-11 Schematic for the radial grid blocks with 3x1x18 blocks in the r, θ, and z directions, respectively, with two flow distributors.**

| Parameter | Value |
|---|---|
| Langmuir adsorption volume in DI water, scf/ton | 1329[a] |
| Langmuir adsorption pressure in DI water, psi | 414[a] |
| Langmuir adsorption volume in DI water, scf/ton | 1788[a] |
| Langmuir adsorption pressure in DI water, psi | 567[a] |
| dz, in. | 0.333 |
| $\theta$, degree | 360 |
| dr1,dr2,dr3, in. | 0.1, 0.2, 0.8 |
| Coal density, g/cm$^3$ | 1.25 |
| Young's modulus, psi | 3.8E5 |
| Poisson's ratio | 0.35 |
| Injection rate, cm$^3$/min | Table 5-4 |
| Production pressure, psi | = Back pressure, Table 5-4 |
| Initial water saturation, % | 100 |
| Porosity, % | Table 5-4 |
| Initial cores permeability, md | Table 3 |
| Initial formation pressure, psi | = Back pressure, Table 5-4 |

Table 5-5 Input parameters used in the simulation study.

As the coal formation is initially saturated with water, $CO_2$ (as a gas or a supercritical phases) injection into coal is a two-phase flow problem. Relative permeability is important for the calculations of pump power required for $CO_2$ injection, and $CO_2$ movement inside the reservoir. The gas and water relative permeabilities in the coalbed have a significant effect on the performance characteristics of the reservoir. Corey equations are used to determine gas and water relative permeabilities (Enoh 2007) as follows:

$$\mathbf{K_{rg} = K^{*}_{rg}\left(\frac{s_g - s_{gr}}{1 - s_{wc} - s_{gr}}\right)^{n}}, \text{ and} \qquad \mathbf{5\text{-}5}$$

$$\mathbf{K_{rw}} = \mathbf{K^{*}_{rw}}\left(\frac{\mathbf{s_w - s_{wc}}}{\mathbf{1 - s_{wc} - s_{gr}}}\right)^{\mathbf{m}}, \qquad 5\text{-}6$$

where $K_{rg}$ is the relative permeability to gas, $K^{*}_{rg}$ is the relative permeability to gas at critical water saturation, $\mathbf{s_{wc}}$ is critical water saturation, and m, n are Corey exponents. The history-matching technique can be used to determine Corey exponents (n, m). Connate water saturations and the end point relative permeabilities (effective permeability to water at the end of injection gas stage/absolute permeability) were obtained from the coreflood results.

## 5.5. Results and Discussion: Numerical Simulation

**Fig. 5-12A** shows the pressure drop match for the base case. Two cases were conducted, one case with matrix swelling effect considered and another one case without it. Even though the matrix swelling effect was neglected, the pressure drop across the core increased after $CO_2$ injection, as a result of the presence of residual gas in the core and the reduction in the relative water permeability. Furthermore, Fig. 11 also shows that when accounting for the matrix swelling effect, the absolute core permeability decreased and the ΔDPs increased. As the difference between the overburden pressure and the injection pressure was kept constant (200 psi), the fracture expansion due to increasing the injection pressure was neglected. **Fig. 5-12B** shows the same analysis for the 20 g/L NaCl brine case. Similar behavior to the base case was almost found, where the pressure effect is more dominant than the salt effect.

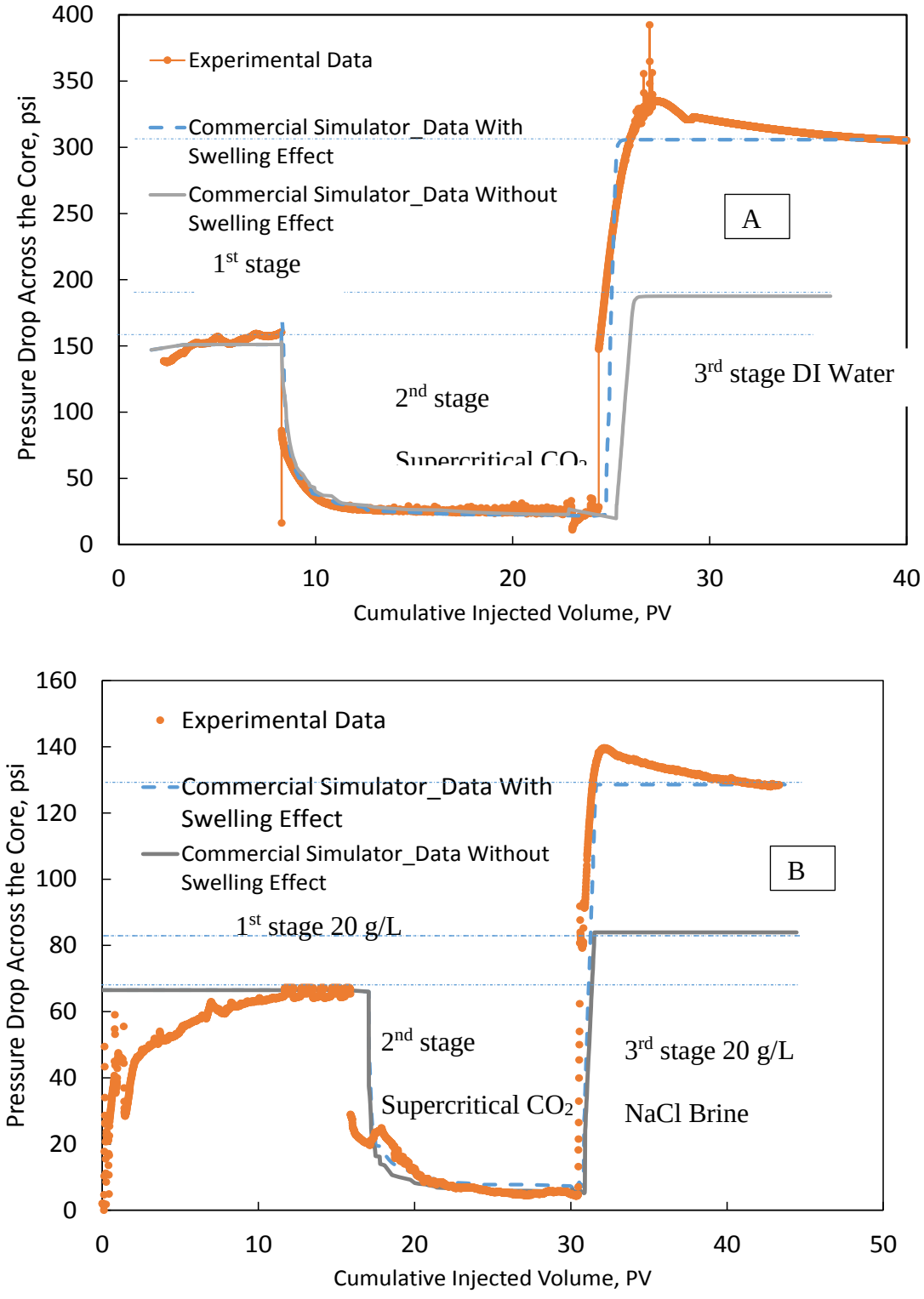


**Fig. 5-12 Matching the pressure drop across the core with a commercial simulator for (A) the base case, and (B) the 20 g/L NaCl brine case.**

**Fig. 5-13** shows the water saturation distribution along the core during the three injection stages. The core was initially saturated under vacuum with water ($S_w = 1$). As $CO_2$ was injected into the core, the gas displaced the water, and the water saturation decreased with time to the residual water saturation ($S_w = 0.4$). Finally, the water was injected (the third stage), and water saturation increased and displaced the gas from the core (residual gas saturation reached to around 0.1), in agreement with the result proposed by Ramurthy et al. (2003).

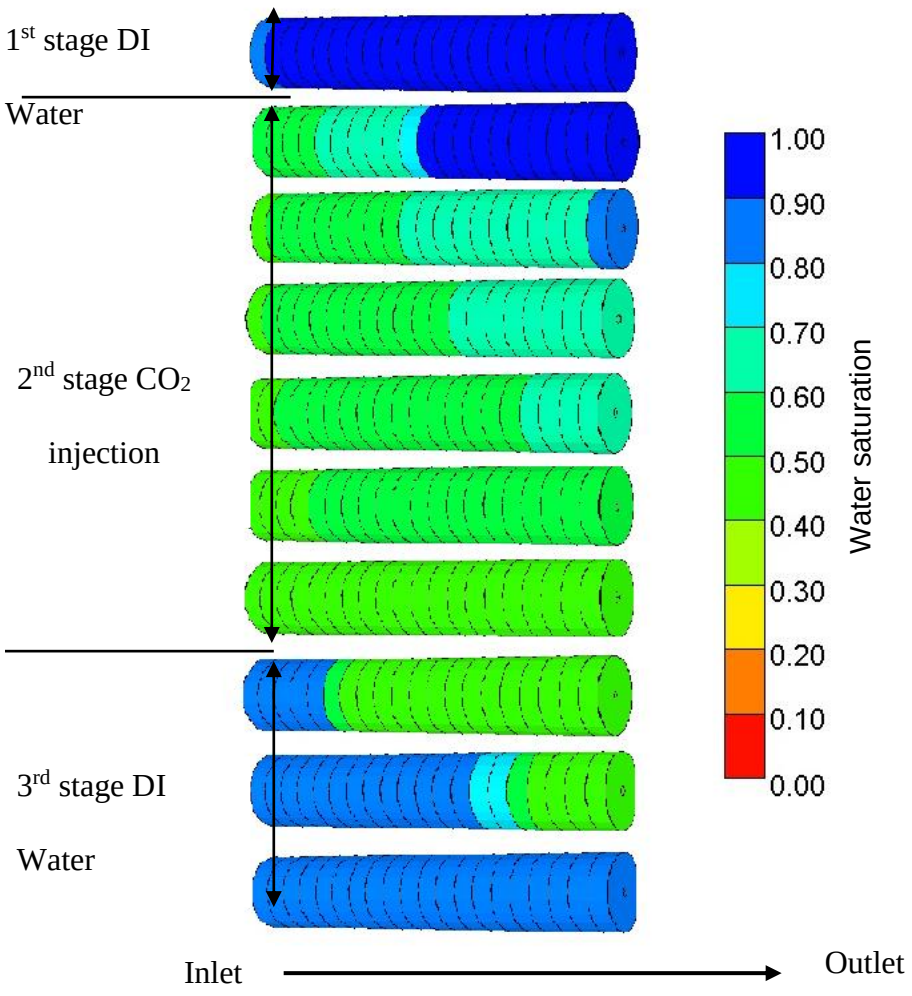


**Fig. 5-13 Water saturation profile along the core during the three injection stages for the base case.**

The relative permeability curves were adjusted so that the pressure drop in the two-phase flow stage obtained from the simulator matched the pressure drop obtained from the experimental work. Eqs. 4 and 5 were used to calculate the relative permeability. **Fig. 13** shows the estimated relative permeability curves as functions of water salinity, $N_2$ concentration in the injected gas, and back pressure. As the water salinity increased, the coal became more $CO_2$-wet. As a result, the residual gas saturation increased and the end-point and cross-point water saturation decreased. Furthermore, the overall gas relative permeability decreased and the water relative permeability increased, which is in agreement with the literature (Durucan et al. 2013; Zhang et al. 2014). Similar behavior was found as a function of $N_2$ concentration. Low displacement efficiency was found as $N_2$ concentration increased and the coal became more water wet. **Fig. 13c** shows a reduction in both water and gas relative permeabilities as the back pressure increased, but $k_{rg}$ reduction was higher than $k_{rw}$ reduction. This behavior was due to the Klinkenberg (slippage) effect that can increase the effective gas permeability at low pressures (Zhang et al. 2014). The relative permeability curves were independent on injection flow rate.

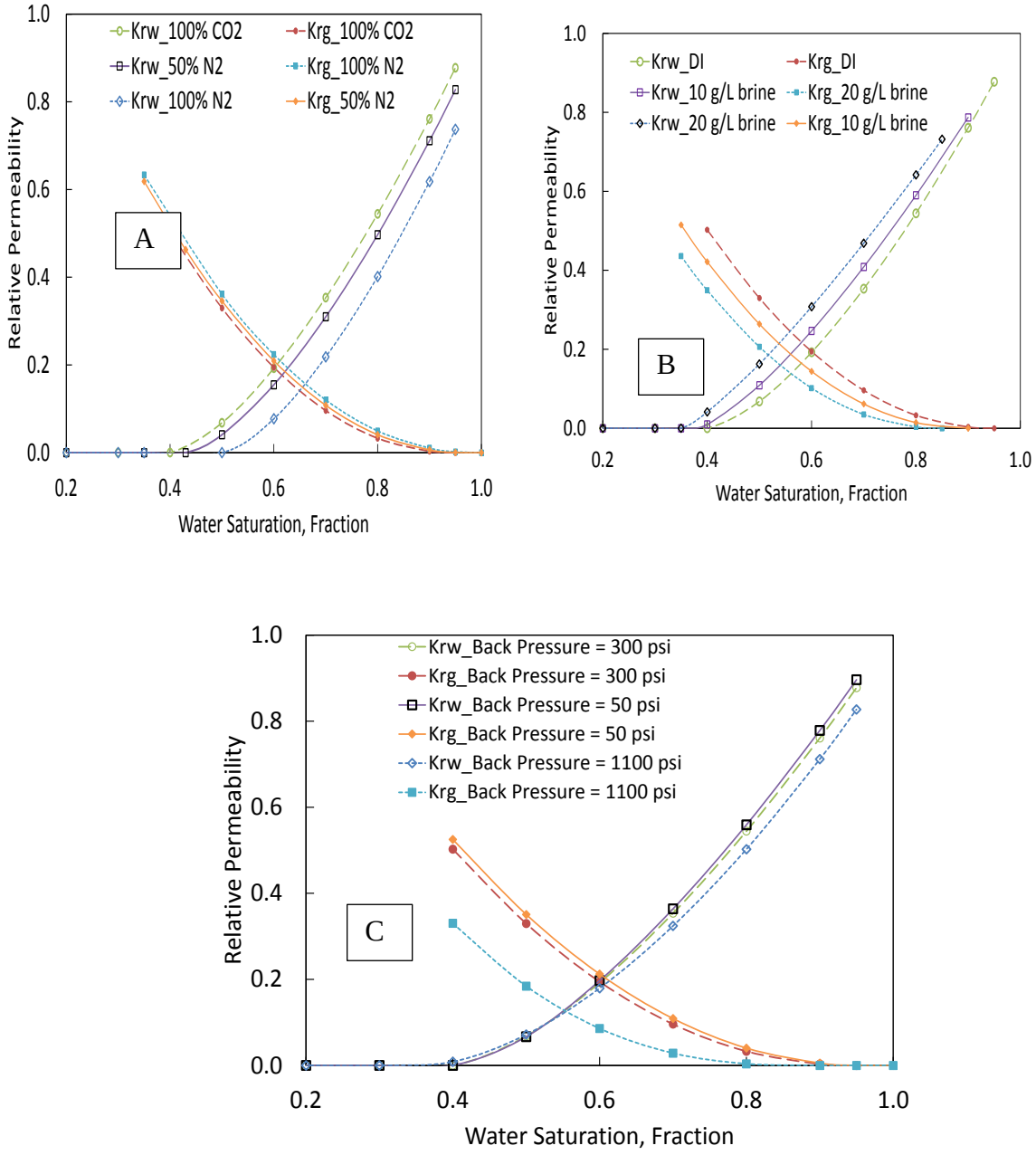


**Fig. 5-14 Relative permeability curves at 1 cm$^3$/min as a function of (A) salt concentration, (B) $N_2$ concentration, and (C) back pressure.**

### 5.6. Pilot Field Evidence

The Allison Unit in the San Juan Basin is the first $CO_2$-ECBM recovery pilot (Reeves and Oudinot 2005). **Fig. 14** shows the production and injection history for this unit. $CO_2$ injection was applied at constant bottom-hole pressure (2300 psi). The injection flow rate was started at 50 MMscf/month, then decreased with time to 20 MMscf/month. The reduction in the well injectivity was due to the swelling effect of the coal matrix, which is in agreement with the permeability dynamics. This behavior was not observed on section 3 of the $CO_2$ injection stage (second stage). This difference was a result of increasing gas relative permeability with time that overcame the reduction in the absolute permeability (as discussed previously), but the change in injectivity could be anticipated from the change in a pressure drop on the third and first injection stages. The increase in the injectivity of $CO_2$ (300 days after decline) was due to the reduction in the reservoir pressure (the produced gas volume is larger than the injected gas volume). As a result, the

$CO_2$ started to desorb from the coal surface and lead to matrix shrinkage that increased the permeability.

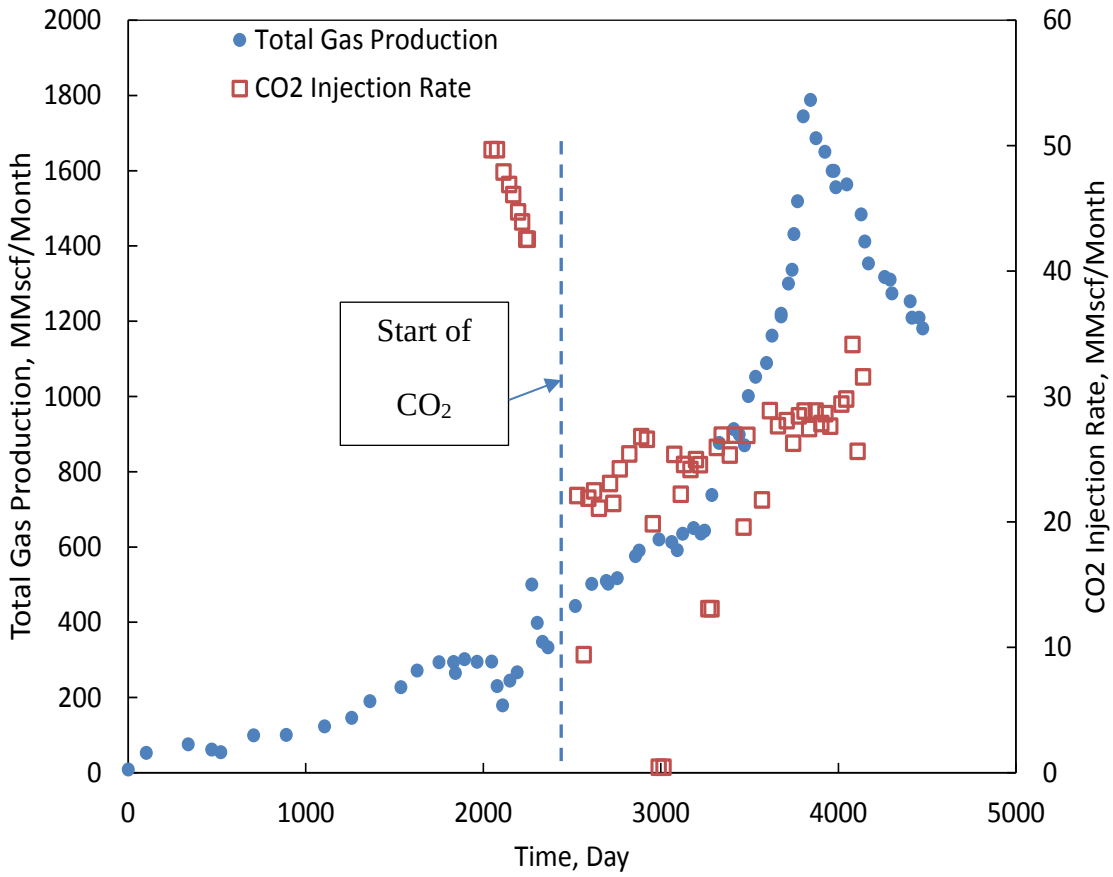


**Fig. 5-15 Gas injection and production flow in Allison Unit in San Juan Basin.**

To compare flue gas and $N_2$ injection for ECBM, the Tiffany Unit in the San Juan Basin was investigated for ECBM by $N_2$ injection. **Fig. 15** shows the production and injection rates in the Tiffany Unit. Almost no change in the injectivity was found, which is in agreement with the results shown in Fig. 5 where the pressure drop difference decreased to 8% at 100% $N_2$. Furthermore, an earlier gas breakthrough was observed with an $N_2$ concentration of 16% in the produced gas, which related to low displacement efficiency, as discussed in earlier. In comparison to $CO_2$ injection, a $CO_2$ breakthrough

was minimal in the Allison Unit during the life of the injection with $CO_2$ at a concentration of 0.6% in the produced gas.

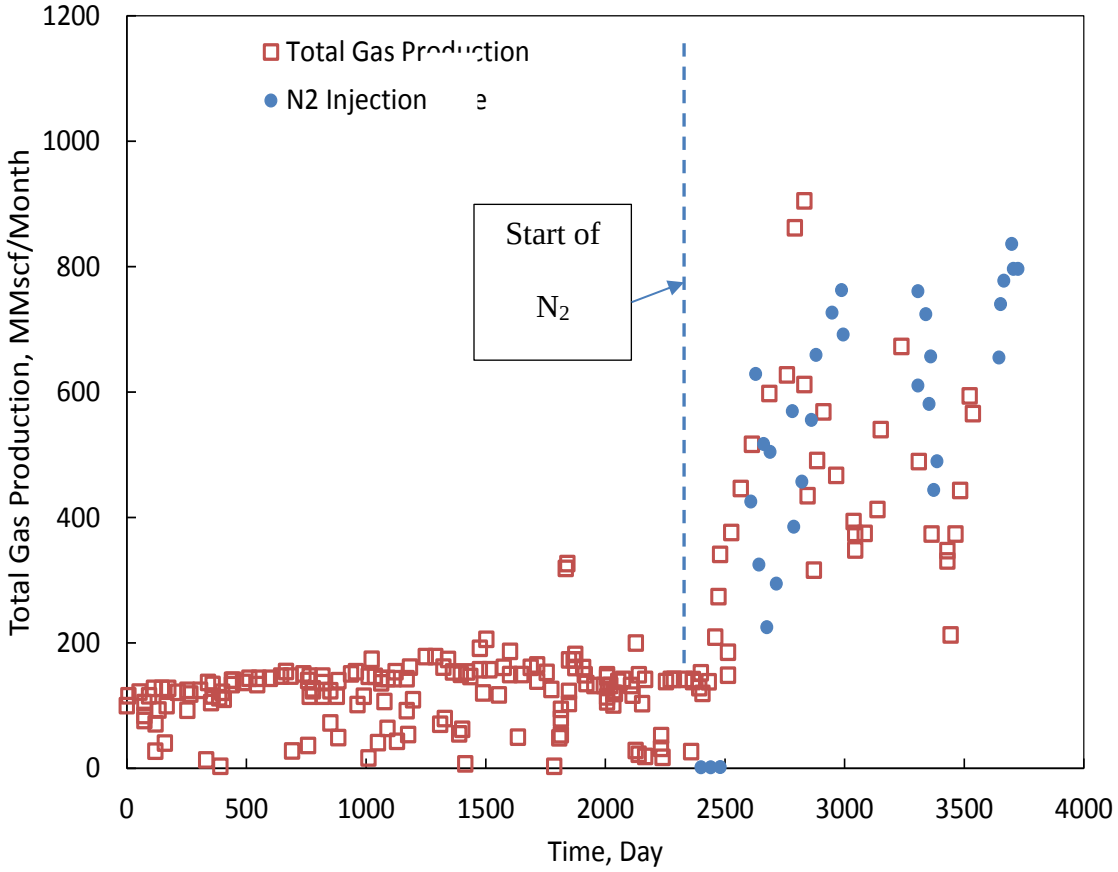


**Fig. 5-16 Gas injection and production flow in the Tiffany Unit in San Juan Basin.**

Moreover, a series of $CO_2$ and $N_2$ injection cycles was conducted previously on the Yobari Test site in North Japan (Fujioka et al. 2010). A micro-pilot test was carried out in the period between May 2004 and October 2007. Preliminary results from several injection tests indicated that $CO_2$ injectivity in fully water-saturated coal seams increased as the water saturation near the injector was decreased during the injection of $CO_2$. This

behavior is similar to results observed in section 3 on the $CO_2$ injection stage (second stage). The preliminary results of the pilot test showed that coal swelling and injectivity reduction was observed and the injection of $N_2$ counteracted the swelling effect.

# CHAPTER VI
# CONCLUSIONS

An integrated model was combined with a developed GMBE, a deliverability equation, and an optimization algorithm. The GMBE accounts for the porosity variation due to matrix shrinkage, formation compressibility, and the solubility of methane in water. The GMBE was formatted similarly to the material balance equation of conventional oil reservoirs. Therefore, Tarner procedure and straight line solution can be used to solve it. From this work, the following conclusions were obtained:

1. The matrix shrinkage effect is significant and needs to be included in the calculations, especially for high gas adsorption content formations. Otherwise, the formation compaction will be dominated in cases of low gas adsorption content.
2. The material balance equations of King and Clarkson and McGovern underestimated OGIP with nearly 10% error. This error was considered by adding the shrinkage effect in the developed material balance equation.
3. The accounting for the solubility of methane in water shows no variation in the OGIP, so its effect can be ignored.
4. The application of the model on actual field cases shows a good match with the actual performance of the three wells. In the case of a single layer model, it estimates a weighted average of the initial gas content, pore volume, matrix shrinkage coefficient, and formation permeability for the coal formations. In the case of a commingled layered model, it estimates the individual performance for each layer by matching the total production for the well.

An integrated model was developed in order to simulate the ECBM performance. It combined a compositional material balance equation, stream tube concept, and optimization algorithm. From this work, the following conclusions were obtained.

1. The developed model helps in estimating on a time basis, the future gas production rate, the permeability and porosity changes, the produced gas composition, and the $CO_2$ distribution on the reservoir.

2. The injection pressure and the production pressure control the total production flowrate.
3. The injection pressure and the production pressure don't affect the breakthrough time but it affects the methane production rate. The reduction in production pressure or increasing the injection pressure accelerates the methane production with almost the same cumulative production.
4. The injection of gas with high Langmuir volume ($CO_2$) improves the methane recovery comparing to gas with low Langmuir volume ($N_2$).
5. Decreasing of Langmuir pressure of the injected gas delays the $CO_2$ breakthrough, improves the methane production rate but decreases the total flow rate due to permeability reduction as a result of the matrix swelling.

The effect of water salinity and injected gas composition on the wettability of bitumen coal was investigated. This work resulted in the following conclusions:

1. The presence of inorganic salts destabilized and compressed the hydrated layer (double layer) surrounding the coal surface, making it more hydrophobic.
2. Salts raised both the contact angle and $CO_2$ adsorption but decreased the absolute value of the zeta potential.
3. As the salt concentration increased, the coal became more $CO_2$-wet, and the NaCl was more effective at changing the wettability than $MgCl_2$ and $CaCl_2$.
4. As $N_2$ concentration in the injected gas increased, the contact angle decreased. In the case of 100% $N_2$, the contact angle remained less than 90˚, and the coal remained water-wet, even at high pressures.

The effects of the formation pressure ($CO_2$ state), injection flow rate, injected gas composition, and the salinity of formation water on $CO_2$ sequestration in high-volatile bituminous coal were examined both experimentally and theoretically. Results yielded the following conclusions:

1. The increase of NaCl concentration reduces the coal permeability, but this effect decreases with high formation pressure.

2. The water salinity in coal formations decreases as the overall gas relative permeability decreases and increases the water relative permeability. Similar behavior was found in the presence of $N_2$ in the injected gas.
3. $CO_2$ injectivity increased initially as gas relative permeability near the well increased, then the injectivity decreased as a result of matrix swelling and absolute permeability reduction.
4. The injection flow rate controls the contact time of $CO_2$ on the coal surface and the $CO_2$ adsorption onto the coal matrix and slightly affects the coal permeability.
5. The presence of $N_2$ in the injected gas decreases the displacement efficiency, and the change in the coal permeability decreases.
6. The higher the back pressure, the lower the water and the gas relative permeabilities.

For $CO_2$ sequestration and ECBM purposes, the injection of pure $CO_2$ into highly volatile bituminous coal is more efficient at high NaCl concentration and high formation pressure.

# REFERENCES


Ahmed, T. 2010. Chapter 6 - Fundamentals of Reservoir Fluid Flow. In *Reservoir Engineering Handbook (Fourth Edition)*, ed. Ahmed, T., Boston: Gulf Professional Publishing.

Ahmed, T. and Meehan, D.N. 2012. Chapter 3 - Unconventional Gas Reservoirs. In *Advanced Reservoir Management and Engineering (Second Edition)*, Boston: Gulf Professional Publishing.

Ahmed, T. H., Centilmen, A., and Roux, B.P. 2006. A Generalized Material Balance Equation for Coalbed Methane Reservoirs. SPE Annual Technical Conference and Exhibition, San Antonio, Texas, USA, 24-27 September. SPE-102638-MS. http://dx.doi.org/10.2118/102638-MS.

Akin, S. and Kovscek, A. 2003. Computed Tomography in Petroleum Engineering Research. *Geological Society, London, Special Publications* **215** (1): 23-38. http://dx.doi: 10.1144/GSL.SP.2003.215.01.03

Alotaibi, M.B., Nasr-El-Din, H.A., and Fletcher, J.J. 2011. Electrokinetics of Limestone and Dolomite Rock Particles. *SPE Reservoir Evaluation & Engineering* **14** (05): 594-603. http://dx.doi.org/10.2118/148701-PA

Ameri, A., Kaveh, N.S., Rudolph, E.S.J. et al. 2013. Investigation on Interfacial Interactions among Crude Oil–Brine–Sandstone Rock–$CO_2$ by Contact Angle Measurements. *Energy & Fuels* **27** (2): 1015-1025. http://dx.doi.org/10.1021/ef3017915

Aminian, K. and Ameri, S. 2009. Predicting Production Performance of CBM Reservoirs. *Journal of Natural Gas Science and Engineering* **1** (1): 25-30. http://dx.doi.org/10.1016/j.jngse.2009.03.003

Anderson, W.G. 1987. Wettability Literature Survey Part 5: The Effects of Wettability on Relative Permeability. *Journal of Petroleum Technology* **39** (11): 1,453-451,468. http://dx.doi.org/10.2118/16323-PA

Arif, M., Barifcani, A., Lebedev, M. et al. 2016. $CO_2$-Wettability of Low to High Rank Coal Seams: Implications for Carbon Sequestration and Enhanced Methane Recovery. *Fuel* **181**: 680-689. http://dx.doi.org/10.1016/j.fuel.2016.05.053

Arps, J. 1945. Analysis of Decline Curves. *Transactions of the American Institute of Mining, Metallurgical and Petroleum Engineers* **160**: 228-247. http://dx.doi.org/10.2118/945228-G

Ayers Jr, W.B. 2003. Coalbed Methane in the Fruitland Formation, San Juan Basin, Western United States: A Giant Unconventional Gas Play. *AAPG Memoir* **85**(78):159-188. http://dx.doi.org/10.1306/8626D4D7-173B-11D7-8645000102C1865D

Battistutta, E., van Hemert, P., Lutynski, M. et al. 2010. Swelling and Sorption Experiments on Methane, Nitrogen and Carbon Dioxide on Dry Selar Cornish Coal. *International Journal of Coal Geology* **84** (1): 39-48. http://dx.doi.org/10.1016/j.coal.2010.08.002

Benson, S.M. and Cole, D.R. 2008. $CO_2$ Sequestration in Deep Sedimentary Formations. *Elements* **4** (5): 325-331. http://dx.doi.org/10.2113/gselements.4.5.325

Busch, A., Gensterblum, Y., and Krooss, B.M. 2003. Methane and $CO_2$ Sorption and Desorption Measurements on Dry Argonne Premium Coals: Pure Components and Mixtures. *International Journal of Coal Geology* **55** (2–4): 205-224. http://dx.doi.org/10.1016/S0166-5162(03)00113-7

Busch, A. and Gensterblum, Y. 2011. Cbm and $CO_2$-ECBM Related Sorption Processes in Coal: A Review. *International Journal of Coal Geology* **87** (2): 49-71. http://dx.doi.org/10.1016/j.coal.2011.04.011

Carroll, R.E. and Pashin, J.C. 2003. Relationship of Sorption Capacity to Coal Quality: $CO_2$ Sequestration Potential of Coalbed Methane Reservoirs in the Black Warrior Basin. In *2003 International Coalbed Methane Symposium, Paper*, 317.

Chen, D., Pan, Z., Liu, J. et al. 2013. An Improved Relative Permeability Model for Coal Reservoirs. *International Journal of Coal Geology* **109–110** (0): 45-57. DOI: http://dx.doi.org/10.1016/j.coal.2013.02.002

Chiquet, P., Broseta, D., and Thibeau, S. 2007. Wettability Alteration of Caprock Minerals by Carbon Dioxide. *Geofluids* **7** (2): 112-122. http://dx.doi.org/10.1111/j.1468-8123.2007.00168.x

Choy, K.K.H., Porter, J.F., and McKay, G. 2000. Langmuir Isotherm Models Applied to the Multicomponent Sorption of Acid Dyes from Effluent onto Activated Carbon. *Journal of Chemical & Engineering Data* **45** (4): 575-584. http://dx.doi.org/10.1021/je9902894

Clarkson, C.R. and Bustin, R.M. 2000. Binary Gas Adsorption/Desorption Isotherms: Effect of Moisture and Coal Composition Upon Carbon Dioxide Selectivity over Methane. *International Journal of Coal Geology* **42** (4): 241-271. http://dx.doi.org/10.1016/S0166-5162(99)00032-4

Clarkson, C. and Mcgovern, J. 2001. Study of the Potential Impact of Matrix Free Gas Storage Upon Coalbed Gas Reserves and Production Using a New Material Balance Equation. In *Paper 0113 presented at the International Coalbed Methane Symposium, Tuscaloosa, Alabama*:14-18.

Clarkson, C.R., Pan, Z., Palmer, I.D. et al. 2010. Predicting Sorption-Induced Strain and Permeability Increase with Depletion for Coalbed-Methane Reservoirs. *SPE Journal* **15** (01): 152-159. http://dx.doi.org/10.2118/114778-PA

Clarkson, C.R., Rahmanian, M., Kantzas, A. et al. 2011. Relative Permeability of Cbm Reservoirs: Controls on Curve Shape. *International Journal of Coal Geology* **88** (4): 204-217. http://dx.doi.org/10.1016/j.coal.2011.10.003

Clarkson, C.R. 2013. Production Data Analysis of Unconventional Gas Wells: Review of Theory and Best Practices. *International Journal of Coal Geology* **109**: 101-146. http://dx.doi.org/10.1016/j.coal.2013.01.002

Crosdale, P.J., Moore, T.A., and Mares, T.E. 2008. Influence of Moisture Content and Temperature on Methane Adsorption Isotherm Analysis for Coals from a Low-Rank, Biogenically-Sourced Gas Reservoir. *International Journal of Coal Geology* **76** (1–2): 166-174. http://dx.doi.org/10.1016/j.coal.2008.04.004

Dusseault, M., Bachu, S., and Rothenburg, L. 2004. Sequestration of $CO_2$ in Salt Caverns. *Journal of Canadian Petroleum Technology* **43** (11): 49-55. http://dx.doi.org/10.2118/04-11-04

Enoh, M.E. 2007. A Tool to Predict the Production Performance of Vertical Wells in a Coalbed Methane Reservoir, West Virginia University. ProQuest Dissertations Publishing.

Espie, T. 2005. A New Dawn for $CO_2$ EOR. International Petroleum Technology Conference, Doha, Qatar, 21-23 November. IPTC-10935-MS. http://dx.doi.org/10.2523/IPTC-10935-MS

Espinoza, D.N. and Santamarina, J.C. 2010. Water-$CO_2$-Mineral Systems: Interfacial Tension, Contact Angle, and Diffusion—Implications to $CO_2$ Geological Storage. *Water Resources Research* **46** (7): 1-10. http://dx.doi.org/10.1029/2009WR008634

Farokhpoor, R., Bjørkvik, B.J.A., Lindeberg, E. et al. 2013. Wettability Behaviour of $CO_2$ at Storage Conditions. *International Journal of Greenhouse Gas Control* **12** (0): 18-25. http://dx.doi.org/10.1016/j.ijggc.2012.11.003

Fenghour, A. and Wakeham, W.A. 1997. The Viscosity of Carbon Dioxide. *Journal of Physical Chemistry Reference Data* **27** (1): 31-44. http://dx.doi.org/10.1063/1.556013

Fujioka, M., Yamaguchi, S., and Nako, M. 2010. $CO_2$-ECBM Field Tests in the Ishikari Coal Basin of Japan. *International Journal of Coal Geology* **82** (3–4): 287-298. http://dx.doi.org/10.1016/j.coal.2010.01.004

Garduno, J.L., Morand, H., Saugier, L. et al. 2003. $CO_2$ Sequestration Potential of Texas Low-Rank Coals. SPE Annual Technical Conference and Exhibition, Denver, Colorado, 5-8 October. SPE-84154-MS. http://dx.doi.org/10.2118/84154-MS

Gray, I. 1987. Reservoir Engineering in Coal Seams: Part 1-the Physical Process of Gas Storage and Movement in Coal Seams. *SPE Reservoir Engineering* **2** (1): 28-34. http://dx.doi.org/10.2118/12514-PA

Hamawand, I., Yusaf, T., and Hamawand, S.G. 2013. Coal Seam Gas and Associated Water: A Review Paper. *Renewable and Sustainable Energy Reviews* **22** (0): 550-560. http://dx.doi.org/10.1016/j.rser.2013.02.030

Harpalani, S. and Schraufnagel, R.A. 1990. Shrinkage of Coal Matrix with Release of Gas and Its Impact on Permeability of Coal. *Fuel* **69** (5): 551-556. http://dx.doi.org/10.1016/0016-2361(90)90137-F

Harvey, P.A., Nguyen, A.V., and Evans, G.M. 2002. Influence of Electrical Double-Layer Interaction on Coal Flotation. *Journal of Colloid and Interface Science* **250** (2): 337-343. http://dx.doi.org/10.1006/jcis.2002.8367

Hatch, J. 2007. Petroleum Assessment of the Pottsville Coal Total Petroleum System, Black Warrior Basin, Alabama and Mississippi Geologic Assessment of Undiscovered Oil and Gas Resources of the Black Warrior Basin Province, Alabama and Mississippi: U.S. Geological Survey Digital Data Series DDS–69–I, chap. 4, 28 p.

He, Q., Mohaghegh, S.D., and Gholami, V. 2013. A Field Study on Simulation of $CO_2$ Injection and Ecbm Production and Prediction of $CO_2$ Storage Capacity in Unmineable Coal Seam. *Journal of Petroleum Engineering* **2013**: 8. http://dx.doi.org/10.1155/2013/803706

Holland, J.H. 1975. Adaptation in Natural and Artificial Systems: An Introductory Analysis with Applications to Biology, Control, and Artificial Intelligence: U Michigan Press. MIT Press Cambridge, MA.

Houghton, J.T., Ding, Y., Griggs, D.J. et al. 2001. Climate Change 2001: The Scientific Basis. The Press Syndicate of the University of Cambridge. http://dx.doi.org/10.1002/qj.200212858119

Ibrahim, A. F, Nasreldin, H. A. 2015. History Matching and Predicting Gas Production During ECBM. Presented at Unconventional Resources Technology Conference, San Antonio, Texas, USA, 20-22 July. URTEC-2147766-MS. https://doi.org/10.15530/URTEC-2015-2147766

Kapoor, A., Ritter, J.A., and Yang, R.T. 1990. An Extended Langmuir Model for Adsorption of Gas Mixtures on Heterogeneous Surfaces. *Langmuir* **6** (3): 660-664. http://dx.doi.org/10.1021/la00093a022

King, G. 1990. Material Balance Techniques for Coal Seam and Devonian Shale Gas Reservoirs. SPE Annual Technical Conference and Exhibition, New Orleans, Louisiana, 23-26 September. SPE-20730-MS. http://dx.doi.org/10.2118/20730MS

King, G. 1993. Material-Balance Techniques for Coal-Seam and Devonian Shale Gas Reservoirs with Limited Water Influx. *SPE reservoir engineering* **8** (01): 67-72. http://dx.doi.org/10.2118/20730-PA

Kwok, D. and Neumann, A. 1999. Contact Angle Measurement and Contact Angle Interpretation. *Advances in colloid and interface science* **81** (3): 167-249. http://dx.doi.org/10.1016/S0001-8686(98)00087-6

Kwok, D.Y. and Neumann, A.W. 2000. Contact Angle Interpretation in Terms of Solid Surface Tension. *Colloids and Surfaces A: Physicochemical and Engineering Aspects* **161** (1): 31-48. http://dx.doi.org/10.1016/S0927-7757(99)00323-4

Langmuir, I. 1916. The Constitution and Fundamental Properties of Solids and Liquids. Part I. Solids. *Journal of the American Chemical Society* **38** (11): 2221-2295. http://dx.doi.org/10.1021/ja02268a002

Laubach, S.E., Marrett, R.A., Olson, J.E. et al. 1998. Characteristics and Origins of Coal Cleat: A Review. *International Journal of Coal Geology* **35** (1–4): 175-207. http://dx.doi.org/10.1016/S0166-5162(97)00012-8

Le Gal, N., Lagneau, V., and Charmoille, A. 2012. Experimental Characterization of Ch4 Release from Coal at High Hydrostatic Pressure. *International Journal of Coal Geology* **96–97** (0): 82-92. http://dx.doi.org/10.1016/j.coal.2012.04.001

Leighton, A.J. and Higgins, R.V. 1975. Improved Method to Predict Multiphase Waterflood Performance for Constant Rates or Pressures. Report of Investigations / Bureau of Mines. U.S. Dept. of the Interior, Bureau of Mines.

Li, Q., Lin, B., Zhao, S. et al. 2013. Surface Physical Properties and Its Effects on the Wetting Behaviors of Respirable Coal Mine Dust. *Powder Technology* **233**: 137-145. http://dx.doi.org/10.1016/j.powtec.2012.08.023

Liu, J., Chen, Z., Elsworth, D. et al. 2011. Interactions of Multiple Processes During Cbm Extraction: A Critical Review. *International Journal of Coal Geology* **87** (3–4): 175-189. http://dx.doi.org/10.1016/j.coal.2011.06.004

Liu, S. and Harpalani, S. 2013. Permeability Prediction of Coalbed Methane Reservoirs During Primary Depletion. *International Journal of Coal Geology* **113**: 1-10. http://dx.doi.org/10.1016/j.coal.2013.03.010

Maphala, T. and Wagner, N.J. 2012. Effects of $CO_2$ Storage in Coal on Coal Properties. *Energy Procedia* **23**: 426-438. http://dx.doi.org/10.1016/j.egypro.2012.06.070

Mavor, M.J., Gunter, W.D., Robinson, J.R. et al. 2002. Testing for $CO_2$ Sequestration and Enhanced Methane Production from Coal. SPE Gas Technology Symposium, Calgary, Alberta, Canada, 30 April-2 May. SPE-75683-MS. http://dx.doi.org/10.2118/75683-MS

Mazumder, S., Plug, W.-J., and Bruining, H. 2003. Capillary Pressure and Wettability Behavior of Coal-Water-Carbon Dioxide System. SPE Annual Technical Conference and Exhibition, Denver, Colorado, 5-8 October. SPE-84339-MS. http://dx.doi.org/10.2118/84339-MS

Mazumder, S., Wolf, K.H.a.A., Hemert, P. et al. 2008. Laboratory Experiments on Environmental Friendly Means to Improve Coalbed Methane Production by Carbon Dioxide/Flue Gas Injection. *Transport in Porous Media* **75** (1): 63-92. http://dx.doi.org/10.1007/s11242-008-9222-z

Mckee, C.R. 1987. Stress-Dependent Permeability and Porosity of Coal. *SPE Formation Evaluation.* **3** (1): 81-91. http://dx.doi.org/10.2118/12858-PA

Meehan, D.N. 1980. Estima;ting Water Viscosity at Reservoir Conditions. *Petroleum Engineering*: 117-118.

Mohamed, I. and Nasr-El-Din, H.A. 2013. Fluid/Rock Interactions During $CO_2$ Sequestration in Deep Saline Carbonate Aquifers: Laboratory and Modeling Studies. *SPE Journal* **18** (03): 468-485.

Mora, C.A. 2007. Comparison of Computation Methods for Cbm Production Performance. Master of Science, Texas A&M University.

Nasralla, R.A., Bataweel, M.A., and Nasr-El-Din, H.A. 2013. Investigation of Wettability Alteration and Oil-Recovery Improvement by Low-Salinity Water in Sandstone Rock. *Journal of Canadian Petroleum Technology* **52** (02): 144-154.

Ozdemir, O. 2013. Specific Ion Effect of Chloride Salts on Collectorless Flotation of Coal. *Physicochemical Problems of Mineral Processing* **49**.

Palmer, I. 1998. How Permeability Depends on Stress and Pore Pressure in Coalbeds: A New Model. *SPE reservoir engineering* **1** (6): 539-543.

Palmer, I. 2009. Permeability Changes in Coal: Analytical Modeling. *International Journal of Coal Geology* **77** (1–2): 119-126. DOI: http://dx.doi.org/10.1016/j.coal.2008.09.006

Pashin, J.C. 2007. Hydrodynamics of Coalbed Methane Reservoirs in the Black Warrior Basin: Key to Understanding Reservoir Performance and Environmental Issues. *Applied Geochemistry* **22** (10): 2257-2272. DOI: http://dx.doi.org/10.1016/j.apgeochem.2007.04.009

Peng, D.Y. and Robinson, D.B. 1976. A New Two-Constant Equation of State. *Industrial & Engineering Chemistry Fundamentals* **15** (1): 59-64.

Pilisi, N., Ceyhan, I., and Vasantharajan, S. 2010. $CO_2$ Sequestration in Deepwater Subseabed Formations. In *SPE International Conference on* $CO_2$ *Capture Storage and Utilization*: Society of Petroleum Engineers.ISBN 155563317X.

Plug, W.-J., Mazumder, S., and Bruining, J. 2008. Capillary Pressure and Wettability Behavior of $CO_2$ Sequestration in Coal at Elevated Pressures. *Spe Journal* **13** (04): 455-464.

Powwas, T. 1998. How Permeability Depends on Stress and Pore Pressure a New Model.

Reeves, S. and Oudinot, A. 2005. The Allison Unit Co2-Ecbm Pilot–a Reservoir and Economic Analysis. In *2005 International Coalbed Methane Symposium, Paper*, 522:16-20.

Saghafi, A., Pinetown, K., and Javanmard, H. 2014. Gas Wettability of Coal and Implications for Gas Desorption and Drainage. Paper presented at the 14th Coal Operators' Conference, University of Wollonong. the Australasian Institute of Mining and Metallurgy & Mine Managers Association of Australia.

Sakurovs, R. and Lavrencic, S. 2011. Contact Angles in Co2-Water-Coal Systems at Elevated Pressures. *International Journal of Coal Geology* **87** (1): 26-32. DOI: http://dx.doi.org/10.1016/j.coal.2011.04.005

Salgın, S., Salgın, U., and Bahadır, S. 2012. Zeta Potentials and Isoelectric Points of Biomolecules: The Effects of Ion Types and Ionic Strengths. *Int. J. Electrochem. Sci* **7**: 12404-12414.

Schroeder, K., Ozdemir, E., and Morsi, B. 2002. Sequestration of Carbon Dioxide in Coal Seams. *gas* **2**: 2.

Seidle, J.P. 1999. A Modified P/Z Method for Coal Wells. In *SPE Rocky Mountain regional meeting*:223-236.

Seidle, J.P. 2000. Reservoir-Engineering Aspects of $CO_2$ Sequestration in Coals. *Journal of petroleum technology* **52** (4): 64-66.

Seidle, J. 2011. *Fundamentals of Coalbed Methane Reservoir Engineering*: PennWell Books. Original edition. ISBN 1593700016.

Shi, J.-Q. and Durucan, S. 2005. A Model for Changes in Coalbed Permeability During Primary and Enhanced Methane Recovery. *SPE Reservoir Evaluation & Engineering* **8** (04): 291-299.

Shi, J. and Durucan, S. 2004. Drawdown Induced Changes in Permeability of Coalbeds: A New Interpretation of the Reservoir Response to Primary Recovery. *Transport in porous media* **56** (1): 1-16.

Shimada, S., Li, H., Oshima, Y. et al. 2005. Displacement Behavior of Ch4 Adsorbed on Coals by Injecting Pure Co2, N2, and Co2–N2 Mixture. *Environmental Geology* **49** (1): 44-52. DOI: 10.1007/s00254-005-0057-4

Shojai, K. N., Rudolph, E.S.J., Wolf, K.-H.a.A. et al. 2011. Wettability Determination by Contact Angle Measurements: Hvbb Coal–Water System with Injection of Synthetic Flue Gas and Co2. *Journal of Colloid and Interface Science* **364** (1): 237-247. DOI: http://dx.doi.org/10.1016/j.jcis.2011.07.091

Shojai, K. N., Wolf, K.H., Ashrafizadeh, S.N. et al. 2012. Effect of Coal Petrology and Pressure on Wetting Properties of Wet Coal for Co2 and Flue Gas Storage. *International Journal of Greenhouse Gas Control* **11, Supplement** (0): S91-S101. DOI: http://dx.doi.org/10.1016/j.ijggc.2012.09.009

Siemons, N., Bruining, H., Castelijns, H. et al. 2006. Pressure Dependence of the Contact Angle in a Co2–H2o–Coal System. *Journal of Colloid and Interface Science* **297** (2): 755-761. DOI: http://dx.doi.org/10.1016/j.jcis.2005.11.047

Standard, A. 2013. Standard Test Methods for Proximate Analysis of Coal and Coke by Macro Thermogravimetric Analysis.

State, U.S.D.o. 2010. *U.S. Climate Action Report 2010*. Washington: Global Publishing Services.

Tarner, J. 1944. How Different Size Gas Caps and Pressure Maintenance Programs Affect Amount of Recoverable Oil. *Oil Weekly* **144** (2): 32-34.

Taud, H., Martinez-Angeles, R., Parrot, J. et al. 2005. Porosity Estimation Method by X-Ray Computed Tomography. *Journal of petroleum science and engineering* **47** (3): 209-217.

Vishal, V., Singh, T.N., and Ranjith, P.G. 2015. Influence of Sorption Time in Co2-Ecbm Process in Indian Coals Using Coupled Numerical Simulation. *Fuel* **139**: 51-58. DOI: http://dx.doi.org/10.1016/j.fuel.2014.08.009

Williams-Kovacs, J., Clarkson, C.R., and Nobakht, M. 2012. Impact of Material Balance Equation Selection on Rate-Transient Analysis of Shale Gas. In *SPE Annual*

*Technical Conference and Exhibition*: Society of Petroleum Engineers.ISBN 1613992130.

Wu, Y., Liu, J., Chen, Z. et al. 2011. A Dual Poroelastic Model for $CO_2$ -Enhanced Coalbed Methane Recovery. *International Journal of Coal Geology* **86** (2–3): 177-189. DOI: http://dx.doi.org/10.1016/j.coal.2011.01.004

Young, T. 1805. An Essay on the Cohesion of Fluids. *Philosophical Transactions of the Royal Society of London* **95**: 65-87.

Yu, H., Yuan, J., Guo, W. et al. 2008. A Preliminary Laboratory Experiment on Coalbed Methane Displacement with Carbon Dioxide Injection. *International Journal of Coal Geology* **73** (2): 156-166. DOI: http://dx.doi.org/10.1016/j.coal.2007.04.005

Zhao, D., Zhao, Y., and Feng, Z. 2011. Laboratory Experiment on Coalbed-Methane Desorption Influenced by Water Injection and Temperature. *Journal of Canadian Petroleum Technology* **50** (7/8): pp. 24-33. DOI: 10.2118/148945-pa

Zhou, F., Hou, W., Allinson, G. et al. 2013. A Feasibility Study of Ecbm Recovery and Co 2 Storage for a Producing Cbm Field in Southeast Qinshui Basin, China. *International Journal of Greenhouse Gas Control* **19**: 26-40.

Zhou, F., Hussain, F., and Cinar, Y. 2013. Injecting Pure $N_2$ and $CO_2$ to Coal for Enhanced Coalbed Methane: Experimental Observations and Numerical Simulation. *International Journal of Coal Geology* **116–117** (0): 53-62. DOI: http://dx.doi.org/10.1016/j.coal.2013.06.004

Zhu, W., Wei, C., Liu, J. et al. 2013. Impact of Gas Adsorption Induced Coal Matrix Damage on the Evolution of Coal Permeability. *Rock mechanics and rock engineering* **46** (6): 1353-1366.